UNICAMP

UNIVERSIDADE ESTADUAL DE CAMPINAS
INSTITUTO DE FÍSICA "GLEB WATAGHIN"

DOCTORAL THESIS

RENAN PICORETI NAKAHARA

INVISIBLE AND VISIBLE DECAY OF SOLAR NEUTRINOS

DECAIMENTO INVISÍVEL E VISÍVEL DE NEUTRINOS SOLARES

CAMPINAS
2021

RENAN PICORETI NAKAHARA

INVISIBLE AND VISIBLE DECAY OF SOLAR NEUTRINOS

DECAIMENTO INVISÍVEL E VISÍVEL DE NEUTRINOS SOLARES

Tese apresentada ao Instituto de Física "Gleb Wataghin" da Universidade Estadual de Campinas como parte dos requisitos exigidos para a obtenção do título de Doutor em Ciências.

Thesis presented to the "Gleb Wataghin" Institute of Physics of the University of Campinas in partial fulfillment of the requirements for the degree of Doctor in Science.

Orientador: Prof. Dr. Orlando L. G. Peres

Este exemplar corresponde à versão final da tese defendida por Renan Picoreti Nakahara e orientada por Prof. Dr. Orlando Luis Goulart Peres.

CAMPINAS
2021

Ficha catalográfica
Universidade Estadual de Campinas
Biblioteca do Instituto de Física Gleb Wataghin
Lucimeire de Oliveira Silva da Rocha - CRB 8/9174

P588i Picoreti Nakahara, Renan, 1986-
Invisible and visible decay of solar neutrinos / Renan Picoreti Nakahara. – Campinas, SP : [s.n.], 2020.

Orientador: Orlando Luís Goulart Peres.
Tese (doutorado) – Universidade Estadual de Campinas, Instituto de Física Gleb Wataghin.

1. Neutrinos. 2. Neutrinos solares. 3. Decaimento de neutrinos. I. Peres, Orlando Luís Goulart, 1969-. II. Universidade Estadual de Campinas. Instituto de Física Gleb Wataghin. III. Título.

Informações para Biblioteca Digital

Título em outro idioma: Decaimento invisível e visível de neutrinos solares
Palavras-chave em inglês:
Neutrinos
Solar neutrinos
Neutrino decay
Área de concentração: Física
Titulação: Doutor em Ciências
Banca examinadora:
Orlando Luís Goulart Peres [Orientador]
Arlene Cristina Aguilar
Ettore Segreto
Pedro Accioly Nogueira Machado
André Luiz Carvalho de Gouvêa
Data de defesa: 17-12-2020
Programa de Pós-Graduação: Física

Identificação e informações acadêmicas do(a) aluno(a)
- ORCID do autor: https://orcid.org/0000-0001-8306-3098
- Currículo Lattes do autor: http://lattes.cnpq.br/5613639525786606

MEMBROS DA COMISSÃO JULGADORA DA TESE DE DOUTORADO DE **RENAN PICORETI NAKAHARA – RA 88979** APRESENTADA E APROVADA AO INSTITUTO DE FÍSICA "GLEB WATAGHIN", DA UNIVERSIDADE ESTADUAL DE CAMPINAS, EM 17 / 12 / 2020.

COMISSÃO JULGADORA:

- Prof. Dr. Orlando Luis Goulart Peres – Orientador – DRCC/IFGW/UNICAMP
- Profa. Dra. Arlene Cristina Aguilar – DRCC/IFGW/UNICAMP
- Prof. Dr. Ettore Segreto – DRCC/IFGW/UNICAMP
- Prof. Dr. Pedro Accioly Nogueira Machado – IF/USP
- Prof. Dr. André Luiz Carvalho de Gouvêa – NU

OBS.: Ata da defesa com as respectivas assinaturas dos membros encontra-se no SIGA/Sistema de Fluxo de Dissertação/Tese e na Secretaria do Programa da Unidade.

CAMPINAS
2021

Acknowledgements

First and foremost, I would like to thank my husband Thiago Seike Picoreti Nakahara for his invaluable support for the last eleven years.

Next, I would like to thank my supervisor Dr. Orlando L. G. Peres for his guidance since my M.Sc. studies, for the several opportunities given to me throughout these years, and specially for his insightful supervision during the development of my Ph.D. project.

I also gratefully acknowledge Dr. Julia Tjus supervision during the sandwich Ph.D. period at Ruhr-Universität Bochum, Germany.

I would like to thank my colleagues and friends at the University of Campinas (UNICAMP), specially Pedro Simoni Pasquini and Gabriela Stenico, for the fruitful and often amusing discussions during our *frequent* coffee breaks.

I am thankful as well to my colleagues and friends at the Communications Office of the Brazilian Center for Research in Energy and Materials (CNPEM) for being supportive at each and every one of my frequent assertions for the last five years that "this year I will defend my thesis".

Finally, I would like to thank my family for being unwittingly offensive by constantly asking when I would defend the thesis.

This study was financed in part by the Coordenação de Aperfeiçoamento de Pessoal de Nível Superior – Brasil (CAPES) – Finance Code 001. The sandwich PhD period at Ruhr-Universität Bochum, Germany, was supported by "Programa Conjunto de Bolsas de Doutorado na República Federal da Alemanha 2011/2012 DAAD - CAPES - CNPq", process BEX 12371/12-2.

Resumo

Neutrinos solares são produzidos nos processos de fusão termonuclear que alimentam o Sol. Os primeiros experimentos para sua detecção indicavam um fluxo de neutrinos solares menor do que o previsto pelos modelos padrão solares, no que veio a ser conhecido como o problema do neutrino solar (*Solar Neutrino Problem* — SNP). Experimentos posteriores eventualmente estabeleceram o modelo de oscilação de sabor com ângulo de mistura grande e com a conversão de sabor ressonante de Mikheyev-Smirnov-Wolfenstein (LMA-MSW, na sigla em inglês) como a solução para o SNP. A solução LMA-MSW estabelece, acima de qualquer dúvida razoável, a natureza massiva dos neutrinos, o que torna possível que os neutrinos decaiam em outras partículas. Neste trabalho, investigamos o decaimento de neutrinos como um efeito secundário na propagação de neutrinos solares a fim de extrair novos limites para o tempo de vida dos neutrinos usando os dados experimentais mais recentes.

Abstract

Solar neutrinos are produced in the thermonuclear fusion processes that power the Sun. Early experiments indicated a solar neutrino flux lower than the predicted by the Solar Standard Models, which came to be known as the Solar Neutrino Problem (SNP). Later solar neutrino experiments eventually established the Neutrino Flavor Oscillation model with Large Mixing Angle and Mikheyev-Smirnov-Wolfenstein Resonant Flavor Conversion (LMA-MSW) as the solution to the SNP. The LMA-MSW solution establishes beyond reasonable doubt the massive nature of neutrinos, which makes it possible for neutrinos to decay into other particles. In this work, we investigate neutrino decay as a sub-leading effect in the propagation of solar neutrinos to extract new limits to neutrino lifetime using the most recent experimental data.

List of Figures

List of Tables

Contents

Introduction

From the discovery of sunspots — which *hinted* at the possibility of an imperfect sky — to the Solar Neutrino Problem — which led to the discovery of neutrino oscillations and the massive nature of neutrinos —, the Sun has been a constant source of new phenomena challenging the scientific knowledge of each generation. Moreover, the Sun has also been a laboratory for testing new theories, such as the observation of solar eclipses in the early 20th Century, which provided early evidence in favour of Einstein's General Relativity. Similarly, neutrinos have consistently confronted the *status quo* since they were proposed by Wolfgang Pauli in 1930 [1] to explain the continuous energy spectrum of electrons produced in the beta decay. The neutrino oscillation phenomenon, for example, is currently one of the most significant deviations from the Standard Model, establishing neutrinos as massive particles. Being massive, it becomes possible for neutrinos to decay into other particles.

In **Chapter One**, we present an introductory discussion on the properties of the Sun, the models built from observational data and used to described its inner structure and energy generation through thermonuclear fusion processes, and the consequent production of solar neutrinos. In **Chapter Two**, neutrino oscillations are described, both in vacuum and in matter, and applied in the propagation of solar neutrinos from production to detection. In **Chapter Three**, neutrino decay models are presented and the formalism necessary to account for both neutrino oscillations and decay as a secondary effect on the propagation of solar neutrinos is discussed. In **Chapter Four**, we investigate the solar neutrino invisible decay, in which daughter particles are not detectable/detected by an experiment. The formalism is presented and its consequences to the solar neutrino flux are analysed. From this analysis, we extract new lower limits to neutrino lifetime in this decay scenario. Finally, in **Chapter Five**, we investigate the solar neutrino visible decay, in which at least one of the daughter particles is in principle detectable, is discussed. The formalism is presented and its consequences to the solar neutrino flux are analysed. From this analysis, we extract new lower limits to neutrino lifetime in this decay scenario.

Chapter 1

The Sun and Solar Neutrinos

The Sun is a Main Sequence star — in the Hertzsprung-Russell diagram[1] — of spectral type G [2]. It has a radius of around 7×10^5 km and a mass of 2×10^{30} kg, concentrating about 99.9% of the total mass of the Solar System. The Sun rotates around the galactic center at a 10 kpc radius[2] and at speeds of approximately $250\,\mathrm{km} \cdot \mathrm{s}^{-1}$.

The Sun was formed from the gravitational collapse of a cloud of gas and dust around 4.6 billion years ago. During the collapse, the gas in the cloud heats up until temperature and pressure in its innermost region are enough to initiate thermonuclear fusion reactions, transforming hydrogen into helium. The energy release allows the outwards pressure of the hot gas to balance the inwards force of gravity. The gas reach hydrostatic equilibrium, the collapse stops and the star is born.

In this Chapter, the properties of the Sun are discussed, alongside models constructed from observational data and used to described its inner structure and energy generation through thermonuclear fusion processes. The production of the so-called solar neutrinos by such reactions is also discussed.

1.1 Solar Standard Models and Solar Structure

The Sun can be probed through a variety of methods, from the astronomical observation of surface properties and phenomena to the measurement of its normal modes of oscillation — known as helioseismology — some of which can provide information about deep regions within the star.

Mathematical models of the Sun can be constructed from observational data to describe the solar structure and evolution. A Standard Solar Model (SSM) is based on observational parameters such as the solar age, mass, radius and surface luminosity (given in

[1] The Hertzsprung-Russell diagram is a luminosity versus surface temperature diagram. In this diagram, most stars fall under a narrow region called the Main Sequence [2]. The Main Sequence of this diagram is where a star spends most of its lifetime while its main energy source is the fusion of hydrogen into helium.

[2] One parsec (pc) is equivalent to 3.26 light-years or 3.09×10^{13} km. It is defined as the distance for an astrophysical object to have an annual parallax of one arcsecond.

Table 1.1) as well as the cross sections governing the nuclear reaction rates. Other input parameters are [3]:

- Chemical Abundance: The abundance of different chemical elements affects the energy transport in the Sun and hence its temperature and density profiles. Since only the surface chemical abundances are measurable, two assumptions are made regarding this parameters: (a) the Sun is chemically homogeneous when it enter the Main Sequence and (b) the current surface composition reflects the initial abundances of all elements up to carbon.

- Radiative Opacities: Since the energy transport in the innermost regions of the Sun happens mainly through radiation, the opacity of the solar matter to the propagation of photons is an important input parameter which influences, for instance, the temperature profile of the star. The radiative opacities are calculated both from (a) the assumed chemical abundances in the solar matter and (b) from modeling the interactions between atoms and radiation.

- Equation of State: The behavior of the solar matter and the relation between its pressure, temperature, density, and other properties must take into account several effects including, for example, (a) radiation pressure and (b) electron degeneracy.

Besides the input parameters, some other approximations and assumptions are made in the SSMs:

- Hydrostatic Equilibrium: The Sun is assumed to be in hydrostatic equilibrium, that is, the inwards force of gravity is balanced by the outwards pressure of the hot gas.

- Energy Generation: The main process responsible for the energy generation in the Sun are thermonuclear fusion reactions.

- Energy Transport: Energy produced in the interior of the Sun is transported outwards either by radiation or convection.

- Changes in Abundance: The chemical abundances in the Sun are supposed to change only due to nuclear reactions in regions in which there are no convective movement of the solar matter.

The SSM is finally obtained after simulating the solar environment and evolution using the inputs and assumptions above. The final product are the physical quantities that define the model [3]: (a) temperature, (b) density, (c) pressure and (d) the integrated luminosity of the Sun. The profile for the first three is shown in Figure 1.1. Additionally, the SSM also provides the spectra of acoustic oscillations of the surface of the Sun — which can be verified

Table 1.1: Solar parameters [4], some of which are input parameters used in the SSM while others result from the BS05(OP) [5] SSM.

Parameter	Value	Unit
Age	4.57×10^9	years
Mass	1.988×10^{30}	kg
Equatorial Radius	6.957×10^8	m
Surface Luminosity	3.828×10^{26}	W
Surface Effective Temperature	5772	K
Core Density ρ_c	152.9	$g \cdot cm^{-3}$
Core Temperature T_c	1.567×10^7	K
Core Pressure P_c	2.357×10^{17}	$dyn \cdot cm^{-2}$

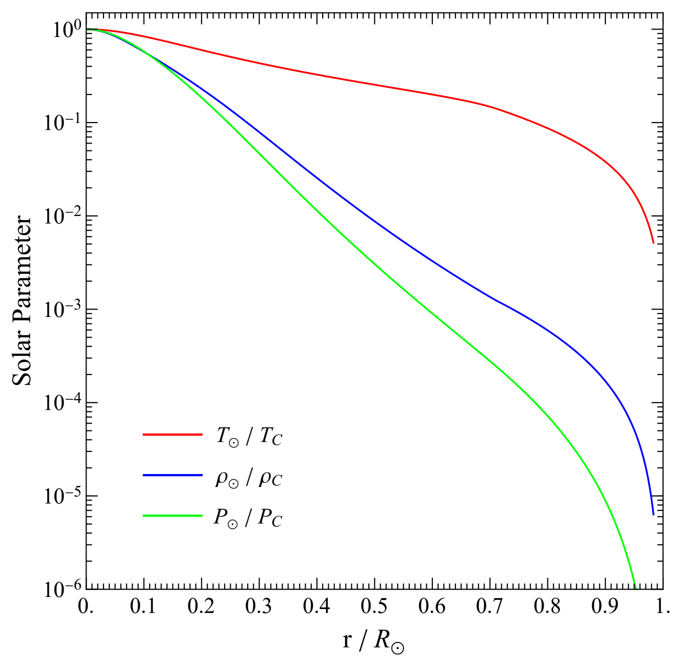

Figure 1.1: Physical quantities — temperature, density, and pressure — of the Sun which are results from the BS05(OP) [5] SSM. ρ_c, T_c and P_c are the values of these quantities in the solar core and are given in Table 1.1.

by helioseismological studies — and the fluxes of neutrinos produced in the fusion reactions, which can me measured in solar neutrino experiments.

From astronomical and helioseismological data, as well from the SSM simulations, the structure of the Sun can be divided in a variety of regions, among which the following can be highlighted:

- Core ($0 \leq r \leq 0.25R_\odot$): The innermost region of the Sun and where the thermonuclear fusion reactions take place. At its centre, temperature and density reaches around $1.6 \times 10^7\,\mathrm{K}$ and $150\,\mathrm{g \cdot cm^{-3}}$ respectively.

- Radiative Zone ($0.25R_\odot < r \leq 0.7R_\odot$): In this region the energy produced in the core is transported to the outer regions in the form of radiation diffusion, with photons being continuously absorbed and re-emitted by atoms in the medium.

- Convective Zone ($0.7R_\odot < r \leq R_\odot$): In this region the energy is transported to the solar surface in the form of heat by convection of the hot gas.

- Photosphere: The region where the visible light observed from the Sun is produced. This region thickness is of the order of $10^4\,\mathrm{km}$, and it has an effective temperature[3] of around $6 \times 10^3\,\mathrm{K}$ and a density of $2 \times 10^{-4}\,\mathrm{kg \cdot m^{-3}}$ [6].

Above the Photosphere, the Chromosphere extends to a few thousand kilometers, and the Corona extends up to 2 solar radii above the solar surface. Both regions are less dense but hotter than the Photosphere below. The heating of those regions are supposed to be due to variable magnetic fields originated in the photosphere which transport and accelerate particles to the upper regions [2].

1.2 Fusion Processes and Neutrino Fluxes

The Sun is powered by the energy released by thermonuclear fusion reactions of light elements that happen in its core. The energy release comes from the difference in mass between the reacting and product nuclei, since the total mass of a nucleus is less than the sum of the masses of its constituents [7]:

$$m(A,Z) = Zm_\mathrm{p} + (A-Z)m_\mathrm{n} - B(A,Z)\,, \tag{1.1}$$

where Z is the atomic number, A is the atomic mass, B is the binding energy of the nucleus, m_p and m_n are the masses of protons and neutrons respectively. The overall result of the nuclear

[3]Effective temperature is the temperature a black body of the same size would have to be to emit the same luminosity as the Sun.

fusion processes in the Sun is the reaction $4\,\mathrm{p} \to {}^{4}\mathrm{He} + 2\,\mathrm{e}^{+} + 2\,\nu_{\mathrm{e}} + \gamma$ and the energy released

$$Q = 4m_{\mathrm{p}} - 2m_{\mathrm{e}} - m_{^{4}\mathrm{He}} \approx 26\,\mathrm{MeV} \tag{1.2}$$

is carried out by photons and in a small part by neutrinos, which are also a by-product of the nuclear fusion reactions. There are two main sets of reactions that happen in Main Sequence Stars, such as the Sun: the Proton-Proton (pp) chain and the Carbon-Nitrogen-Oxygen (CNO) cycle.

The complete set of reactions of the pp chain is depicted in Figure 1.2. The main reaction branch of the pp chain is

$$\begin{gathered} \mathrm{p} + \mathrm{p} \to {}^{2}\mathrm{H} + \mathrm{e}^{+} + \nu_{\mathrm{e}} \\ \Downarrow \\ {}^{2}\mathrm{H} + \mathrm{p} \to {}^{3}\mathrm{He} + \gamma \\ \Downarrow \\ {}^{3}\mathrm{He} + {}^{3}\mathrm{He} \to {}^{4}\mathrm{He} + 2\,\mathrm{p}. \end{gathered}$$

The energy release rate in this process is roughly $Q_{\mathrm{pp}} \propto T^{4}$, defined by the time-scale of the first and slowest reaction of the chain which is almost 10^{10} years [8].

The CNO cycle also transforms four hydrogen atoms into one helium atom, releasing energy in the form of photons and neutrinos, using the $^{12}\mathrm{C}$ atom as a catalyst of the process. The complete set of reactions of the CNO cycle is pictured in Figure 1.3. The three neutrino producing reactions are

$$\begin{aligned} &{}^{13}\mathrm{N} \to {}^{13}\mathrm{C} + \mathrm{e}^{+} + \nu_{\mathrm{e}}\,, \\ &{}^{15}\mathrm{O} \to {}^{15}\mathrm{N} + \mathrm{e}^{+} + \nu_{\mathrm{e}} \text{ and} \\ &{}^{17}\mathrm{F} \to {}^{17}\mathrm{O} + \mathrm{e}^{+} + \nu_{\mathrm{e}}\,. \end{aligned}$$

The energy release rate in the CNO cycle is $Q_{\mathrm{CNO}} \propto T^{16}$ [8]. Although the energy release rate in the CNO cycle is higher, it is not the main process happening inside the Sun. The dominant process is dependent on the temperature in the core of the star and hence on its mass. In more massive stars, with hotter cores, the electrons have higher kinetic energy which enables them to win over the coulombian repulsion from heavier nuclei. As such, in less massive stars such as the Sun, the dominant process is the pp chain.

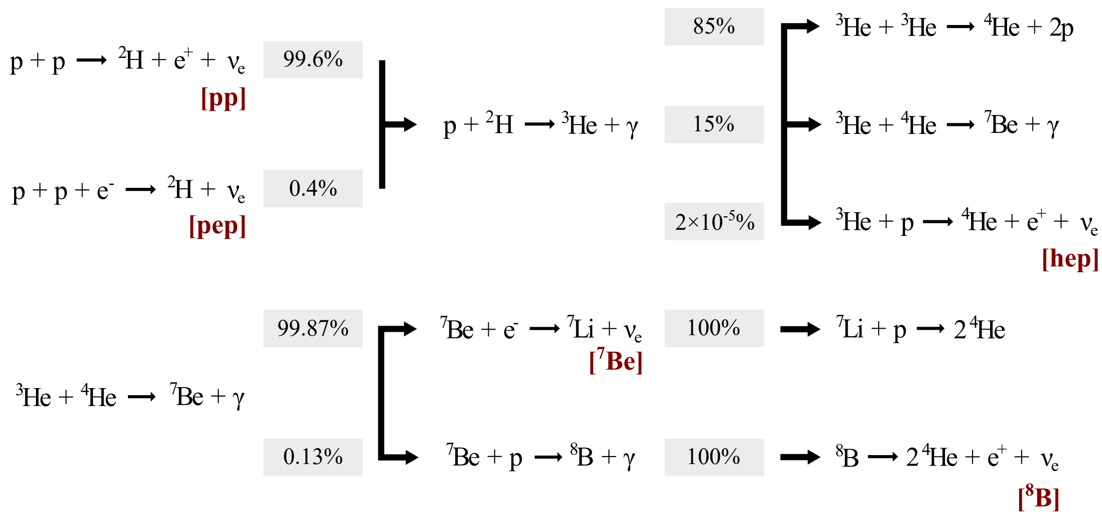

Figure 1.2: Set of reactions of the pp chain of stellar thermonuclear fusion reactions. Neutrino producing reactions are labeled In this process, the pp, hep and ^{8}B neutrinos that are emitted in continuous spectra while the pep and ^{7}Be neutrinos are emitted in monochromatic spectra. Neutrino fluxes are plotted in Figure 1.4 for the BS05(OP) [5] SSM.

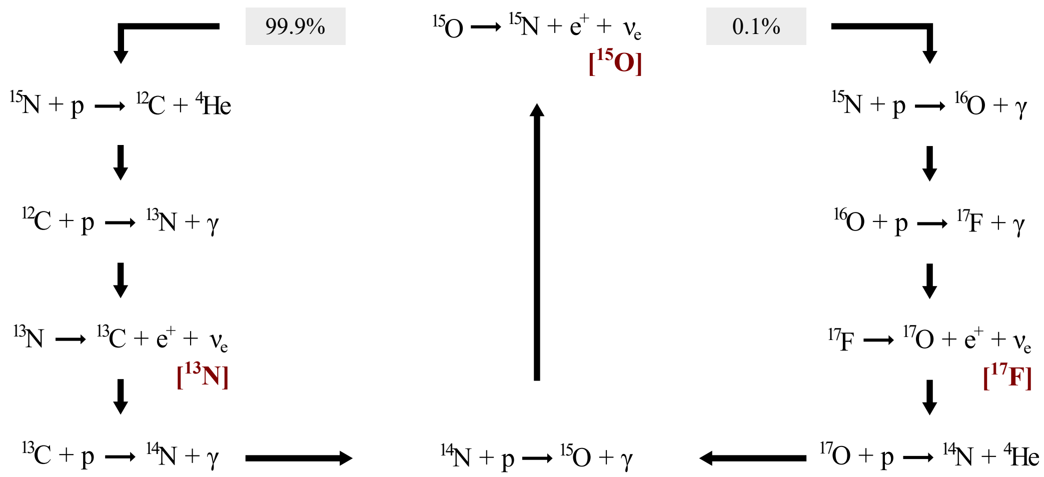

Figure 1.3: Set of reactions of the CNO cycle of stellar thermonuclear fusion reactions. Neutrino producing reactions are labeled All neutrinos fluxes in this process — ^{13}N, ^{15}O, ^{17}F — are produced in continuous spectra. Neutrino fluxes are plotted in Figure 1.4 for the BS05(OP) [5] SSM.

Electron neutrinos are a by-product of the thermonuclear fusion reactions that power the Sun as it can be seen in Figures 1.2 and 1.3. Such neutrinos are produced in very particular spectra, both continuous and monochromatic, and are named after the reaction in which they are produced. In the pp chain, the pp, hep and ^{8}B neutrinos are emitted in continuous spectra while the pep and ^{7}Be are monochromatic. In the CNO cycle, all neutrinos fluxes — called ^{13}N, ^{15}O, ^{17}F — are produced in continuous spectra. All fluxes are shown in Figure 1.4. Table 1.2 shows the neutrino producing reactions from the pp chain and CNO cycle, the produced neutrinos' average and maximum energies as well as the fluxes calculated in the BS05(OP) SSM. Due to the temperature dependency of each reaction, different fractions of each neutrino flux are produced at a different depths within the solar core, as shown in Figure 1.5.

The neutrinos produced in the solar core propagate outwards, leaving the Sun and traveling through the interplanetary media until they reach Earth where they can be detected. Photons are continually scattered in electromagnetic processes in the solar medium, consequently losing the information of their initial state and taking upwards of 10^5 years to reach the surface of the Sun [9]. Neutrinos, on the other hand, do the same in around 2 s due to their low interaction cross sections with the solar matter, bringing information directly from the inner regions of the Sun. As such, solar neutrinos were historically regarded as a potential evidence for the solar fusion reactions, driving the interest in their detection, which was finally achieved in the 1970s with the results from the Homestake [10] experiment. However, as it will be discussed in the Chapter 2, the detection of solar neutrinos brought to light several new questions to the understanding of the Sun and of neutrinos themselves.

Table 1.2: Reactions from the pp chain and CNO cycle that produce the solar neutrino fluxes, including the neutrino's average and maximum energies [7] as well as the fluxes reported by the BS05(OP) [5] SSM.

	Reaction	Average Neutrino Energy [MeV]	Maximum Neutrino Energy [MeV]	Predicted Neutrino Flux [$\mathrm{cm^{-2} \cdot s^{-1}}$]
pp	$\mathrm{p + p \rightarrow {}^{2}H + e^{+} + \nu_e}$	0.2668	0.423	5.99×10^{10}
pep	$\mathrm{p + e^{-} + p \rightarrow {}^{2}H + \nu_e}$	1.445	1.445	1.42×10^{8}
hep	$\mathrm{{}^{3}He + p \rightarrow {}^{4}He + e^{+} + \nu_e}$	9.628	18.778	7.93×10^{3}
^{7}Be	$\mathrm{e^{-} + {}^{7}Be \rightarrow {}^{7}Li + \nu_e}$	0.3855 (0.8631)	0.3855 (0.8631)	4.84×10^{9}
^{8}B	$\mathrm{{}^{8}B \rightarrow 2\,{}^{4}He + e^{+} + \nu_e}$	6.735	~ 15	5.69×10^{6}
^{13}N	$\mathrm{{}^{13}N \rightarrow {}^{13}C + e^{+} + \nu_e}$	0.7063	1.1982	3.07×10^{8}
^{15}O	$\mathrm{{}^{15}O \rightarrow {}^{15}N + e^{+} + \nu_e}$	0.9964	1.7317	2.33×10^{8}
^{17}F	$\mathrm{{}^{17}F \rightarrow {}^{17}O + e^{+} + \nu_e}$	0.9977	1.7364	5.84×10^{6}

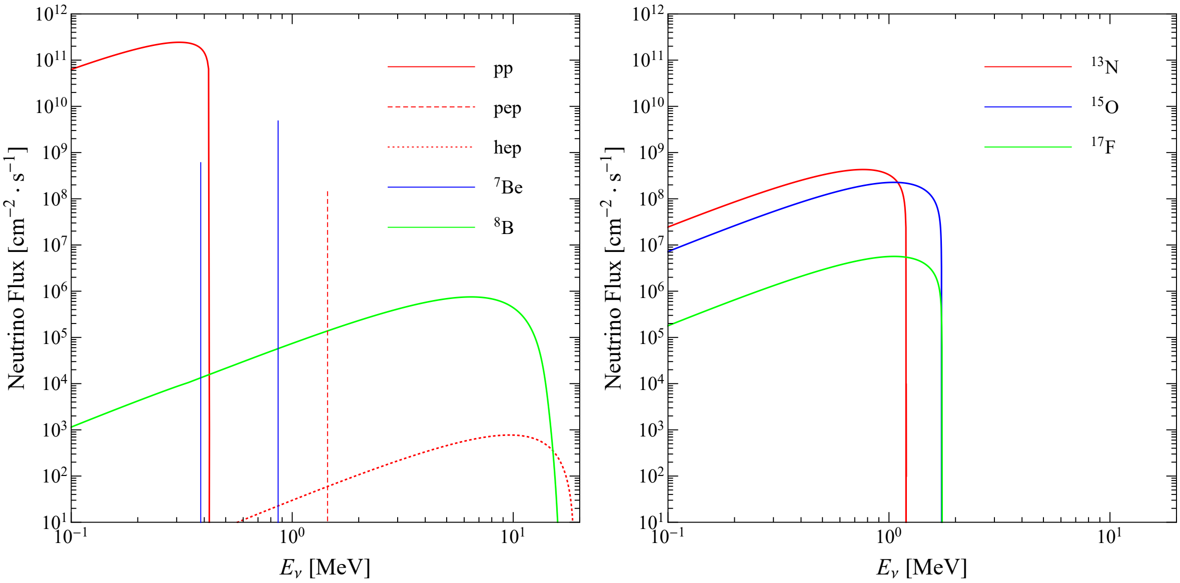

Figure 1.4: Energy spectra of solar neutrinos produced in the pp chain (left) and in the CNO cycle (right) for the BS05(OP) [5] SSM.

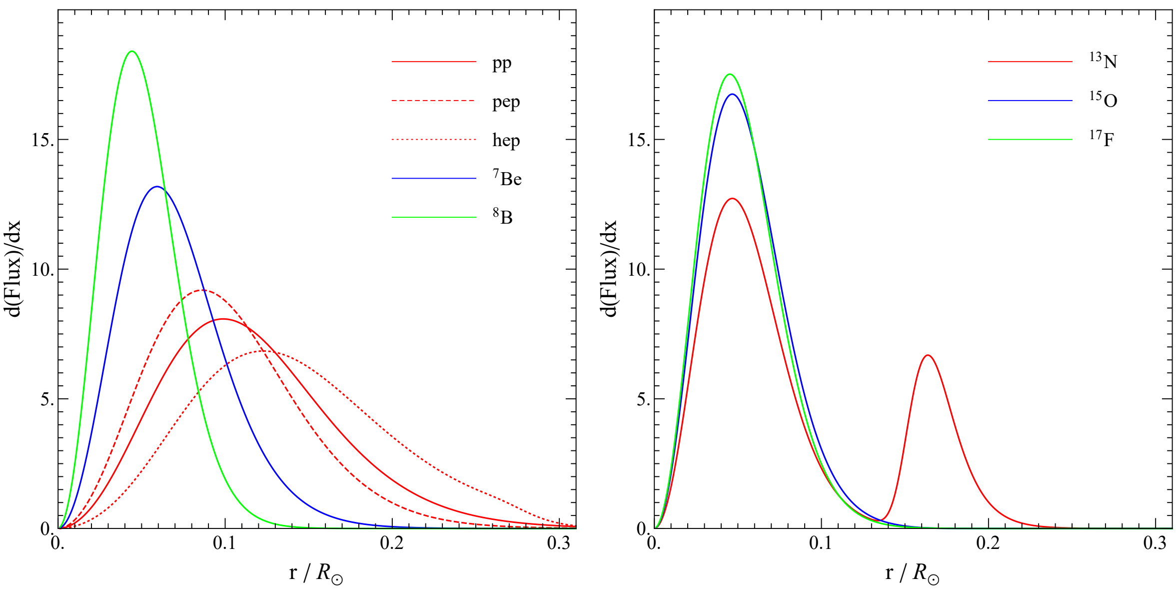

Figure 1.5: Distributions for the fraction of each neutrino flux produced at a given radius in the pp chain (left) and in the CNO cycle (right) for the BS05(OP) [5] SSM. Remarkably, the ^{13}N profile has two peaks: the first for where the reactions are approximately in steady state and the second for residual $^{12}C + p \rightarrow ^{13}N + \gamma$ at radii where the temperature is too low for the subsequent reactions [11].

Chapter 2

Solar Neutrino Oscillations

As seen in Chapter 1, solar neutrinos are produced in the thermonuclear fusion processes that power the Sun. In such reactions, four protons are converted into Helium through several intermediate steps, some of which generate neutrinos in very particular spectra — both continuous and monochromatic. The early experiments detecting these neutrinos indicated a lower flux than the predicted by the SSMs. This deficit became known as the Solar Neutrino Problem (SNP).

The solution to the SNP was sought in both solar and particle physics, leading to several models aiming to accurately describe the available data. Over the years, results from neutrino experiments eventually established the Neutrino Flavor Oscillation model with Large Mixing Angle and Mikheyev-Smirnov-Wolfenstein Resonant Flavor Conversion (LMA-MSW) as the solution to the SNP.

In this Chapter, an overview of the experiments designed for the detection of solar neutrinos is presented, the neutrino oscillation phenomenon is described, both in vacuum and in matter, and it is applied in the propagation of solar neutrinos from production to detection.

2.1 Neutrino Experiments and the Solar Neutrino Problem

The Homestake [10] chlorine neutrino experiment was the first to detect solar neutrinos and also the first to hint at the SNP. This experiment was proposed and built in the 1960s and early results [12] already indicated a neutrino flux of about one-third the predicted by SSMs. The Homestake detection signature was based on the inverse β decay reaction $\nu_e + {}^{37}\mathrm{Cl} \to {}^{37}\mathrm{Ar} + \mathrm{e}^-$, which has a threshold of $0.814\,\mathrm{MeV}$. Because of that, the experiment was sensitive to the higher energy ^{7}Be line, the pep line, and the ^{8}B spectrum, which was the main contribution to the detected flux. In this kind of experiment, the solar neutrino flux is measured by extracting and counting the Argon atoms that are produced in the reaction. The average solar neutrino rate measured by Homestake between March 1970 and February 1994 was [10]

$$R_{\mathrm{HS}}^{\mathrm{exp}} = 2.56 \pm 0.16\,(\mathrm{stat.}) \pm 0.16\,(\mathrm{syst.})\,\mathrm{SNU}^{1}\,, \tag{2.1}$$

whereas the predicted rate for Homestake at that time, by Bahcall and Pinsonneault [10, 13], was $R_{^{37}\mathrm{Cl}} = 9.3^{+1.2}_{-1.4}$ SNU.

The same principle of the Homestake experiment was applied in other experiments but using the the reaction $\nu_e + {}^{71}\mathrm{Ga} \to {}^{71}\mathrm{Ge} + \mathrm{e}^-$. Such is the case of GALLEX [14] and its successor GNO [15], and SAGE [16] experiments. The 0.233 MeV threshold for the reaction makes these experiments sensitive to all of the solar neutrino spectra. The average solar neutrino rate measured by GALLEX and GNO between May 1991 and April 2003 was [15]

$$R_{\mathrm{GG}}^{\mathrm{exp}} = 69.3 \pm 4.1\,(\mathrm{stat.}) \pm 3.6\,(\mathrm{syst.})\,\mathrm{SNU}\,, \tag{2.2}$$

while for the SAGE experiment, the average solar neutrino rate between January 1990 and December 2007 was [16]

$$R_{\mathrm{SG}}^{\mathrm{exp}} = 65.4\,^{+3.1}_{-3.0}\,(\mathrm{stat.})\,^{+2.6}_{-2.8}\,(\mathrm{syst.})\,\mathrm{SNU}\,, \tag{2.3}$$

whereas the predicted rate for the Gallium experiments would be [7] $R_{^{71}\mathrm{Ga}} = 118.88\,\mathrm{SNU}$ in the BSB05(AGS05) SSM [11].

Another class of experiments are the Water Cherenkov detectors. In this kind of experiment, neutrinos are detected through the measurement of Cherenkov light emitted by electrons traversing a medium with speeds above the local speed of light. These electrons are either elastically scattered ($\nu + e^- \to \nu + e^-$) or inelastically produced ($\nu + X \to Y + e^-$) by the incoming neutrinos. Due to the characteristics of the Cherenkov light, this kind of experiment is sensitive to both direction and energy of the incoming neutrinos.

The Kamioka Nucleon Decay Experiment — Kamiokande — experiment is a water Cherenkov detector that was first designed for the detection of proton decay (Kamiokande-I) [17] and started operating in 1983. Later, in 1986, it was upgraded and optimized to observe ^{8}B solar neutrinos (Kamiokande-II) [18, 19], operating from January, 1987, to April, 1990. The last phase (Kamiokande-III) operated from December 1990 and February 1995. The average flux of ^{8}B neutrinos measured in phases II and III are [20]

$$\Phi_{\mathrm{KDE}}^{^8\mathrm{B}} = [2.80 \pm 0.19\,(\mathrm{syst.}) \pm 0.33\,(\mathrm{stat.})] \times 10^6\,\mathrm{cm}^{-2} \cdot \mathrm{s}^{-1}\,, \tag{2.4}$$

with the corresponding number of 390^{+35}_{-33} neutrino events, which is about half the expected at the time, by Bahcall and Pinsonneault [20, 21], at 785 neutrino events.

The Super-Kamiokande (SK) experiment is a water Cherenkov detector built as a successor to the the Kamiokande experiment. The SK experiment started operating in April

[1] A Solar Neutrino Unit (1 SNU) corresponds to 10^{-36} events per target atom per second.

1996, divided in four phases. SK-I [22] collected data from April 1996 to July 2001. SK-II [23] ran from December 2002 to October 2005. Next, SK-III [24] ran from October 2006 to August 2008. Finally, SK-IV [25] started collecting data in September 2008 and ran until May 2018 [26]. The measured flux combining all phases, up to February 2014, was

$$\Phi^{\text{SK}}_{^8\text{B}} = [2.345 \pm 0.014\,(\text{syst.}) \pm 0.036(\text{stat.})] \times 10^6\,\text{cm}^{-2} \cdot \text{s}^{-1}\,. \tag{2.5}$$

Refurbishment work started in June 2018 for the addition of Gadolinium (Gd) into the detector to improve neutrino detection [27]. On January 2019, data for this fifth phase (SK-V) started being collected [26].

Another experiment in this category is the Sudbury Neutrino Observatory (SNO) experiment. SNO is a heavy-water (D_2O) Cherenkov detector also designed to measure the ^{8}B solar neutrinos through three different methods:

(i) the elastic scattering $\nu_\alpha + \text{e}^- \to \nu_\alpha + \text{e}^-$ as used in the regular water Cherenkov experiments, where ν_α represents any neutrino flavor;

(ii) the charged current reaction $\nu_e + \text{D} \to \text{p} + \text{p} + \text{e}^-$, which is used to measure the energy spectrum of electron neutrinos by measuring the kinetic energy of the product electrons;

(iii) and the neutral current reaction $\nu_\alpha + \text{D} \to \text{p} + \text{n} + \nu_\alpha$, which measures the energy spectrum of neutrinos from the detection of the product neutrons.

This last reaction is essential for verifying the neutrino oscillation solution to the SNP because it is equally sensitive to all active neutrino flavors. As such, three different phases were planned for the SNO experiment, based on ways of improving the detection of the neutrons from these NC reactions in (iii).

The first phase [28] was based on the capture of the neutrons by the deuterium $\text{n} + \text{D} \to {}^3\text{He} + \gamma$ and which operated from November 1999, to May 2001. The second phase [29] was based on the neutron captured on chlorine atoms from NaCl added to the heavy water tank, which led to a statistical improvement to the measurement of NC reactions. This phase ran from July 2001, and August 2003. Finally, the third phase [30, 31] consisted in the inclusion in the heavy water tank of a grid of proportional ^{3}He counters, which also measured the neutron capture on helium. This last phase operated between November 2004 and November 2006. The results from this latter phase for each detection method are

$$\Phi^{^8\text{B,ES}}_{\text{SNO}} = [1.77\,^{+0.09}_{-0.10}\,(\text{syst.})\,^{+0.24}_{-0.21}\,(\text{stat.})] \times 10^6\,\text{cm}^{-2} \cdot \text{s}^{-1}\,, \tag{2.6}$$

$$\Phi^{^8\text{B,CC}}_{\text{SNO}} = [1.67\,^{+0.07}_{-0.08}\,(\text{syst.})\,^{+0.05}_{-0.04}\,(\text{stat.})] \times 10^6\,\text{cm}^{-2} \cdot \text{s}^{-1}\,, \tag{2.7}$$

$$\Phi^{^8\text{B,NC}}_{\text{SNO}} = [5.54\,^{+0.36}_{-0.34}\,(\text{syst.})\,^{+0.33}_{-0.31}\,(\text{stat.})] \times 10^6\,\text{cm}^{-2} \cdot \text{s}^{-1}\,. \tag{2.8}$$

From the combined analysis of the three phases [32] the flux of solar neutrinos of all flavors is

$$\Phi^{^8\mathrm{B}}_{\mathrm{SNO}} = [5.25\,^{+0.11}_{-0.13}\,(\mathrm{syst.}) \pm 0.16\,(\mathrm{stat.})] \times 10^6\,\mathrm{cm}^{-2} \cdot \mathrm{s}^{-1}\,, \tag{2.9}$$

which is compatible with SSM predictions. These results demonstrated that neutrinos indeed undergo flavor change between production and detection. As recognition for their discoveries, the SK and SNO Collaborations were awarded the 2015 Nobel Prize in Physics in the name of Takaaki Kajita (SK) and Arthur B. McDonald (SNO) [33].

Another class of neutrino experiments are the liquid scintillator experiments. In such experiments, a neutrino incident on the detector may elastically scatter off an electron in the medium. The charged particle traverse the matter exciting atoms and molecules on their path. Upon de-excitation, the atoms emit electromagnetic radiation. If not reabsorbed by the material, the radiation can be detected and provide information on the charged particle and, consequently, on the neutrino. This method allows the detection of low energy solar neutrinos similarly to the radiochemical methods while also allowing for spectral measurements and real-time detection which is possible with Water Cherenkov experiments [34].

One such experiment is Borexino [35], which started collecting data in May 2007 with the main goal of measuring the ^{7}Be solar neutrino line. By the end of its first phase [36], the experiment managed not only that [37], but also directly measured the pp [38] and pep [39, 40] neutrinos. Most recently, the collaboration reported the detection of neutrinos from the CNO cycle [41].

2.2 Neutrino Oscillations

During the investigation into the SNP, several models were created in both solar and particle physics with the objective to accurately describe the available data. Since the depletion of the neutrino flux was inconsistent across experiments, unknown errors could be affecting their results. Additionally, the understanding of the solar structure and neutrino production could be incomplete, demanding the modification of the solar models.

The phenomenon of neutrino oscillations was first proposed by Bruno Pontecorvo [42–44] in 1957, in analogy to the oscillations in the $K^0\bar{K}^0$ system [45–48], originally describing the oscillation between the electron neutrino - the only known neutrino flavour at the time - and the corresponding antineutrino. In 1962, with the discovery of the muon neutrino, Ziro Maki, Masami Nakagawa and Shoichi Sakata extended the oscillation model to two active neutrino flavours [49]. The standard neutrino oscillation theory was developed in the following years [50, 51].

2.2.1 Neutrino Oscillations in Vacuum

A neutrino of flavour ν_α is, by definition, the neutrino produced in charged current weak interactions, either on the interaction of a lepton l_α or alongside an antilepton $\bar{l}_\alpha$. Charged leptons are distinguished through their masses. However, since neutrinos are relativistic, they are distinguished through the detection of the associated charged lepton.

Thus, if neutrinos are massive and there are mass eigenstates ν_1, ν_2, ν_3... which are non-degenerate — that is, $m_1 \neq m_2 \neq m_3 \neq ...$ — it is possible to write a flavour eigenstate ν_α as a mixture, a linear combination of mass eigenstates [7]:

$$|\,\nu_\alpha\,\rangle = \sum_k U^*_{\alpha k}\,|\,\nu_k\,\rangle\,. \tag{2.10}$$

From the precise measurement of the so-called invisible decay width of the Z boson, the number of neutrino flavors lighter than $m_Z/2$ participating in weak interactions is restricted to three [52]. By taking into account only these three species — denoted ν_e, ν_μ and ν_τ — the coefficients $U^*_{\alpha k}$ in Equation (2.10) are the elements of a 3×3 matrix, called Pontecorvo-Maki-Nakagawa-Sakata (PMNS) mixing matrix, which can be parametrized by three mixing angles and CP-violating phases, one for Dirac neutrinos and three for Majorana neutrinos. The PMNS mixing matrix $\mathbf{U}$ can be written as

$$\mathbf{U} = \mathbf{R_{23}}\,\mathbf{R_{13}}\,\mathbf{R_{12}}\,\mathbf{D_M}\,, \tag{2.11}$$

where the matrices $\mathbf{R_{ij}}$ are given by

$$\mathbf{R_{12}} = \begin{pmatrix} c_{12} & s_{12} & 0 \\ -s_{12} & c_{12} & 0 \\ 0 & 0 & 1 \end{pmatrix}, \quad \mathbf{R_{13}} = \begin{pmatrix} c_{13} & 0 & s_{13}e^{-i\delta} \\ 0 & 1 & 0 \\ -s_{13}e^{i\delta} & 0 & c_{13} \end{pmatrix}, \quad \mathbf{R_{23}} = \begin{pmatrix} 1 & 0 & 0 \\ 0 & c_{23} & s_{23} \\ 0 & -s_{23} & c_{23} \end{pmatrix},$$

with $s_{ij} = \sin\theta_{ij}$ and $c_{ij} = \cos\theta_{ij}$, where θ_{ij} are mixing angles and δ is the CP violation phase, also called Dirac phase. Additionally, the matrix $\mathbf{D_M}$ is given by

$$\mathbf{D_M} = \begin{pmatrix} e^{i\eta_1} & 0 & 0 \\ 0 & e^{i\eta_2} & 0 \\ 0 & 0 & 1 \end{pmatrix},$$

where η_1, η_2 are called the Majorana phases and they do not contribute to neutrino oscillations

— see Equation (2.28). Hence, neglecting the Majorana phases, Equation (2.11) becomes

$$\mathbf{U} = \begin{pmatrix} c_{12}c_{13} & s_{12}c_{13} & s_{13}e^{-i\delta} \\ -s_{12}c_{23} - c_{12}s_{23}s_{13}e^{i\delta} & c_{12}c_{23} - s_{12}s_{23}s_{13}e^{i\delta} & s_{23}c_{13} \\ s_{12}s_{23} - c_{12}c_{23}s_{13}e^{i\delta} & -c_{12}s_{23} - s_{12}c_{23}s_{13}e^{i\delta} & c_{23}c_{13} \end{pmatrix} . \tag{2.12}$$

The mass eigenstates in Equation (2.10) are the eigenstates of the Hamiltonian:

$$\mathscr{H}\,|\,\nu_k\,\rangle = E_k\,|\,\nu_k\,\rangle\,, \quad \text{with } E_k = \sqrt{|\vec{p}|^2 + m_k^2}. \tag{2.13}$$

And the evolution of the eigenstates is obtained from Schrödinger's equation as

$$|\,\nu_k(t)\,\rangle = e^{-iE_k t}\,|\,\nu_k\,\rangle\,. \tag{2.14}$$

Thus

$$|\,\nu_\alpha(t)\,\rangle = \sum_k U^*_{\alpha k}\,|\,\nu_k(t)\,\rangle = \sum_k U^*_{\alpha k}\,e^{-iE_k t}\,|\,\nu_k\,\rangle\,. \tag{2.15}$$

From the unitarity of the mixing matrix $\mathbf{U}$, one obtains the inverse transformation to Equation (2.10):

$$|\,\nu_k\,\rangle = \sum_\beta U_{\beta k}\,|\,\nu_\beta\,\rangle\,, \tag{2.16}$$

from which one can write:

$$|\,\nu_\alpha(t)\,\rangle = \sum_\beta \sum_k U^*_{\alpha k}\,e^{-iE_k t} U_{\beta k}\,|\,\nu_\beta\,\rangle\,, \tag{2.17}$$

that is, a neutrino produced in a flavour eigenstate $|\,\nu_\alpha\,\rangle$, since it is a linear combination of mass eigenstates, is described as a superposition of flavour eigenstates at a time t after its production. The transition amplitude between states is given by

$$A_{\nu_\alpha \to \nu_\beta} = \langle\,\nu_\beta\,|\,\nu_\alpha(t)\,\rangle = \sum_k U^*_{\alpha k} U_{\beta k}\,e^{-iE_k t}\,. \tag{2.18}$$

Thus, the probability that a neutrino produced in a flavour eigenstate ν_α be detected in a flavor eigenstate ν_β , at a time t after its production, is

$$P_{\nu_\alpha \to \nu_\beta}(t) = |A_{\nu_\alpha \to \nu_\beta}|^2 = \sum_j \sum_k U^*_{\alpha k} U_{\beta k} U_{\alpha j} U^*_{\beta j}\,e^{-i(E_k - E_j)t}\,. \tag{2.19}$$

Since neutrinos are ultra-relativistic, one can make the approximation

$$E_k = \left(|\,\vec{p}_k\,|^2 + m_k^2\right)^{1/2} \approx E + \frac{m_k^2}{2E}\,, \tag{2.20}$$

where $|\vec{p}_k| = E$ is the neutrino energy neglecting the mass contribution [7]. Hence

$$E_k - E_j \approx \frac{1}{2E}\left(m_k^2 - m_j^2\right) = \frac{\Delta m_{kj}^2}{2E}\,, \tag{2.21}$$

where Δm_{kj}^2 is called the mass-squared difference between mass eigenstates k and j. In addition, if L is the distance traversed by the neutrinos between production and detection, one can write $L \approx t$. Thus

$$P_{\nu_\alpha \to \nu_\beta}(L,E) = \sum_{k,j} U_{\alpha k}^* U_{\beta k} U_{\alpha j} U_{\beta j}^* \exp\left(-i\frac{\Delta m_{kj}^2}{2E}L\right). \tag{2.22}$$

Equation (2.22) can be rewritten as

$$P_{\nu_\alpha \to \nu_\beta}(L,E) = \sum_k |U_{\alpha k}|^2 |U_{\beta k}|^2 + 2\mathrm{Re}\left[\sum_k \sum_{j<k} U_{\alpha k}^* U_{\beta k} U_{\alpha j} U_{\beta j}^* \exp\left(-2\pi i\frac{L}{L_{kj}^{\mathrm{osc}}}\right)\right], \tag{2.23}$$

where $L_{kj}^{\mathrm{osc}} = 4\pi E/\Delta m_{kj}^2$ is the distance at which the phase generated by the mass-squared difference Δm_{kj}^2 becomes equal to 2π.

The same procedure can be followed for antineutrinos starting with

$$|\bar{\nu}_\alpha\rangle = \sum U_{\alpha k}|\bar{\nu}_k\rangle\,, \tag{2.24}$$

for which it is found that

$$P_{\bar{\nu}_\alpha \to \bar{\nu}_\beta}(L,E) = \sum_k |U_{\alpha k}|^2 |U_{\beta k}|^2 + 2\mathrm{Re}\left[\sum_k \sum_{j<k} U_{\alpha k} U_{\beta k}^* U_{\alpha j}^* U_{\beta j} \exp\left(-2\pi i\frac{L}{L_{kj}^{\mathrm{osc}}}\right)\right]. \tag{2.25}$$

From Equations (2.13) and (2.20), we consider the evolution of two mass eigenstates ν_1 and ν_2 [53]:

$$i\frac{d}{dx}\begin{pmatrix}\nu_1\\ \nu_2\end{pmatrix} = \mathbf{H}\begin{pmatrix}\nu_1\\ \nu_2\end{pmatrix} = \begin{pmatrix}E_1 & 0\\ 0 & E_2\end{pmatrix}\begin{pmatrix}\nu_1\\ \nu_2\end{pmatrix} = \left[E\,\mathbf{I} + \frac{1}{2E}\mathbf{M}\right]\begin{pmatrix}\nu_1\\ \nu_2\end{pmatrix}, \tag{2.26}$$

with $\mathbf{M} = \mathbf{diag}(m_1^2, m_2^2) = m_1^2\mathbf{I} + \mathbf{diag}(0, \Delta m_{21}^2)$. The quantities $E\mathbf{I}$ and $m_1^2\mathbf{I}$ result in overall phases which are not observable and can be rotated out by a change of base, resulting in

$$i\frac{d\nu_{\mathrm{M}}}{dx} = \frac{1}{2E}\mathbf{M}\nu_{\mathrm{M}}\,. \tag{2.27}$$

Now, multiplying both sides by $\mathbf{U}$ and using $\mathbf{U}^\dagger\,\mathbf{U} = \mathbf{I}$, it is finally obtained that

$$i\frac{d\nu_{\mathrm{F}}}{dx} = \frac{1}{2E}\mathbf{U}\mathbf{M}\mathbf{U}^\dagger\nu_{\mathrm{F}}\,, \tag{2.28}$$

from which

$$\mathbf{H}_{\text{vac}} = \frac{1}{2E}\mathbf{U}\mathbf{M}\mathbf{U}^{\dagger}\,, \tag{2.29}$$

is identified as the Hamiltonian governing the evolution of neutrinos in the flavor basis and the consequent flavor oscillations in vacuum. For antineutrinos, the Hamiltonian is obtained by complex conjugation:

$$\mathbf{H}_{\text{vac}} = \frac{1}{2E}(\mathbf{U}\mathbf{M}\mathbf{U}^{\dagger})^{*}\,. \tag{2.30}$$

In the absence of CP violation, the vacuum Hamiltonian for neutrinos and antineutrinos are the same. For three neutrino flavors, the mass-squared difference matrix $\mathbf{M}$ is written as

$$\mathbf{M} = \mathbf{diag}(0, \Delta m^2_{21}, \Delta m^2_{31})\,. \tag{2.31}$$

As it can been seen, neutrino oscillations are not sensitive to the absolute scale of neutrino masses, but only to the squared-mass differences such as Δm^2_{21} and Δm^2_{31} which have been measured by a variety of neutrino oscillation experiments.

2.2.2 Neutrino Oscillations in Matter

When propagating in matter, neutrinos are subject to an effective potential due to weak charged (CC) and neutral current (NC) coherent forward elastic scatterings with particles in the medium, equivalent to an index of refraction which modifies their mixing [7].

For an electron neutrino propagating in a medium subject to coherent forward elastic CC scatterings, the potential V_{CC} is given by [7]

$$V_{\text{CC}} = \sqrt{2}\,G_F N_e\,, \tag{2.32}$$

where G_F is the Fermi constant and N_e is the electron number density.

In astrophysical environments with low temperature and density, such as the Sun and the Earth, matter is composed of neutrons, protons, and electrons. Electrical neutrality implies an equal number density of protons and electrons, and, consequently, the NC potentials os protons and electrons cancel each other. Hence, only neutrons contribute to the potential V_{NC} which is given by [7]

$$V_{\text{NC}} = -\frac{1}{2}\sqrt{2}\,G_F N_n\,, \tag{2.33}$$

where N_n is the neutron number density in the medium.

When taking into account this so-called matter effect to the neutrino oscillations, the oscillation Hamiltonian for three neutrino flavors is modified by

$$\mathbf{V} = \mathbf{diag}(V_{\text{CC}} + V_{\text{NC}}, V_{\text{NC}}, V_{\text{NC}})\,. \tag{2.34}$$

The term V_{NC} generates a phase common to all flavours which can be rotated out by a phase shift and hence

$$\mathbf{V} = \mathbf{diag}(V_{\mathrm{CC}}, 0, 0)\,. \tag{2.35}$$

The Hamiltonian for neutrino oscillations in matter is finally given on the flavour basis as

$$\mathbf{H}_{\mathrm{osc}} = \frac{1}{2E}\mathbf{U}\mathbf{M}\mathbf{U}^{\dagger} + \mathbf{V}\,. \tag{2.36}$$

In two neutrino families and for a constant matter potential, the evolution of the flavour eigenstates can be written from Equation (2.36):

$$i\frac{d}{dx}\begin{pmatrix} \nu_e \\ \nu_\mu \end{pmatrix} = \frac{1}{2E}\begin{pmatrix} -\Delta m^2 \sin^2\theta + 2EV_{CC} & \Delta m^2 \sin\theta\cos\theta \\ \Delta m^2 \sin\theta\cos\theta & \Delta m^2\cos^2\theta \end{pmatrix}\begin{pmatrix} \nu_e \\ \nu_\mu \end{pmatrix}, \tag{2.37}$$

which can be rewritten as

$$i\frac{d}{dx}\begin{pmatrix} \nu_e \\ \nu_\mu \end{pmatrix} = \frac{1}{4E}\begin{pmatrix} -\Delta m^2 \cos 2\theta + 2EV_{CC} & \Delta m^2 \sin 2\theta \\ \Delta m^2 \sin 2\theta & \Delta m^2\cos 2\theta - 2EV_{CC} \end{pmatrix}\begin{pmatrix} \nu_e \\ \nu_\mu \end{pmatrix} \tag{2.38}$$

The diagonalization of the Hamiltonian above lead to an effective Hamiltonian in the mass basis given by

$$\mathbf{H}_{\mathrm{M}} = \frac{1}{4E}\mathbf{diag}\left(-\Delta m_M^2, \Delta m_M^2\right)\,, \tag{2.39}$$

where:

$$\Delta m_{\mathrm{M}}^2 = \left[\left(\Delta m^2\cos 2\theta - 2EV_{\mathrm{CC}}\right)^2 + \left(\Delta m^2 \sin 2\theta\right)^2\right]^{1/2}\,, \tag{2.40}$$

is the effective mass-squared difference, and the effective mixing matrix in matter:

$$\mathbf{U}_{\mathrm{M}} = \begin{pmatrix} \cos\theta_{\mathrm{M}} & \sin\theta_{\mathrm{M}} \\ -\sin\theta_{\mathrm{M}} & \cos\theta_{\mathrm{M}} \end{pmatrix}, \tag{2.41}$$

with

$$\cos\theta_{\mathrm{M}} = \frac{\Delta m^2\cos 2\theta - 2EV_{\mathrm{CC}}}{\Delta m_{\mathrm{M}}^2} \quad \text{and} \quad \sin\theta_{\mathrm{M}} = \frac{\Delta m^2 \sin 2\theta}{\Delta m_{\mathrm{M}}^2}\,, \tag{2.42}$$

and hence

$$\tan 2\theta_M = \frac{\tan 2\theta}{\left(1 - \dfrac{2EV_{CC}}{\Delta m^2 \cos 2\theta}\right)}\,. \tag{2.43}$$

From Equation (2.43), it can be seen that there is a resonance for which the mixing angle becomes maximal ($\theta_{\mathrm{M}} = \pi/4$) when $V_{\mathrm{CC}} = \Delta m^2\cos 2\theta/(4E)$, that is, for

$$N_e = \frac{\Delta m^2 \cos 2\theta}{2\sqrt{2}EG_{\mathrm{F}}}\,. \tag{2.44}$$

This phenomenon is called the Mikheyev-Smirnov-Wolfenstein (MSW) effect [54–56]. For the most general case of a non-monochromatic neutrino spectrum and a continuously varying matter density (and for a given value of mass-squared difference), there will be sets of continuous values of neutrino energies and matter densities for which the resonance condition is satisfied. In such environments, there might exist transition between the effective mass eigenstates. This effect is measured, in two neutrino families, by an adiabaticity parameter defined as

$$\gamma = \frac{(\Delta m^2_{\mathrm{M}})^2}{\sin 2\theta_{\mathrm{M}} |\mathrm{dV_{CC}/dx}|} . \tag{2.45}$$

If $\gamma \gg 1$ throughout the neutrino trajectory, the evolution is adiabatic, that is, transitions between effective mass eigenstates are negligible. In the LMA parameter region, for the Sun and other environments with smoothly varying densities, neutrino evolution is adiabatic and the survival probability can be written as [7]:

$$P_{ee} = \frac{1}{2}\left(1 + \cos 2\theta_M^{(0)} \cos 2\theta\right) \tag{2.46}$$

where $\theta_M^{(0)}$ is the effective mixing angle at the point neutrino production and given by Equation (2.43) and θ is the mixing angle at the point of detection, assumed here to be in vacuum.

2.3 Oscillation Probabilities in the Sun and on Earth

Electron neutrinos are produced in the solar core from nuclear fusion reactions. They are produced in effective mass eigenstates governed by the matter potential at their point of production, and propagate outwards through the solar matter undergoing adiabatic transitions. Next, they propagate in interplanetary medium and are detected on Earth, either promptly "during the day" or after traversing a segment of the Earth's mantle and core "during the night" being subject to matter effects. The evolution of neutrino states are schematically represented in Figure 2.1. The survival and transition probabilities for solar neutrinos are discussed in this section.

The transition amplitude $A_{\nu_e \to \nu_\alpha} = A_{e\alpha}$ for an electron neutrino produced in the Sun to be detected on Earth as a neutrino of flavor α can be written as

$$A_{e\alpha} = \sum_i A^{\odot}_{ei} A^{\mathrm{vac}}_{ii} A^{\oplus}_{i\alpha} , \tag{2.47}$$

where $A^{\odot}_{ei}$ is the transition amplitude of an electron neutrino produced in the solar core to be in a ν_i state in the solar surface, A^{vac}_{ii} is the propagation amplitude between Sun and Earth surfaces, and $A^{\oplus}_{ie}$ is the transition amplitude of a ν_i to be in a ν_e state upon detection on Earth.

From Equations (2.14) and (2.20), the vacuum propagation amplitude of a i mass eigenstate is given as

$$A_{ii}^{\text{vac}} = \exp(-iE_k L) = \exp(-iEt)\exp\left(-i\frac{m_i^2}{2E}L\right), \tag{2.48}$$

where L is the distance from the surface of the Sun to the surface of the Earth.

The transition probability $P(\nu_e \to \nu_\alpha) = P_{e\alpha}$ is given as $P_{e\alpha} = |A_{e\alpha}|^2$, which, from Equation (2.47), is given in the context of two neutrino families as

$$P_{e\alpha} = |A_{e1}^{\odot}|^2 |A_{1\alpha}^{\oplus}|^2 + |A_{e2}^{\odot}|^2 |A_{2\alpha}^{\oplus}|^2 + \text{Re}\left[A_{e1}^{\odot} A_{1\alpha}^{\oplus} A_{e2}^{*\odot} A_{2\alpha}^{*\oplus} \exp\left(-i\frac{\Delta m_{21}^2}{2E}L\right)\right]. \tag{2.49}$$

In the LMA-MSW parameter region, the oscillation length $l_{\text{osc}} = 4\pi E/\Delta m_{21}^2$ is much shorter than the propagation length L and the phase in Equation (2.49) oscillates very rapidly. As such, the integration over finite neutrino energy bins during detection [57] leads to the averaging of oscillations equivalent to the an incoherent mixture of ν_1 and ν_2 eigenstates. Even for a fixed neutrino energy, the large size of the production region when compared to the oscillation length and the lack of knowledge about the neutrino production point leads to the averaging of oscillations [57]. Thus, one can simply write the incoherent sum of probabilities:

$$P_{e\alpha} = P_{e1}^{\odot} P_{1\alpha}^{\oplus} + P_{e2}^{\odot} P_{2\alpha}^{\oplus}, \tag{2.50}$$

where $P_{ei}^{\odot} = |A_{ei}^{\odot}|^2$ and $P_{i\alpha}^{\oplus} = |A_{i\alpha}^{\oplus}|^2$ from Equation (2.47), with $P_{ei}^{\odot}$ the probability of the produced ν_e be found as a ν_i at the surface of the Sun, $P_{i\alpha}^{\oplus}$ the probability of a ν_i be detected as a ν_α on Earth. Unitarity implies that $\sum_i P_{ei}^{\odot} = 1$ and $\sum_\alpha P_{i\alpha}^{\oplus} = 1$.

2.3.1 Oscillations in Three Neutrino Families

In the context of three neutrino families, the survival and conversion probabilities can be written, as in the previous case averaging over fast oscillations, as

$$P_{e\alpha} = \sum_i P_{ei}^{\odot} P_{i\alpha}^{\oplus}. \tag{2.51}$$

Due to the nature of the interactions of each neutrino flavor in matter, neutrino experiments can usually only differentiate between electronic and non-electronic flavors. Hence, it is useful to simplify the expression above as follows. The evolution equation for the flavor states in three families is given as

$$i\frac{d\nu}{dt} = \frac{1}{2E}\left[\mathbf{U}\mathbf{M}\mathbf{U}^{\dagger} + \mathbf{V}\right]\nu, \tag{2.52}$$

where $\nu = (\nu_e, \nu_\mu, \nu_\tau)$ is a column matrix of the neutrino flavor states, $\mathbf{U}$ is the PMNS mixing matrix, $\mathbf{M}^2$ is the mass-squared difference matrix and $\mathbf{V}$ is the matrix describing matter effects.

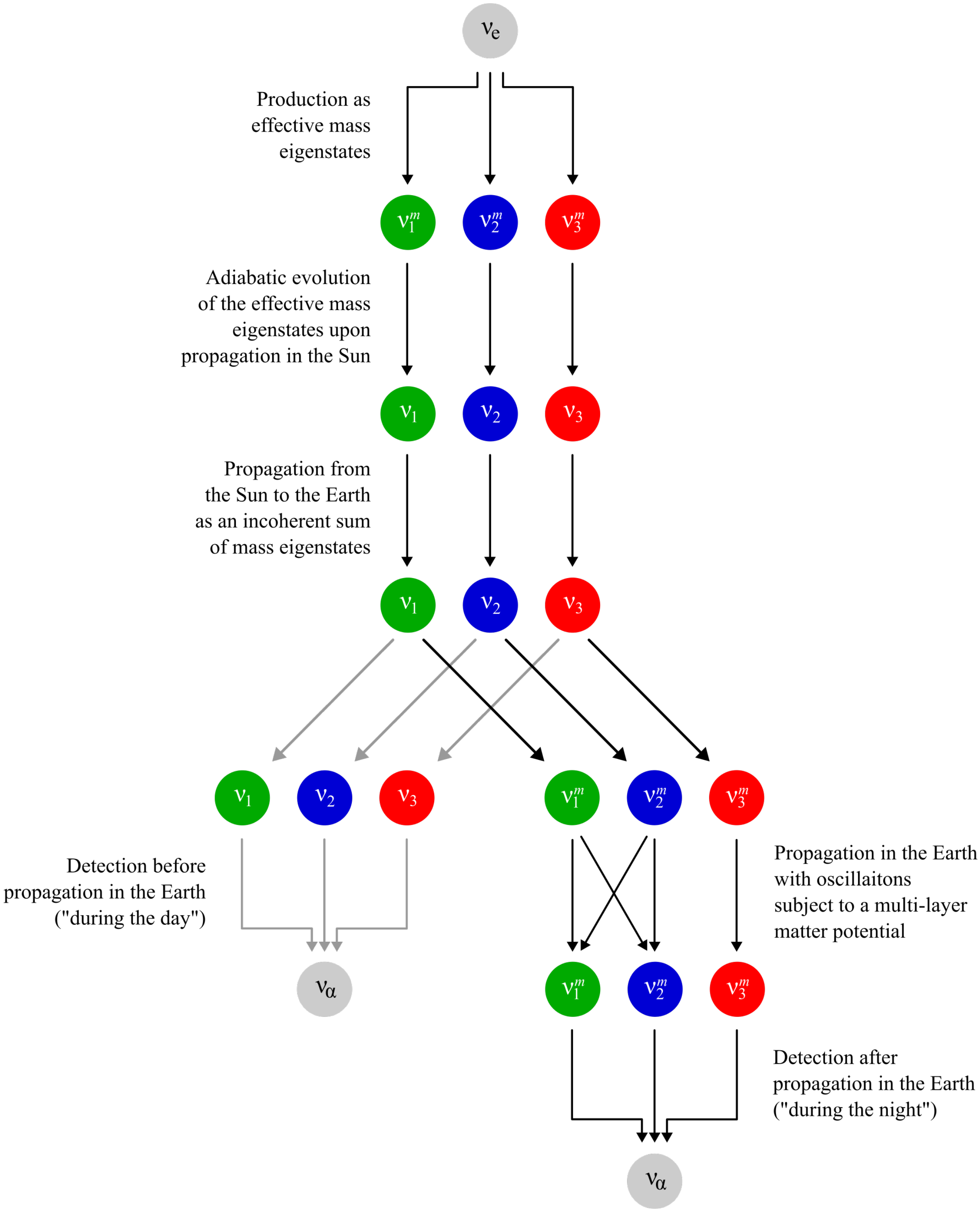

Figure 2.1: Schematic representation of the propagation of solar neutrinos from production to detection. Electron neutrinos are produced in the solar core from nuclear fusion reactions. They are produced in effective mass eigenstates governed by the matter potential at their point of production, and propagate outwards through the solar matter undergoing adiabatic transitions. Next, they propagate in interplanetary medium and are detected on Earth, either promptly "during the day" or after traversing a segment of the Earth's mantle and core "during the night" being subject to matter effects. Figure based on figures presented in Reference [58].

Now, a rotation in the basis can be made by multiplying both sides by $\mathbf{R}_{13}^{\dagger}\mathbf{R}_{23}^{\dagger}$ on the left, and using the relation $\mathbf{R}_{23}\mathbf{R}_{13}\mathbf{R}_{13}^{\dagger}\mathbf{R}_{23}^{\dagger} = \mathbf{I}$:

$$i\frac{d\nu'}{dt} = \frac{1}{2E}\left[\mathbf{R}_{12}\mathbf{M}\mathbf{R}_{12}^{\dagger} + \mathbf{R}_{13}^{\dagger}\mathbf{R}_{23}^{\dagger}\mathbf{V}\mathbf{R}_{23}\mathbf{R}_{13}\right]\nu', \tag{2.53}$$

where the primed states are defined as

$$\nu_e' = c_{13}\nu_e - s_{13}s_{23}\nu_\mu - s_{13}c_{23}\nu_\tau, \tag{2.54}$$

$$\nu_\mu' = c_{23}\nu_\mu - s_{23}\nu_\tau, \tag{2.55}$$

$$\nu_\tau' = s_{13}\nu_e - c_{13}s_{23}\nu_\mu - c_{13}c_{23}\nu_\tau, \tag{2.56}$$

and the evolution equations become

$$i\frac{d\nu'}{dt} = \frac{1}{2E}\begin{pmatrix} \Delta m_{21}^2 s_{12}^2 + 2EV_{\mathrm{CC}}c_{13}^2 & \Delta m_{21}^2 s_{12}c_{12} & 2EV_{CC}s_{13}c_{13} \\ \Delta m_{21}^2 s_{12}c_{12} & \Delta m_{21}^2 c_{12}^2 & 0 \\ 2EV_{\mathrm{CC}}s_{13}c_{13} & 0 & \Delta m_{31}^2 + 2EV_{\mathrm{CC}}s_{13}^2 \end{pmatrix}\nu'. \tag{2.57}$$

Now, for solar neutrino energies, it holds that $|\Delta m_{31}^2| >> 2EV_{\mathrm{CC}}s_{13}c_{13}$, for values of the matter potential V_{CC} both in the Sun and on Earth. In other words, matter effects on the evolution of the ν_τ' eigenstate can be neglected and the evolution of this third family in the primed basis is decoupled, as represented in Figure 2.1.

Thus, let $\mathbf{S}'$ be the time-dependent matrix describing the evolution of the primed states such that

$$\begin{pmatrix} \nu_e'(t) \\ \nu_\mu'(t) \\ \nu_\tau'(t) \end{pmatrix} = \begin{pmatrix} S_{ee}' & S_{e\mu}' & 0 \\ S_{\mu e}' & S_{\mu\mu}' & 0 \\ 0 & 0 & S_{\tau\tau}' \end{pmatrix}\begin{pmatrix} \nu_e'(0) \\ \nu_\mu'(0) \\ \nu_\tau'(0) \end{pmatrix}, \tag{2.58}$$

which we can transform back into the unprimed basis by another rotation:

$$\mathbf{S} = \mathbf{R}_{23}\mathbf{R}_{13}\begin{pmatrix} S_{ee}' & S_{e\mu}' & 0 \\ S_{\mu e}' & S_{\mu\mu}' & 0 \\ 0 & 0 & S_{\tau\tau}' \end{pmatrix}\mathbf{R}_{13}^{\dagger}\mathbf{R}_{23}^{\dagger}. \tag{2.59}$$

Then, the survival and transition probabilities for an electron neutrino is then given by

$$P_{ee} = |\langle\nu_e(t)|S|\nu_e(0)\rangle|^2 = |S_{ee}|^2, \tag{2.60}$$

$$P_{e\mu} + P_{e\tau} = |\langle\nu_\mu(t)|S|\nu_e(0)\rangle|^2 + |\langle\nu_\tau(t)|S|\nu_e(0)\rangle|^2 = |S_{e\mu}|^2 + |S_{e\tau}|^2. \tag{2.61}$$

From Equation (2.59):

$$S_{ee} = c_{13}^2 S'_{ee} + s_{13}^2 S'_{\tau\tau}\,, \tag{2.62}$$
$$S_{e\mu} = -s_{13}s_{23}c_{13}S'_{ee} + c_{13}c_{23}S'_{e\mu} + s_{13}s_{23}c_{13}S'_{\tau\tau}\,, \tag{2.63}$$
$$S_{e\tau} = -c_{13}c_{23}s_{13}S'_{ee} - c_{13}s_{23}S'_{e\mu} + c_{13}c_{23}s_{13}S'_{\tau\tau}\,, \tag{2.64}$$

and hence

$$P_{ee} = c_{13}^4 |S'_{ee}|^2 + c_{13}s_{13}(S'^{*}_{ee}S'_{\tau\tau} + S'_{ee}S'^{*}_{\tau\tau}) + s_{13}^4 |S'_{\tau\tau}|^2\,. \tag{2.65}$$

Since the evolution of the ν'_τ state is decoupled, $|S'_{\tau\tau}|^2 = 1$. Also, by the same reasoning from Equation (2.50), we neglect the interference effects in the second term of the equation above. Hence, the survival and transition probabilities become

$$P_{ee} = c_{13}^4 P'_{ee} + s_{13}^4\,, \tag{2.66}$$
$$P_{e(\mu+\tau)} = c_{13}^2 s_{13}^2 P'_{ee} + c_{13}^2 P'_{e\mu} + c_{13}^2 s_{13}^2\,. \tag{2.67}$$

On both, the primed probabilities are the probabilities for two neutrino families as shown on Equation (2.50). Finally, from Equations (2.66) and (2.67), the sum of probabilities over detected flavor is $\sum_\alpha P_{e\alpha} = 1$, and the probability is conserved.

2.3.2 Neutrino Oscillations in the Sun

Due to the adiabatic evolution of neutrino flavor eigenstates in the Sun, survival and transition probabilities depend only on the effective mixing angle at the point neutrino production and detection. The effective mixing angles are calculated from Equation (2.42). They are governed by the solar matter potential which depends on the electron number density at the point of production. The electron number density from the BS05(OP) [5] SSM is shown in Figure 2.2.

In two neutrino families, the probability of the produced ν_e be found as a ν_i at the surface of the Sun, $P_{ei}^{\odot}$, is given by $P_{ei}^{\odot} = |(U_M)_{ei}|^2$, where U_M is defined in Equation (2.41), and hence

$$P_{e1}^{\odot} = \cos^2\theta_M^{(0)} \quad \text{and} \quad P_{e2}^{\odot} = \sin^2\theta_M^{(0)}\,. \tag{2.68}$$

where $\theta_M^{(0)}$ is the effective mixing angle at the point neutrino production.

As seen in Figure 1.5, due to the temperature dependency of the reactions in each neutrino production channel, fractions of each solar neutrino flux are produced at different regions within the Sun. Hence, each fraction is subject to different matter potentials and are produced with different effective mixing angles. However, since the neutrino oscillation length is much smaller than both the production region and total propagation lengths, it is possible

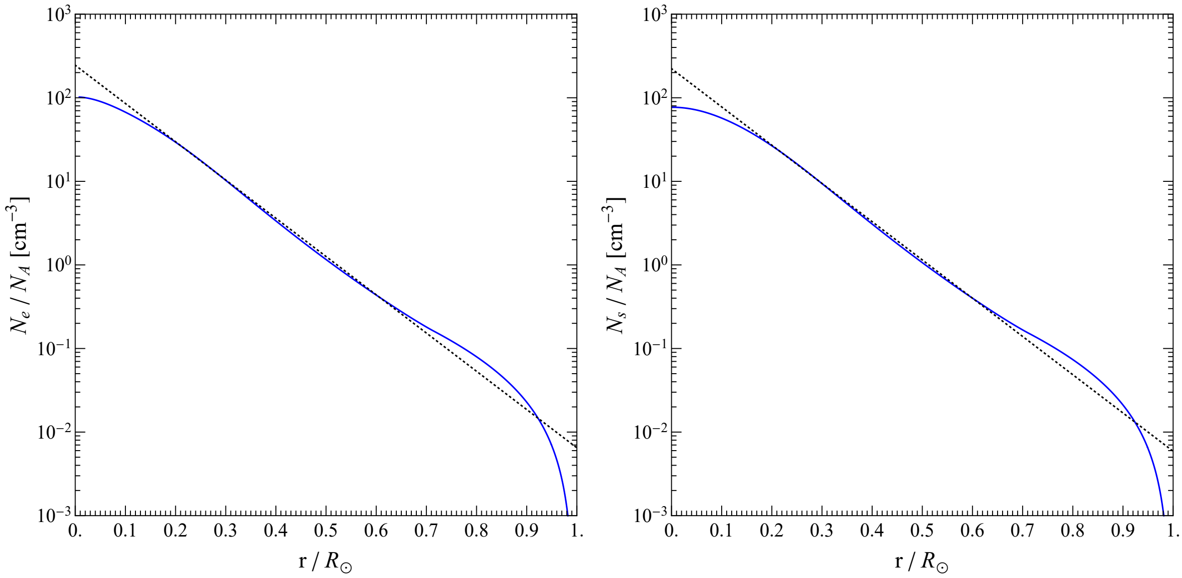

Figure 2.2: Electron (left) and sterile scatterer (right) number density from the BS05(OP) [5] SSM. Such number densities can be approximated by the exponential functions: $N_i(r) = N_i(0)\exp(-r/r_0)$ with $r_0 = R_\odot/10.54$, $N_e(0) = 245\,\mathrm{N_A/cm^3}$ and $N_s(0) = 223\,\mathrm{N_A/cm^3}$, where $R_\odot$ is the Solar radius. Tables for the number densities as functions of the solar radius can be found at the website http://www.sns.ias.edu/ jnb/

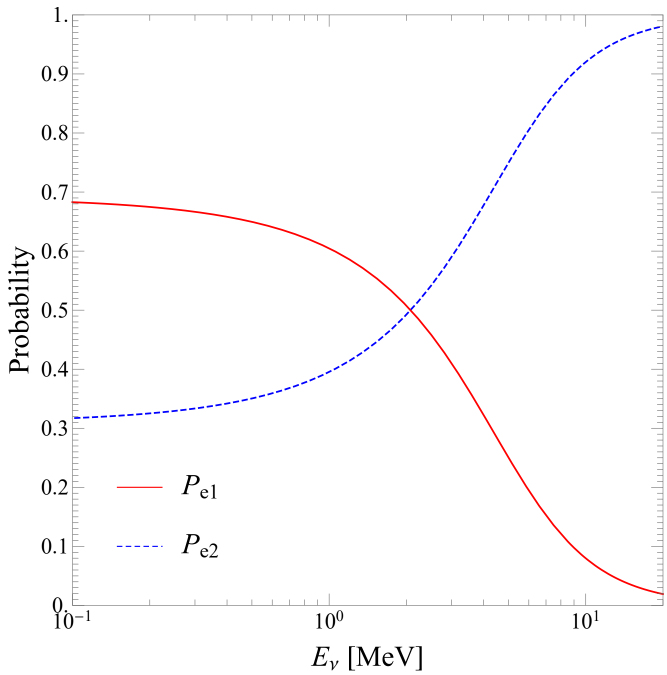

Figure 2.3: Probability for a ^{8}B ν_e produced in the solar core, subject to matter potential corresponding to the average potential in the production region, to be found in the solar surface as ν_1 and ν_2 as described by Equation (2.68). In the LMA-MSW solution, a 10 MeV ν_e will be produced almost as a pure ν_2 and, due to the adiabatic crossing of the resonance region, it will still reach the surface as ν_2. Best-fit values for the global fit neutrino oscillation parameters [59] as shown on Table 2.1 are used.

to average over the production region by assuming all neutrinos are produced subject to the average matter potential in the production region of each channel.

Figure 2.3 shows the probabilities $P^{\odot}_{e1}$ and $P^{\odot}_{e2}$ for ^{8}B neutrinos subject to potential corresponding to the average potential in the production region of this channel. As it can be seen, In the LMA-MSW solution, a 10 MeV ν_e will be produced almost as a pure ν_2 and, due to the adiabatic crossing of the resonance region, it will still reach the surface as ν_2.

2.3.3 Neutrino Regeneration on Earth

Solar neutrinos can be detected on Earth either promptly "during the day" or after traversing a segment of the Earth's mantle and core "during the night" being subject to matter effects.

During the day, arriving neutrinos cross a negligible amount of matter. Their propagation and detection on Earth can be approximated as happening in the vacuum. As such:

$$P^{\oplus}_{1e} = \cos^2\theta_{12} \quad \text{and} \quad P^{\oplus}_{2e} = \sin^2\theta_{12}\,. \tag{2.69}$$

During the night, however, arriving neutrinos may cross large slices of the Earth's matter and core. This may cause an asymmetry between the neutrino flux arriving during day and night. For two neutrino families, the day survival probability is given by

$$P^{\mathrm{D}}_{ee} = P^{\odot}_{e1}\, c^2_{12} + P^{\odot}_{e2}\, s^2_{12}\,, \tag{2.70}$$

and night survival probability is written as

$$P^{\mathrm{N}}_{ee} = P^{\odot}_{e1}\, P^{\oplus}_{1e} + P^{\odot}_{e2}\, P^{\oplus}_{2e}\,. \tag{2.71}$$

Since $P^{\odot}_{e1} + P^{\odot}_{e2} = 1$ and $P^{\oplus}_{1e} + P^{\oplus}_{2e} = 1$, the Equations (2.70) and (2.71) can be rewritten as

$$P^{\mathrm{D}}_{ee} = P^{\odot}_{e1}\left(c^2_{12} - s^2_{12}\right) + s^2_{12}\,, \tag{2.72}$$

and

$$P^{\mathrm{N}}_{ee} = P^{\oplus}_{2e} + \left(1 - 2\,P^{\oplus}_{2e}\right) P^{\odot}_{e1}\,. \tag{2.73}$$

Hence, by isolating $P^{\odot}_{e1}$ in Equation (2.72) and replacing in Equation (2.71):

$$\left(c^2_{12} - s^2_{12}\right) P^{\mathrm{N}}_{ee} = P^{\mathrm{D}}_{ee} - s^2_{12} + P^{\oplus}_{2e}\left(1 - 2\,P^{\mathrm{D}}_{ee}\right)\,, \tag{2.74}$$

and the transition probability is given by $P_{e\mu} \;=\; 1 - P_{ee}$.

Now, for three neutrino families, the survival probabilities are given by

$$P^{\mathrm{D}}_{ee} = s^4_{13} + \left(P^{\odot}_{e1}\, c^2_{12} + P^{\odot}_{e2}\, s^2_{12}\right) c^4_{13}\,, \tag{2.75}$$

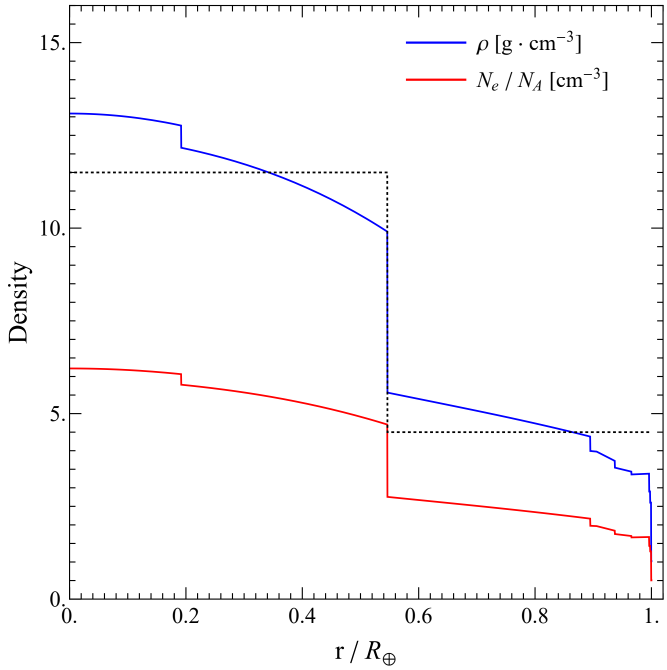

Figure 2.4: Earth's density (upper solid line) and electron number density (lower solid line) profiles as a function of radius r. Earth's density profile ρ is given in Reference [60]. Electron number density [7] is given as $N_e = N_A(\rho/g)\langle Z/A\rangle$ with $\langle Z/A\rangle = 0.475\,(0.495)$ in the core (mantle) for $r \leq (>)$ 3480 km. The dotted line is a step approximation to the density profile with $\rho = 11.5\,(4.5)\,\mathrm{g\cdot cm^{-3}}$ in the core (mantle).

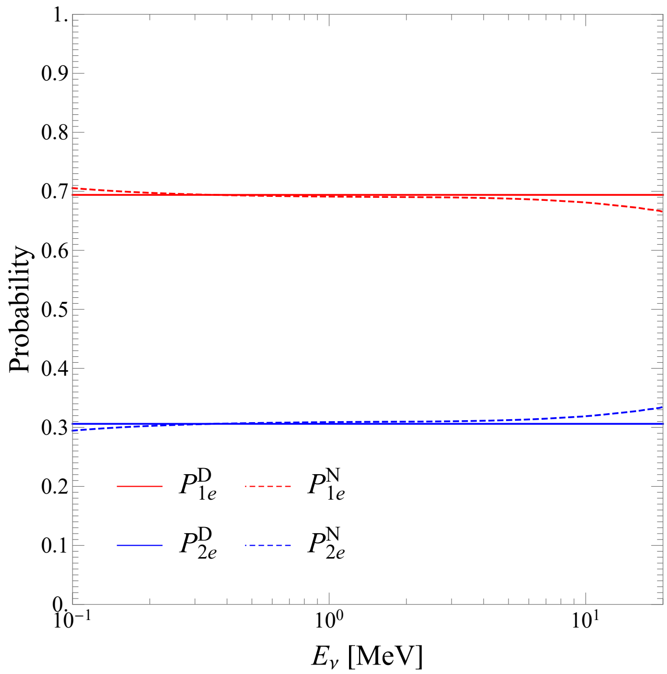

Figure 2.5: Day and Night (SNO latitude) probabilities for ν_1 and ν_2 to be detected on Earth as a ν_e. Solar neutrinos will cross either only Earth's atmosphere (during the day) or Earth's interior (during the night). Thus, due to Earth's matter potential, there may be a day-night asymmetry in the solar neutrino fluxes. Best-fit values for the global fit neutrino oscillation parameters [59] as shown on Table 2.1 are used.

and

$$P_{ee}^{\mathrm{N}} = s_{13}^4 + \left(P_{e1}^{\odot} P_{1e}^{\oplus} + P_{e2}^{\odot} P_{2e}^{\oplus}\right) c_{13}^4 \,. \tag{2.76}$$

By writing $P'_{ee} \;=\; \left(P_{ee} - s_{13}^4\right)/c_{13}^4$ and using Equation (2.74):

$$\left(c_{12}^2 - s_{12}^2\right) P_{ee}^{\mathrm{N}} = P_{ee}^{\mathrm{D}} - s_{12}^2 P' + P_{2e}^{\oplus}\left(P' - 2P_{ee}^{\mathrm{D}}\right) , \tag{2.77}$$

where $P' = c_{13}^4 + 2s_{13}^4$, and the transition probability is given by $P_{e(\mu+\tau)} \;=\; 1 - P_{ee}$.

From Equations (2.74) and (2.77), it can be seen that the net effect of Earth's matter potential will depend on the values of the day probability and θ_{12} mixing angle. If the day probability is small and $\cos^2\theta < \sin^2\theta$, the night probability is greater than the day probability, that is, there is a regeneration of the electron neutrino flux, as shown in Figure 2.4.

2.4 Neutrino Oscillation Parameters

Over the years, results from solar neutrino experiments eventually established the Neutrino Flavor Oscillation model with Large Mixing Angle and Mikheyev-Smirnov-Wolfenstein Resonant Flavor Conversion (LMA-MSW) as the best solution to the SNP. In combination with the measurement of the other oscillation parameters by experiments designed for atmospheric [61], reactor [62] and long-baseline [63] neutrinos established the scenario of three massive light neutrinos that mix [64]. A global fit to neutrino oscillation parameters [59] is shown on Table 2.1.

Table 2.1: Three-flavor oscillation parameters from Reference [59] fit to global data, including SK atmospheric data. In the Normal Hierarchy $\Delta m_{3l}^2 \;=\; \Delta m_{31}^2 \;>\; 0$ and in the Inverted Hierarchy $\Delta m_{3l}^2 \;=\; \Delta m_{32}^2 \;<\; 0$.

Parameter	Normal Hierarchy		Inverted Hierarchy	
	Best-fit $\pm 1\sigma$	3σ Range	Best-fit $\pm 1\sigma$	3σ Range
$\sin^2\theta_{12}$	$0.310^{+0.013}_{-0.012}$	$0.275 \to 0.350$	$0.310^{+0.013}_{-0.012}$	$0.275 \to 0.350$
$\sin^2\theta_{23}$	$0.563^{+0.018}_{-0.024}$	$0.433 \to 0.609$	$0.565^{+0.017}_{-0.022}$	$0.436 \to 0.610$
$\sin^2\theta_{13}$	$0.02237^{+0.00066}_{-0.00065}$	$0.02044 \to 0.02435$	$0.02259^{+0.00065}_{-0.00065}$	$0.02064 \to 0.02457$
$\delta_{\mathrm{CP}}/^\circ$	221^{+39}_{-28}	$144 \to 357$	282^{+23}_{-25}	$205 \to 348$
$\frac{\Delta m_{21}^2}{10^{-5}\,\mathrm{eV}^2}$	$7.39^{+0.21}_{-0.20}$	$6.79 \to 8.01$	$7.39^{+0.21}_{-0.20}$	$6.79 \to 8.01$
$\frac{\Delta m_{3l}^2}{10^{-3}\,\mathrm{eV}^2}$	$+2.528^{+0.029}_{-0.031}$	$+2.436 \to +2.618$	$-2.510^{+0.030}_{-0.031}$	$-2.601 \to -2.419$

As seen in Section 2.2.1, neutrino oscillations are sensitive only to the squared-mass differences, and not to the mass eigenstates' absolute masses [7]. Oscillation experiments show that neutrino oscillations are governed by at least two independent mass-squared differences denoted $\Delta m^2_{\rm sol}$ and $\Delta m^2_{\rm atm}$, respectively defining the dominant oscillation lengths for solar and atmospheric neutrinos, with $\Delta m^2_{\rm sol} << \Delta m^2_{\rm atm}$. Additionally, matter effects in the Sun implies that $\Delta m^2_{\rm sol} > 0$ while the sign of $\Delta m^2_{\rm atm}$ is currently unknown. $\Delta m^2_{\rm atm}$ is measured from neutrino oscillations in vacuum which is sensitive only to the absolute value of the mass-squared difference. In the context of three-neutrino families, there are two independent mass-squared differences, since:

$$\Delta m^2_{32} + \Delta m^2_{21} = \Delta m^2_{31}\,. \tag{2.78}$$

As such, there are two possible solutions for the absolute scale of neutrino masses.

In the so-called "normal" ordering or hierarchy (NH), the smallest mass-squared difference measured by neutrino experiments is chosen to correspond to the mass-squared difference between the two lightest mass eigenstates — arbitrarily labeled ν_1 and ν_2, whereas the heaviest mass eigenstate is labeled ν_3 — and as such [65]:

$$\Delta m^2_{21} \ll \left(\Delta m^2_{31} \approx \Delta m^2_{32} > 0\right)\,. \tag{2.79}$$

On the other hand, in the "inverted" ordering or hierarchy (IH), the smallest mass-squared difference measured by neutrino experiments is chosen to correspond to the mass-squared difference between the two heaviest mass eigenstates — labeled ν_2 and ν_1, whereas the

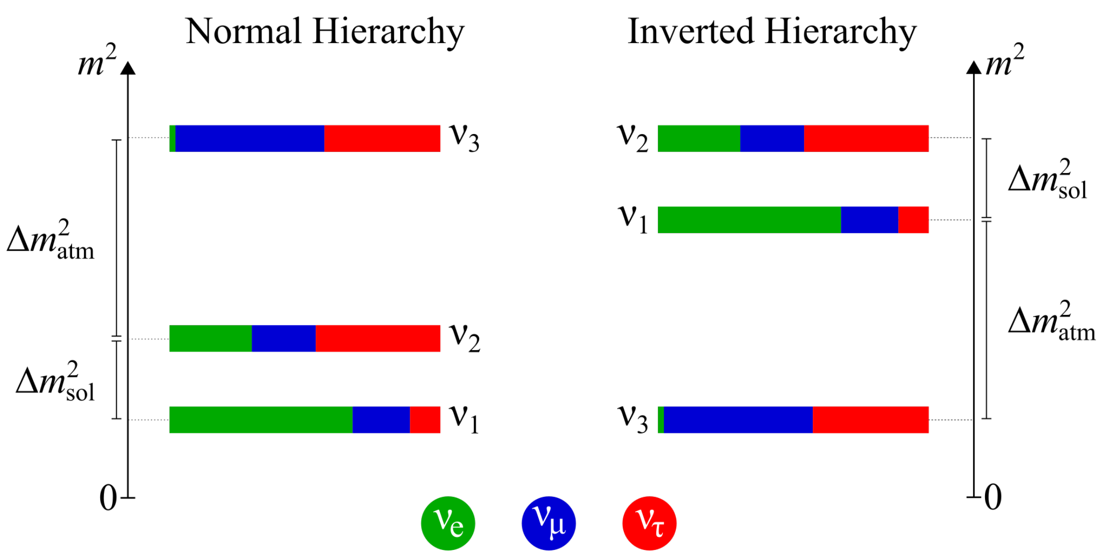

Figure 2.6: Schematic representation of both neutrino mass orderings allowed by the mass-squared differences $\Delta m^2_{\rm sol}$ and $\Delta m^2_{\rm atm}$. The size of colored bars represent the probability of finding a ν_α neutrino in the mass eigenstate ν_i. Best-fit values for the global fit neutrino oscillation parameters [59] as shown on Table 2.1 are used.

lightest mass eigenstate is labeled ν_3 — which implies [65]:

$$\Delta m^2_{21} \ll -\left(\Delta m^2_{32} \approx \Delta m^2_{31} < 0\right) . \tag{2.80}$$

Figure 2.6 shows a schematic representation of both neutrino mass orderings allowed by the mass-squared differences Δm^2_{sol} and Δm^2_{atm}. In Figure 2.6, the size of colored bars represent the probability of finding a ν_α neutrino in the mass eigenstate ν_i. Best-fit values for the global fit neutrino oscillation parameters [59] as shown on Table 2.1 are used.

Chapter 3

Neutrino Decay

Besides neutrino flavour oscillations, presented in Chapter 2, many other models were proposed over the years as solutions to the Solar Neutrino Problem: (i) active neutrino states could be mixed with sterile neutrino states, with parameter values as to reduce the flux of electron neutrinos produced in the Sun [66]; (ii) particles not directly linked to the neutrinos could change their production in the Sun by modifying the thermal transport in the solar core [67]; (iii) neutrinos could be subject to flavour non-diagonal interactions with matter such as $\nu_\alpha + N \to \nu_\beta + X$, which would modify the detected neutrino flux [68]; (iv) if neutrinos are massive, they are allowed to decay modifying the solar neutrino fluxes between production and detection [69]; massive neutrinos might have a magnetic dipole moment through which they interact with magnetic fields in the Sun and change into other helicities and flavours [70]; among others.

The neutrino oscillation phenomenon currently establishes the massive nature of neutrinos beyond reasonable doubt. As such, it is possible for neutrinos to decay into other particles. Hence, neutrino decay has been studied in a variety of circumstances, including: nucleonsynthesis in the early universe and the formation of structures [71, 72], high energy astrophysical phenomena such as Gamma Ray Bursts and Active Galactic Nuclei [73–78], Supernova explosions [79–85], and in the Sun [86–100].

In the latter case, although ruled out as a leading process in the SNP, it is still possible to investigate neutrino decay as sub-leading effects in the propagation of solar neutrinos to extract new limits to neutrino lifetime using the most recent experimental data.

3.1 Neutrino Decay Model

If neutrinos are massive, and the masses are non-degenerate, it is possible for a heavier neutrino to decay into a lighter neutrino with the emission of a photon, $\nu \to \nu' + \gamma$, in what is called a *radiative neutrino decay* (see Reference [101] and references therein). Such decays are constrained using the cosmic microwave background spectral data and lower bounds to the lifetime are obtained [102] as $\tau > 10^{19}\,\mathrm{s}$, which is too constrained to be of interest here.

On the other hand, *non-radiative neutrino decays* [86], i.e., $\nu \to \nu' + X$, which arise from new, non-standard physics, can also be studied. Such decays can be separated into two types: visible and invisible. Invisible decays [80, 82, 85, 92, 103–106] are those in which the products are invisible states, that is, states that either are in principle not detectable or will not be detected by the experiment in question such as the decay into sterile neutrinos plus scalar particles. On the other hand, visible decays [83, 84, 107–111] are those in which the products are visible states, that is, at least one of the daughter particles is in principle detectable, e.g., the decay of a mass eigenstate into at least one lighter active mass-eigenstate.

From the analysis of different neutrino experimental data, its is possible to extract bounds to the lifetime of each neutrino species in a variety of phenomena. For example, from the detection of neutrinos from Supernova 1987A, a bound to ν_1 lifetime can be set [79] at $\tau_1/m_1 \geq 10^5\,\mathrm{s\cdot eV^{-1}}$.

From solar neutrino data, the current bound to ν_2 lifetime for invisible decays was obtained by the SNO collaboration [112] in an analysis including all three phases of ^{8}B solar neutrino data, combined with data from other solar neutrino experiments, resulting in $\tau_2\,/\,m_2 \geq 1.02\times10^{-3}\,\mathrm{s\cdot eV^{-1}}$, at 99% C.L.. On the other hand, in the context of visible decays [103] of solar neutrinos, the bound to ν_2 lifetime was $\tau_2/m_2 \geq 1.1\times10^{-3}\,(6.7\times10^{-2})\,\mathrm{s\cdot eV^{-1}}$ at 90% C.L. corresponding to the hierarchical (quasi-degenerate) scenario for neutrino masses.

Limits to neutrino lifetime can also be investigated for high energy neutrinos [113, 114]. For example, the first detection of a Glashow resonance candidate in IceCube, originated from high-energy cosmic neutrinos, was used [114] to place new lower limits on the lifetimes $\tau_1/m_1 \geq 2.91\times10^{-3}\,\mathrm{s\cdot eV^{-1}}$ and $\tau_2/m_2 \geq 1.26\times10^{-3}\,\mathrm{s\cdot eV^{-1}}$ at 90% C.L..

The lifetime of the ν_3 eigenstate in the context of invisible decays, from the combined accelerator and atmospheric neutrino data, is $\tau_3/m_3 \geq 2.9\times10^{-10}\,\mathrm{s\cdot eV^{-1}}$ at 90% C.L. [111]. Similarly, an analysis of the long-baseline experiments MINOS and T2K gives a combined limit of $\tau_3/m_3 \geq 2.8\times10^{-12}\,\mathrm{s\cdot eV^{-1}}$ at 90% C.L. [115]. For visible decays, from the analysis of data from the reactor experiments KamLAND and JUNO (simulated) [116], the limit was obtained at $\tau_3/m_3 \geq 1.0\times10^{-10}\,\mathrm{s\cdot eV^{-1}}$ at 90% C.L. for the normal hierarchy.

Albeit necessary for decay, there is still no consensus regarding the mechanism for generating neutrino masses. One of the possibilities is that neutrino mass arise from a new coupling to a scalar singlet know as Majoron [117–119]. As a consequence, the coupling makes it possible for a neutrino to decay into a lighter neutrino alongside the emission of a Majoron — $\nu_i \to \nu_j + X$. Hence, for an interaction Lagrangian with Yukawa scalar and pseudoscalar couplings, this process is described by [120]

$$\mathscr{L}_{\mathrm{int}} = \sum_{\substack{i \\ i\neq j}}\sum_{j}(g_s)_{ij}\bar{\nu}_j\nu_i X + i(g_p)_{ij}\bar{\nu}_j\gamma_5\nu_i X + \mathrm{h.c.}\,, \tag{3.1}$$

where $i, j = 1,2,3$ are respectively mother and daughter mass eigenstates, while $(g_s)_{ij}$ and $(g_p)_{ij}$ are respectively the scalar and pseudo-scalar coupling constants. The decay width Γ will be given by

$$d\Gamma = \frac{1}{2E_i} |\mathscr{M}|^2 (2\pi)^4 \delta^{(4)}(\mathbf{p}_i - \mathbf{p}_j - \mathbf{p}_X) \frac{d^3 p_j}{(2\pi)^3} \frac{1}{E_j} \frac{d^3 p_X}{(2\pi)^3} \frac{1}{E_X} , \tag{3.2}$$

where $\mathbf{p}_i = (E_i, \vec{p}_i)$, $\mathbf{p}_j = (E_j, \vec{p}_j)$, $\mathbf{p}_X = (E_X, \vec{p}_X)$ are respectively ν_i, ν_j and X four-momenta, with $E_i^2 = |\vec{p}_i|^2 + m_i^2$, $E_j^2 = |\vec{p}_j|^2 + m_j^2$ and $E_X^2 = |\vec{p}_X|^2 + m_X^2$. In the neutrino decay analysis present in this thesis, we suppose a *massless* Majoron, that is, $m_X = 0$.

The amplitudes $\mathscr{M}$ for each decay process are obtained from the adequate Feynman diagrams and are given in the Laboratory frame by

$$\left|\mathscr{M}\left(\nu_i^r \to \nu_j^r\right)\right|^2 = \frac{(g_s)_{ij}^2}{4}(A+2) + \frac{(g_p)_{ij}^2}{4}(A-2) , \tag{3.3}$$

$$\left|\mathscr{M}\left(\nu_i^r \to \nu_j^{r'}\right)\right|^2 = \frac{(g_s)_{ij}^2 + (g_p)_{ij}^2}{4}\left(\frac{1}{x_{ij}} + x_{ij} - A\right) , \tag{3.4}$$

where r, r' denote helicity states.

In this work, neutrinos are assumed to be Majorana particles, that is, neutrinos and antineutrinos are identical and can only be distinguished by their, respectively, left and right-handed helicities. Weak interactions couple to chiral left-handed neutrinos and chiral right-handed antineutrinos, which, for relativistic neutrinos are approximated as equal to left and right helicity states up to terms of order m/E. Hence, both left-handed and right-handed Majorana neutrinos are detectable.

On the other hand, in the case neutrinos and antineutrinos are Dirac particles, the decay products of the respective helicity-flipping channels do not participate in weak interactions and, consequently, are not observable.

Hence, $\mathscr{M}(\nu_i^r \to \nu_j^r)$ describes helicity-conserving decays, such as $\nu_i \to \nu_j + X$, while $\mathscr{M}(\nu_i^r \to \nu_j^{r'})$ describes helicity-violating decays, such as $\nu_i \to \bar{\nu}_j + X$. In the expressions below, we write $\mathscr{M}(\nu_i^r \to \nu_j^s) = \mathscr{M}_{ij}^{rs}$, where s can denote either of the helicity states. Additionally

$$A = \frac{1}{x_{ij}} \frac{E_i}{E_j} + x_{ij} \frac{E_j}{E_i} , \quad \text{with } x_{ij} = \frac{m_i}{m_j} > 1 . \tag{3.5}$$

Hence, the differential decay width is given by

$$\frac{d\Gamma_{ij}^{rs}}{dE_j} = \frac{m_i m_j}{4\pi E_i^2}\left(1 - \frac{m_i^2}{E_i^2}\right) |\mathscr{M}_{ij}^{rs}|^2 , \tag{3.6}$$

with the kinematics condition

$$E_i - E_j = |\vec{p}_i - \vec{p}_j| = \left(|\vec{p}_i|^2 + |\vec{p}_j|^2 - 2|\vec{p}_i||\vec{p}_j|\cos\theta\right)^{1/2} , \tag{3.7}$$

which leads to the condition on the angle between in and out states

$$\cos\theta = \frac{2E_iE_j - (m_i^2 + m_f^2)}{2|\vec{p}_i||\vec{p}_j|} = \frac{2E_iE_j - (m_i^2 + m_j^2)}{2\left(E_i^2 - m_i^2\right)^{1/2}\left(E_j^2 - m_j^2\right)^{1/2}}, \tag{3.8}$$

which implies the bound to the energy of the outgoing particle

$$\frac{E_i}{2}\left(1+\frac{1}{x_{ij}^2}\right) - \frac{|\vec{p}_i|}{2}\left(1-\frac{1}{x_{ij}^2}\right) \le E_j \le \frac{E_i}{2}\left(1+\frac{1}{x_{ij}^2}\right) + \frac{|\vec{p}_i|}{2}\left(1-\frac{1}{x_{ij}^2}\right). \tag{3.9}$$

For ultra-relativistic neutrinos, the bounds become

$$\frac{E_i}{x^2} \le E_j \le E_i\,, \tag{3.10}$$

and the differential decay width reduces to

$$\frac{d\Gamma_{ij}^{rs}}{dE_j} = \frac{m_im_j}{4\pi E_i^2}\left|\mathscr{M}_{ij}^{rs}\right|^2, \tag{3.11}$$

which yield the partial decay widths

$$\begin{aligned}\Gamma_{ij}^{rr} &= \frac{m_im_j}{16\pi E_i}\left[(g_s)_{ij}^2\left(\frac{x_{ij}}{2} + 2 + \frac{2}{x_{ij}}\ln x_{ij} - \frac{2}{x_{ij}^2} - \frac{1}{2x_{ij}^3}\right) + \right.\\ &\left. + (g_p)_{ij}^2\left(\frac{x_{ij}}{2} - 2 + \frac{2}{x_{ij}}\ln x_{ij} + \frac{2}{x_{ij}^2} - \frac{1}{2x_{ij}^3}\right)\right], \qquad (3.12)\\ \Gamma_{ij}^{rr'} &= \frac{m_im_j}{16\pi E_i}\left[(g_s)_{ij}^2 + (g_p)_{ij}^2\right]\left(\frac{x_{ij}}{2} - \frac{2}{x_{ij}}\ln x_{ij} - \frac{1}{2x_{ij}^3}\right). \qquad (3.13)\end{aligned}$$

Now, for notation convenience, we write the decay widths as functions of $g_{ij}^2 = (g_s)_{ij}^2 + (g_p)_{ij}^2$ and $h_{ij}^2 = (g_s)_{ij}^2 - (g_p)_{ij}^2$. The differential decay widths are rewritten as

$$\begin{aligned}\frac{d\Gamma_{ij}^{rr}}{dE_j} &= \frac{m_im_j}{16\pi E_i^2}\left[g_{ij}^2\left(\frac{1}{x_{ij}}\frac{E_i}{E_j} + x_{ij}\frac{E_j}{E_i}\right) + 2h_{ij}^2\right], \qquad (3.14)\\ \frac{d\Gamma_{ij}^{rr'}}{dE_j} &= \frac{m_im_j}{16\pi E_i^2}g_{ij}^2\left[\frac{1}{x_{ij}} + x_{ij} - \left(\frac{1}{x_{ij}}\frac{E_i}{E_j} + x_{ij}\frac{E_j}{E_i}\right)\right]. \qquad (3.15)\end{aligned}$$

Additionally, since $m_im_j = m_i^2(x_{ij})^{-1}$, we also write for convenience $\delta_{ij} = (x_{ij})^{-1}$ and the expressions further simplify to

$$\frac{d\Gamma_{ij}^{rr}}{dE_j} = \frac{m_i^2}{16\pi E_i^2}\left[g_{ij}^2\left(\frac{E_j}{E_i} + \delta_{ij}^2\frac{E_i}{E_j}\right) + 2\delta_{ij}h_{ij}^2\right], \tag{3.16}$$

$$\frac{d\Gamma_{ij}^{rr'}}{dE_j} = \frac{m_i^2}{16\pi E_i^2}\; g_{ij}^2\left[1 - \frac{E_j}{E_i} + \delta_{ij}^2\left(1 - \frac{E_i}{E_j}\right)\right], \tag{3.17}$$

and similarly, the partial decay widths become

$$\Gamma_{ij}^{rr} = \frac{m_i^2}{32\pi E_i}\left[g_{ij}^2\left(1 - 4\delta_{ij}^2\ln\delta_{ij} - \delta_{ij}^4\right) + 4h_{ij}^2\delta_{ij}\left(1 - \delta_{ij}^2\right)\right], \tag{3.18}$$

$$\Gamma_{ij}^{rr'} = \frac{m_i^2}{32\pi E_i}\left[g_{ij}^2\left(1 + 4\delta_{ij}^2\ln\delta_{ij} - \delta_{ij}^4\right)\right]. \tag{3.19}$$

Finally, the total decay width Γ_i^r for an mass eigenstate i of helicity r is related to its decay rate α_i^r and its rest-frame lifetime τ_i by

$$\frac{m_i}{\tau_i} = \alpha_i^r = \sum_{k,s}\alpha_{ik}^{rs} = E_i\sum_{k,s}\Gamma_{ik}^{rs} = E_i\Gamma_i^r. \tag{3.20}$$

In the following sections, we shall only consider the decay of a single heavier mass eigenstate ν_i into neutrinos and antineutrinos of a lighter mass eigenstate, ν_j and $\bar{\nu}_j$. Hence, the notation in Equations (3.16) and (3.17) above can be simplified to

$$\frac{d\Gamma_{ij}^{rr}}{dE_j} = \frac{m_i^2}{16\pi E_i^2}\left[g^2\left(\frac{E_j}{E_i} + \delta^2\frac{E_i}{E_j}\right) + 2\delta h^2\right], \tag{3.21}$$

$$\frac{d\Gamma_{ij}^{rr'}}{dE_j} = \frac{m_i^2}{16\pi E_i^2}\; g^2\left[1 - \frac{E_j}{E_i} + \delta^2\left(1 - \frac{E_i}{E_j}\right)\right], \tag{3.22}$$

and from Equations (3.18) and (3.19)

$$\Gamma_{ij}^{rr} = \frac{m_i^2}{32\pi E_i}\left[g^2\left(1 - 4\delta^2\ln\delta - \delta^4\right) + 4h^2\delta\left(1 - \delta^2\right)\right], \tag{3.23}$$

$$\Gamma_{ij}^{rr'} = \frac{m_i^2}{32\pi E_i}\left[g^2\left(1 + 4\delta^2\ln\delta - \delta^4\right)\right]. \tag{3.24}$$

Finally, from Equation (3.20), the total decay width is written as $\Gamma_i^r = \Gamma_{ij}^{rr} + \Gamma_{ij}^{rr'}$. As such

$$\Gamma_i^r = \frac{m_i^2}{16\pi E_i}\left[g^2\left(1 - \delta^4\right) + 2h^2\delta\left(1 - \delta^2\right)\right]. \tag{3.25}$$

Now, notice that in general the decay widths, and consequently the decay rates, depend on the interaction coupling constants and neutrino masses, which are unknown parameters. Hence, it would be useful to reduce the number of such unknown parameters [121]. From Equations (3.20) and (3.25), it is possible to write

$$\alpha_i^r = \frac{m_i^2}{16\pi}\left(1-\delta^2\right)\left[(1+\delta)^2 g_s^2 + (1-\delta)^2 g_p^2\right]. \tag{3.26}$$

Solving Equation (3.26) for each coupling constants and substituting one at a time in Equations (3.21) and (3.22), the differential decay widths become

$$\frac{d\Gamma_{ij}^{rr}}{dE_j} = \frac{\alpha_i^r}{E_i^2} f_1 - \frac{\alpha_i^r}{E_i^2} f_2 \left(f_1 \mp \frac{m_i^2 g_{s(p)}^2}{8\pi\alpha_i^r} f_3\right)\left(1+\delta^2 - \frac{E_j}{E_i} - \delta^2 \frac{E_i}{E_j}\right), \tag{3.27}$$

$$\frac{d\Gamma_{ij}^{rr'}}{dE_j} = \frac{\alpha_i^r}{E_i^2} f_2 \left(f_1 \mp \frac{m_i^2 g_{s(p)}^2}{8\pi\alpha_i^r} f_3\right)\left(1+\delta^2 - \frac{E_j}{E_i} - \delta^2 \frac{E_i}{E_j}\right), \tag{3.28}$$

with $f_{1,s(p)} = \dfrac{1}{(1-\delta^2)}$, $f_{2,s(p)} = \dfrac{1}{(1\mp\delta)^2}$ and $f_{3,s(p)} = 2\delta$, and where the upper (lower) sign corresponds to g_s (g_p). As such, since $\delta = m_j/m_i = \sqrt{1-\Delta m_{ij}^2/m_i^2}$, by fixing the value of one coupling constant, the differential decay widths are completely determined by the decay rate α_i and the neutrino mass m_i.

Finally, we can divide the differential decay widths above by the total decay width Γ_i^r, which, from Equation (3.20), is also written $\Gamma_i^r = \alpha_i^r/E_i$. Hence, we obtain a weighted differential decay width

$$w_{ij}^{rr} = \frac{1}{\Gamma_i^r}\frac{d\Gamma_{ij}^{rr}}{dE_j} = \frac{f_1}{E_i} - \frac{f_2}{E_i}\left(f_1 \mp \frac{m_i^2 g_{s(p)}^2}{8\pi\alpha_i} f_3\right)\left(1+\delta^2 - \frac{E_j}{E_i} - \delta^2 \frac{E_i}{E_j}\right), \tag{3.29}$$

$$w_{ij}^{rr'} = \frac{1}{\Gamma_i^r}\frac{d\Gamma_{ij}^{rr'}}{dE_j} = \frac{f_2}{E_i}\left(f_1 \mp \frac{m_i^2 g_{s(p)}^2}{8\pi\alpha_i} f_3\right)\left(1+\delta^2 - \frac{E_j}{E_i} - \delta^2 \frac{E_i}{E_j}\right), \tag{3.30}$$

which appears in the discussion in the next sections.

Now, we explicitly present three cases for the weighted differential decay widths originating from:

- a scalar interaction ($g_p = 0$),
- a pseudo-scalar interaction ($g_s = 0$), and
- an interaction with $g_s^2 = g_p^2$, which we call a democratic interaction.

First, for the scalar interaction, Equations (3.29) and (3.30) become

$$w_{ij}^{rr} = \frac{1}{(1-\delta^2)}\frac{1}{E_i} - \frac{1}{(1-\delta^2)(1+\delta)^2}\frac{1}{E_i}\left(1+\delta^2 - \frac{E_j}{E_i} - \delta^2 \frac{E_i}{E_j}\right), \tag{3.31}$$

$$w_{ij}^{rr'} = \frac{1}{(1-\delta^2)(1+\delta)^2}\frac{1}{E_i}\left(1+\delta^2 - \frac{E_j}{E_i} - \delta^2 \frac{E_i}{E_j}\right). \tag{3.32}$$

Next, for the pseudo-scalar interaction, Equations (3.29) and (3.30) become

$$w_{ij}^{rr} = \frac{1}{(1-\delta^2)}\frac{1}{E_i} - \frac{1}{(1-\delta^2)\,(1-\delta)^2}\frac{1}{E_i}\left(1+\delta^2-\frac{E_j}{E_i}-\delta^2\frac{E_i}{E_j}\right), \tag{3.33}$$

$$w_{ij}^{rr'} = \frac{1}{(1-\delta^2)\,(1-\delta)^2}\frac{1}{E_i}\left(1+\delta^2-\frac{E_j}{E_i}-\delta^2\frac{E_i}{E_j}\right). \tag{3.34}$$

Finally, for the democratic interaction, from Equation (3.26):

$$\alpha_i^r = \frac{m_i^2}{8\pi}\left(1-\delta^4\right)g_s^2 = \frac{m_i^2}{8\pi}\left(1-\delta^4\right)g_p^2, \tag{3.35}$$

for which the weighted differential decay rates given in Equations (3.29) and (3.30) become

$$w_{ij}^{rr} = \frac{1}{(1-\delta^2)}\frac{1}{E_i} - \frac{1}{(1-\delta^4)}\frac{1}{E_i}\left(1+\delta^2-\frac{E_j}{E_i}-\delta^2\frac{E_i}{E_j}\right), \tag{3.36}$$

$$w_{ij}^{rr'} = \frac{1}{(1-\delta^4)}\frac{1}{E_i}\left(1+\delta^2-\frac{E_j}{E_i}-\delta^2\frac{E_i}{E_j}\right). \tag{3.37}$$

From Equations (3.31) – (3.37), for some combinations of E_i, E_j and δ, w_{ij}^{rs} may be null. For the chirality changing decay, for all three cases defined above, $w_{ij}^{rr'} = 0$ for $E_i = E_j$ and $E_i = E_j/\delta^2$ which corresponds to the integration limits on Equation (3.10). On the other hand, the chirality conserving $w_{ij}^{rr} = 0$ is null only for the pseudo-scalar decay with $E_i = E_j/\delta$. These behaviors are shown in Figure 3.1 for $\delta = 0.05$ and $\delta = 0.95$.

Notice that, by integrating the equations above within the limits defined in Equation (3.10), one obtains the branching fraction Br_{ij}^{rs} for each decay channel, shown in Figure 3.2. First, for the scalar interaction:

$$\mathrm{Br}_{ij}^{rr} = \frac{1+\delta^2}{2(1+\delta)^2} - \frac{2\delta^2\ln\delta}{(1+\delta)^2(1-\delta^2)} + \frac{2\delta}{(1+\delta)^2}, \tag{3.38}$$

$$\mathrm{Br}_{ij}^{rr'} = \frac{1+\delta^2}{2(1+\delta)^2} + \frac{2\delta^2\ln\delta}{(1+\delta)^2(1-\delta^2)}. \tag{3.39}$$

Next, for the pseudo-scalar interaction:

$$\mathrm{Br}_{ij}^{rr} = \frac{1+\delta^2}{2(1-\delta)^2} - \frac{2\delta^2\ln\delta}{(1-\delta)^2(1-\delta^2)} + \frac{2\delta}{(1-\delta)^2}, \tag{3.40}$$

$$\mathrm{Br}_{ij}^{rr'} = \frac{1+\delta^2}{2(1-\delta)^2} + \frac{2\delta^2\ln\delta}{(1-\delta)^2(1-\delta^2)}. \tag{3.41}$$

Finally, for the democratic interaction:

$$\mathrm{Br}_{ij}^{rr} = \frac{1}{2} - \frac{2\delta^2 \ln \delta}{(1-\delta^4)}, \tag{3.42}$$

$$\mathrm{Br}_{ij}^{rr'} = \frac{1}{2} + \frac{2\delta^2 \ln \delta}{(1-\delta^4)}. \tag{3.43}$$

As it can be seen from Figures 3.1 and 3.2, as $\delta \to 0$, that is, if neutrino masses are hierarchical with $m_i >> m_j$ or $m_j = 0$, the decays become independent of the coupling constants. In addition, chirality conserving and changing decays become equally probable. On the other hand, as $\delta \to 1$, that is, if the neutrino masses are quasi-degenerate with $m_i \approx m_j$, the chirality changing decays become suppressed, except for the case of the pseudo-scalar interaction. To understand this behavior as $m_i \approx m_j$, we take Equations (3.23) and (3.24) and expand δ keeping the lowest order in $\Delta m_{ij}^2/m_i^2$:

$$\Gamma_{ij}^{rr} = \frac{m_i^2}{32\pi E_i}\left[8g_s^2\left(\frac{\Delta m_{ij}^2}{m_i^2}\right) + \frac{1}{6}g_p^2\left(\frac{\Delta m_{ij}^2}{m_i^2}\right)^3\right], \tag{3.44}$$

$$\Gamma_{ij}^{rr'} = \frac{m_i^2}{32\pi E_i}\left[\left(g_s^2 + g_p^2\right)\frac{1}{3}\left(\frac{\Delta m_{ij}^2}{m_i^2}\right)^3\right]. \tag{3.45}$$

As demonstrated by Equations (3.44) and (3.44), the decay is in general dominated by chirality-conserving fraction due to the order of dependency on $\Delta m_{ij}^2/m_i^2$, explaining the behavior of scalar and democratic interactions. However, for the case of a pseudo-scalar interaction, even though the decay is highly suppressed, the chirality-conserving and chirality-changing fractions are of comparable orders. In this context, we can approximate the branching fractions defined in Equations (3.38) – (3.43) keeping the lowest order terms in $\Delta m_{ij}^2/m_i^2$. First, for the scalar interaction:

$$\mathrm{Br}_{ij}^{rr} = 1 - \frac{1}{24}\left(\frac{\Delta m_{ij}^2}{m_i^2}\right)^2 \quad \text{and} \quad \mathrm{Br}_{ij}^{rr'} = \frac{1}{24}\left(\frac{\Delta m_{ij}^2}{m_i^2}\right)^2. \tag{3.46}$$

Next, for the pseudo-scalar interaction:

$$\mathrm{Br}_{ij}^{rr} = \frac{1}{3} + \frac{1}{120}\left(\frac{\Delta m_{ij}^2}{m_i^2}\right)^2 \quad \text{and} \quad \mathrm{Br}_{ij}^{rr'} = \frac{2}{3} - \frac{1}{120}\left(\frac{\Delta m_{ij}^2}{m_i^2}\right)^2. \tag{3.47}$$

Finally, for the democratic interaction:

$$\mathrm{Br}_{ij}^{rr} = 1 - \frac{1}{12}\left(\frac{\Delta m_{ij}^2}{m_i^2}\right)^2 \quad \text{and} \quad \mathrm{Br}_{ij}^{rr'} = \frac{1}{12}\left(\frac{\Delta m_{ij}^2}{m_i^2}\right)^2. \tag{3.48}$$

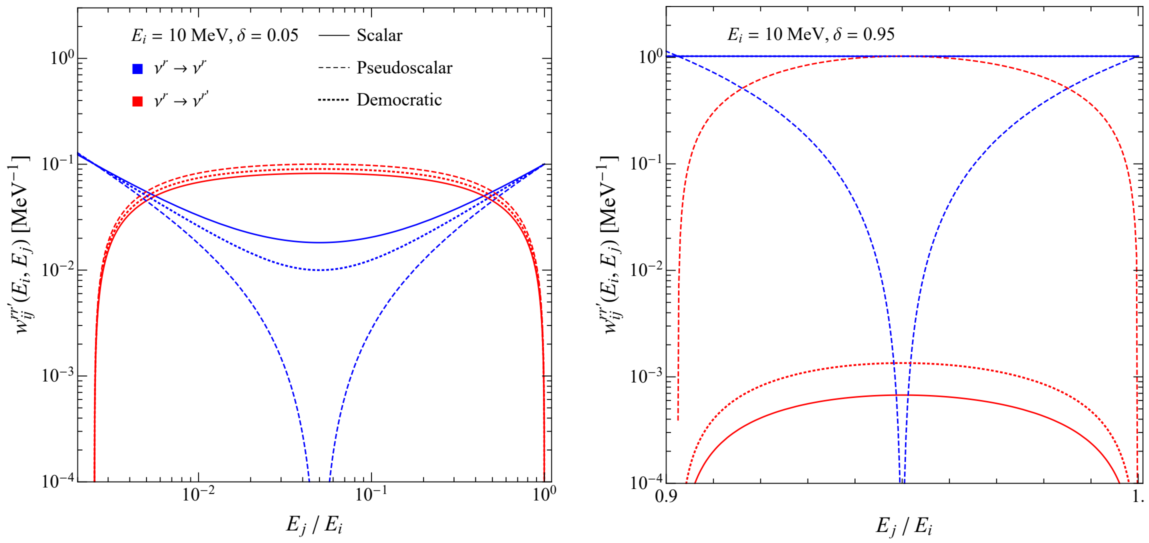

Figure 3.1: Normalized differential decay widths for the decay of a 10 MeV neutrino or antineutrino for both chirality conserving (blue curves) and changing (red curves) decays as functions of the ratio between daughter and mother neutrino energies E_j/E_i, for scalar (continuous curves), pseudo-scalar (dotted curves), and democratic (dashed curves) interactions, as defined in Equations (3.31) – (3.37). Left: $\delta = 0.05$. Right: $\delta = 0.95$.

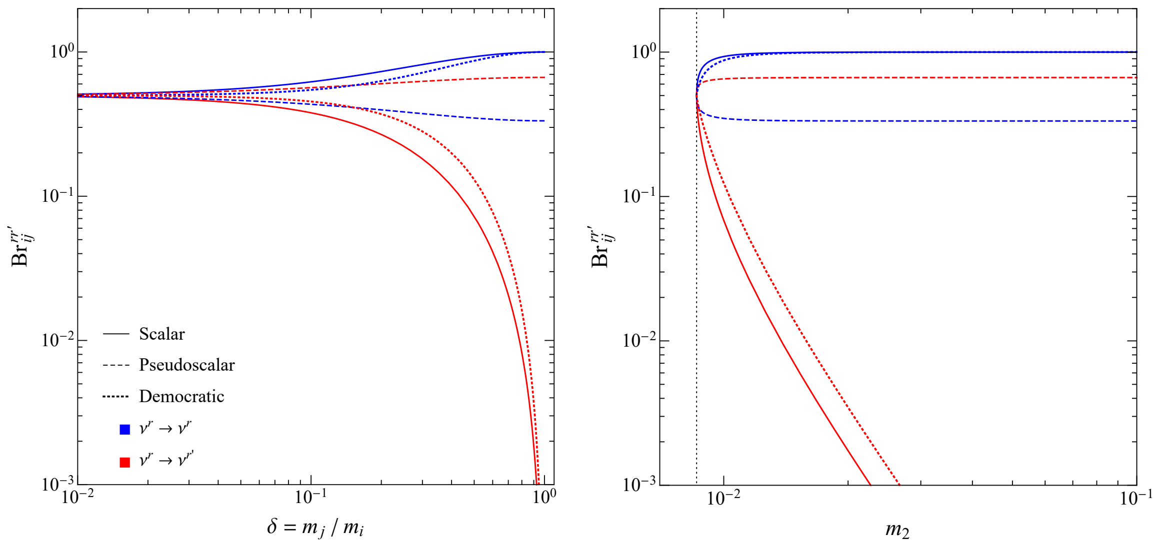

Figure 3.2: Decay branching fractions for both chirality conserving (blue curves) and changing (red curves) decays, for scalar (continuous curves), pseudo-scalar (dotted curves), and democratic (dashed curves) interactions, as defined in Equations (3.31) – (3.37). Left: Branching fractions are plotted as functions $\delta = m_j/m_i$. Right: A decay $\nu_2^r \to \nu_1^s$ is assumed and the branching fractions are plotted as a function of m_2, with vertical dotted black line representing $\delta = 0$ or correspondingly $m_2 = \sqrt{\Delta m_{21}^2}$.

The consequences of such hierarchical and quasi-degenerate decay scenarios are discussed in later sections included into the effect of neutrino oscillations.

3.2 Neutrino Oscillations with Decay

A model independent combined formalism for obtaining survival and transition probabilities including both neutrino oscillations and decay is presented by Reference [120] and summarized below. For this combined treatment, it is first necessary to introduce three operators — for propagation, appearance and disappearance — in terms of creation and annihilation operators usually noted $\hat{a}^\dagger$ and $\hat{a}$.

The Propagation Operator describes the propagation of states of energy E_i for a distance l along a baseline L. The operator is defined as

$$\mathscr{E}(l) = \sum_i \exp\left(-iE_i l\right) (\hat{a}_i^r)^\dagger \hat{a}_i^r \,. \tag{3.49}$$

The Disappearance Operator describes the amplitude of undecayed mass eigenstates of energy E_i and chirality r to remain undecayed after propagating a distance l along a baseline L. The operator is defined as

$$\mathscr{D}_-(l) = \sum_i \exp\left(-\frac{\alpha_i^r l}{2E_i}\right) (\hat{a}_i^r)^\dagger \hat{a}_i^r \,. \tag{3.50}$$

The Appearance Operator describes the destruction of states i with energy E_i and chirality r, and creation of states j with chirality s between a distance l and $l+dl$ along a baseline L. The operator is defined as

$$\mathscr{D}_+(l) = \sum_{\substack{i \\ i\neq j}} \sum_j \left(\frac{\alpha_{ij}^{rs}}{E_i}\eta_{ij}\right)^{1/2} \exp(i\xi)\, (\hat{a}_j^s)^\dagger \hat{a}_i^r \,. \tag{3.51}$$

In the expressions above, α_{ij}^{rs} is the decay rate for the $i \to j$ decay channel as defined previously, ξ is a random phase that accounts for the phase shift caused by additional not measured particles produced in the decay, and η_{ij}^{rs} describes the fraction of decay products that arrive at the detector given by

$$\eta_{ij}^{rs}(l,L,D) = \frac{1}{\Gamma_{ij}^{rs}} \int_{E_{min}}^{E_{max}} \int_{(\cos\theta)_D}^{1} \left| \frac{d\Gamma_{ij}^{rs}}{d\cos\theta dE_j}(E_i,E_j) \right| dE_j \, d\cos\theta \,, \tag{3.52}$$

where the integration limits correspond to the energy range covered by the detector and the decay angle within which the decay products can reach the detector.

The Sun is a radially symmetric neutrino source and the neutrino production area in the core is observed from Earth within a small angle $\theta_{sun} \approx 10^{-3}$. Consequently, if the decay angle is smaller than the observation angle, the daughter neutrino can reach the detector. From

Equation (3.8), it can be seen that, for ultra-relativistic neutrinos, the decay is forwardly peaked. As such, it is reasonable to suppose that every neutrino within the energy range of interest reach the detector. Hence, η_{ij}^{rs} can be approximated as independent of distance l along a baseline L, as well as the detector area perpendicular to the beam direction D. In this context:

$$\frac{d\eta_{ij}^{rs}}{dE_j} = \frac{1}{\Gamma_{ij}^{rs}} \frac{d\Gamma_{ij}^{rs}}{dE_j}(E_i, E_j)\,, \tag{3.53}$$

equals the normalized energy distribution of the decay products, describing the fraction of daughter neutrinos that reach the detector with energy between E_j and $E_j + dE_j$ after being produced from the decay of a neutrino of energy E_i.

With the operators defined above, one can now calculate the transition probabilities between neutrino eigenstates i and j for a variety of situations. A simple case is the survival probability upon decay neglecting propagation effects:

$$P_{ii}^{rr} = |\langle \nu_i^r | \mathscr{D}_-(L) | \nu_i^r \rangle|^2 = \left| \langle \nu_i^r | \left[\sum_j \exp\left(-\frac{\alpha_j^r L}{2E_j} \right) (\hat{a}_j^r)^\dagger \hat{a}_j^r \right] | \nu_i^r \rangle \right|^2 , \tag{3.54}$$

which wields

$$P_i^{\text{surv}} = P_{ii}^{rr} = \exp\left(-\frac{\alpha_i^r}{E_i} L \right) . \tag{3.55}$$

On the other hand, the appearance probability for a stable mass eigenstate ν_j produced from the decay of a unstable mass eigenstate ν_i on its propagation in a given baseline L is given by

$$\begin{aligned} P_{ij}^{rs} &= \int_0^L dl \left| \langle \nu_j^s | \mathscr{D}_+ \mathscr{D}_- | \nu_i^r \rangle \right|^2 , \\ &= \int_0^L dl \left| \langle \nu_j^s | \left[\sum_{\substack{m,n \\ m\neq n}} \left(\frac{\alpha_{mn}^{rs}}{E_m} \eta_{mn}^{rs} \right)^{1/2} (\hat{a}_n^s)^\dagger \hat{a}_m^r \right] \left[\sum_k \exp\left(-\frac{\alpha_k^r l}{2E_k} \right) (\hat{a}_k^r)^\dagger \hat{a}_k^r \right] | \nu_i^r \rangle \right|^2 . \end{aligned} \tag{3.56}$$

Hence

$$P_{ij}^{rs} = \int_0^L dl \left(\frac{\alpha_{ij}^{rs}}{E_i} \eta_{ij}^{rs} \right) \exp\left(-\frac{\alpha_i^r l}{E_i} \right) = \eta_{ij}^{rs} \left(\frac{\alpha_{ij}^{rs}}{\alpha_i^r} \right) \left(1 - \exp\left(-\frac{\alpha_i^r L}{E_i} \right) \right) . \tag{3.57}$$

where it was supposed that η_{ij}^{rs} is a constant in l. If $\nu_i^r \to \nu_j^s$ is the only possible decay channel and we suppose for the moment $\eta_{ij}^{rs} = 1$, that is, every daughter neutrino can reach the detector, it follows that the appearance/conversion probability is

$$P_i^{\text{conv}} = P_{ij}^{rs} = 1 - \exp\left(-\frac{\alpha_i^r L}{E_i} \right) . \tag{3.58}$$

Now, consider the general transition probability, now including propagation, between neutrino eigenstates i and j with n intermediate decays — $\nu_i \to \nu_k^{(1)} \to ... \to \nu_l^{(n-1)} \to \nu_j$ — denoted $P_{ij}^{(n)}$. For $n = 0$, the transition probability is given by

$$P_{ij}^{(0)} = |\left\langle \nu_j^s \,\middle|\, \mathscr{E}(L)\mathscr{D}_-(L) \,\middle|\, \nu_i^r \right\rangle|^2 . \tag{3.59}$$

$P_{ij}^{(0)}$ describes only the disappearance of the initial particle and there is not the appearance of new particles, that is, there are no decay products to be detected. As such, $P_{ij}^{(0)}$ can be identified as the transition probability for invisible decays, that is, $P_{ij}^{(0)} = P_{ij}^{inv}$.

Now, considering the transition between flavor eigenstates ν_α and ν_β along a baseline L, the survival and transition probabilities are given by

$$P_{\alpha\beta}^{inv} = |\left\langle \nu_\beta^s \,\middle|\, \mathscr{E}(L)\mathscr{D}_-(L) \,\middle|\, \nu_\alpha^r \right\rangle|^2 , \tag{3.60}$$

which, from Equation (2.10), the probability becomes

$$P_{\alpha\beta}^{inv} = \left| \sum_i \sum_j \left(U_{\alpha i}^r\right)^* \left(U_{\beta j}^r\right) \left\langle \nu_j^s \,\middle|\, \mathscr{E}(L)\mathscr{D}_-(L) \,\middle|\, \nu_i^r \right\rangle \right|^2 . \tag{3.61}$$

From Equations (3.49) and (3.50), the probability is given by

$$P_{\alpha\beta}^{inv} = \left| \sum_i \left(U_{\alpha i}^r\right)^* \left(U_{\beta i}^r\right) \exp\left(-iE_i l - \frac{\alpha_i^r l}{2E_i}\right) \right|^2 . \tag{3.62}$$

From Equation (2.20) $E_k \approx E + m_k^2/2E$, where $E = |\vec{p}_k|$ is the neutrino energy neglecting the mass contribution [7]. Similarly, we can also approximate:

$$\frac{1}{E_k} = \left(|\vec{p}_k|^2 + m_k^2\right)^{-1/2} \approx \frac{1}{E}\left(1 - \frac{m_k^2}{2E}\right) \approx \frac{1}{E} . \tag{3.63}$$

As such, the exponent in Equation (3.62) can be written as

$$\Delta_k(l) = -iE_k l - \frac{\alpha_k^r l}{2E_k} \approx -iE_\alpha l - i\frac{m_k^2 l}{2E_\alpha} - \frac{\alpha_k^r l}{2E_\alpha} = -iE_\alpha l - \frac{\tilde{m}_k^2 l}{2E_\alpha} . \tag{3.64}$$

The first term does not contribute to the probability upon expansion of the modulus in Equation (3.62), hence we can write

$$P_{\alpha\beta}^{inv} = \left| \sum_i \left(U_{\alpha i}^r\right)^* \left(U_{\beta i}^r\right) \exp\left(-\frac{\tilde{m}_i^2 l}{2E_\alpha}\right) \right|^2 . \tag{3.65}$$

For $n > 0$, on the other hand, the transition probabilities are given by

$$P_{ij}^{(n)} = \int_0^L dl_1 ... \int_{l_n-1}^L dl_n \left| \langle \nu_j^s \,|\, \mathscr{E}(L-l)\mathscr{D}_-(L-l) \left[\prod_{i=1}^n \mathscr{D}_+(l_i)\mathscr{E}(l_i)\mathscr{D}_-(l_i) \right] |\, \nu_i^r \rangle \right|^2 , \quad (3.66)$$

with $l = \sum_{i=1}^{n} l_i$. In general, if the decay mean free path is of the same order of magnitude as the baseline L, one can consider only one appearance step and neglect $n > 1$ and the only decay of interest is $\nu_i \to \nu_j$. If the decay mean free path is much shorter than the baseline L, more intermediate decays may need to be taken into account, e.g., $\nu_i \to \nu_k \to \nu_j$, as eventually allowed by decay model under scrutiny.

Since we assume that only one neutrino mass eigenstate is unstable (see Section 3.1), only one intermediate decay is possible, that is, $n \leq 1$, and we don't need to make assumptions regarding the decay mean free path at the moment. Hence, the transition and survival probabilities for visible decays can be approximated as

$$P_{ij}^{vis} = P_{ij}^{(0)} + P_{ij}^{(1)} , \quad (3.67)$$

with:

$$P_{ij}^{(1)} = \int_0^L dl \left| \langle \nu_j^s \,|\, \mathscr{E}(L-l)\mathscr{D}_-(L-l)\mathscr{D}_+(l,L)\mathscr{E}(l)\mathscr{D}_-(l) \,|\, \nu_i^r \rangle \right|^2 . \quad (3.68)$$

As before, the transition between flavor eigenstates ν_α and ν_β along a baseline L, the appearance term is given by

$$P_{\alpha\beta}^{(1)} = \int_0^L dl \left| \sum_i \sum_j \left(U_{\alpha i}^r \right)^* \left(U_{\beta j}^r \right) \langle \nu_j^s \,|\, \mathscr{E}(L-l)\mathscr{D}_-(L-l)\mathscr{D}_+(l,L)\mathscr{E}(l)\mathscr{D}_-(l) \,|\, \nu_i^r \rangle \right|^2 , \quad (3.69)$$

which, from Equations (3.49), (3.50), (3.51), and (3.64) becomes

$$P_{\alpha\beta}^{(1)} = \int_0^L dl \left| \sum_{i,\,j;i\neq j} \left(U_{\alpha i}^r \right)^* \left(U_{\beta i}^r \right) \left(\frac{\alpha_{ij}^{rs}}{E_\alpha} \eta_{ij}^{rs} \right)^{1/2} \exp\left[-\frac{\tilde{m}_i^2}{2E_\alpha} l - \frac{\tilde{m}_j^2}{2E_\beta}(L-l) \right] \right|^2 . \quad (3.70)$$

Next, to account for the energy shift in the neutrino spectrum due to visible decay, the probabilities are written as

$$\begin{aligned} \frac{dP_{\alpha\beta}^{rs}}{dE_\beta} = & \left| \sum_i \left(U_{\alpha i}^r \right)^* \left(U_{\beta i}^r \right) \exp\left(-\frac{\tilde{m}_i^2 l}{2E_\alpha} \right) \right|^2 \delta\left(E_i - E_j \right) \delta_{rs} + \\ & + \int_0^L dl \left| \sum_{i,\,j;i\neq j} \left(U_{\alpha i}^r \right)^* \left(U_{\beta j}^s \right) \left(\frac{\alpha_{ij}^{rs}}{E_\alpha} \frac{d\eta_{ij}^{rs}}{dE_\beta} \right)^{1/2} \exp\left[-\frac{\tilde{m}_i^2}{2E_\alpha} l - \frac{\tilde{m}_j^2}{2E_\beta}(L-l) \right] \right|^2 . \end{aligned} \quad (3.71)$$

Finally, the neutrino flux arriving at the detector, either in invisible or visible decays, is given by

$$\phi_\beta^s(E_\beta) = \int dE_\alpha\, \phi_\alpha^r(E_\alpha) \frac{dP_{\alpha\beta}^{rs}}{dE_\beta}(E_\alpha, E_\beta)\,, \tag{3.72}$$

that is, since a mother neutrino of energy E_α may decay producing a daughter neutrino of energy E_β, the daughter neutrino flux arriving at the detector is in general not equal the mother neutrino flux.

In the following sections, the consequences of this formalism will be examined in the context of solar neutrinos for both invisible and visible decays.

Chapter 4

Invisible Decay of Solar Neutrinos

As stated in Chapter 3, invisible decays [80, 82, 85, 92, 103–106] are those in which the products are invisible states, that is, states that either are in principle not detectable or will not be detected by the experiment in question such as the decay into sterile neutrinos plus scalar particles.

Our results presented in this Section were published [122] at Physics Letters B, volume 761, October 10th, 2016, pages 70–73 included in Appendix B. Additionally, this work was presented by O. L. G. Peres at the 38th International Conference on High Energy Physics (ICHEP 2016) and published [123] as a contribution to the conference proceedings at Proceedings of Science, volume 282, April 19th, 2017, page 464.

4.1 Formalism

As shown in Figure 4.1, established limits before this work (see Section 3.1) on the neutrino lifetime imply that neutrinos do not substantially decay either inside the Sun or Earth. As such, we can take into consideration that neutrino decay only in vacuum on their way from Sun to Earth, and Equation (3.65) can be rewritten as

$$P_{e\beta}^{\text{invis}} = \left| \sum_i A_{ei}^{\odot} A_{i\beta}^{\oplus} \exp\left(-i\frac{m_i L}{2E_\alpha}\right) \exp\left(-\frac{\alpha_i^r L}{2E_\alpha}\right) \right|^2 , \tag{4.1}$$

where $A_{ei}^{\odot}$ is the transition amplitude of an electron neutrino produced in the solar core to be in a ν_i state in the solar surface, and $A_{i\beta}^{\oplus}$ is the transition amplitude of a ν_i to be in a ν_β state upon detection on Earth. In addition, by expanding the expression above and neglecting interference terms, as done in Chapter 2, it is possible to rewrite it as the incoherent sum of probabilities:

$$P_{e\beta}^{\text{invis}} = \sum_i P_{ei}^{\odot} P_i^{surv} P_{i\beta}^{\oplus} , \tag{4.2}$$

where $P^{\odot}_{ei} = \left|A^{\odot}_{ei}\right|^2$ is the probability of the produced ν_e be found as a ν_i at the surface of the Sun, $P^{\oplus}_{i\beta} = \left|A^{\oplus}_{i\beta}\right|^2$ is the probability of a ν_i be detected as a ν_β on Earth, and P^{surv}_i is the decay survival probability of an eigenstate i upon propagating the Sun-Earth distance

$$P^{\text{surv}}_i = P^{rr}_{ii} = \exp\left(-\frac{\alpha^r_i}{E_\alpha}L\right) . \tag{4.3}$$

as given by Equation (3.55) and shown in Figure 4.1.

As previously seen in Figure 2.3, in the LMA-MSW solution, a 10 MeV ν_e will be produced almost as a pure ν_2 and, due to the adiabatic crossing of the resonance region, it will still reach the solar surface as ν_2. *As such, the most interesting scenario for the invisible decay of solar neutrinos is to assume the mass eigenstate ν_2 is unstable and decays into invisible states.* Hence, the survival and transition probabilities for two neutrino families is given by

$$P'_{ee} = P^{\odot}_{e1} P^{\oplus}_{1e} + P^{\odot}_{e2} P^{\text{surv}}_2 P^{\oplus}_{2e} , \tag{4.4}$$
$$P'_{e\mu} = P^{\odot}_{e1} P^{\oplus}_{1\mu} + P^{\odot}_{e2} P^{\text{surv}}_2 P^{\oplus}_{2\mu} . \tag{4.5}$$

Figure 4.2 shows the day survival probability as defined in Equation (4.4)for electron neutrinos produced in the Sun and detected on Earth for different values of τ_2/m_2 with the Earth-Sun distance set to 1 A.U.

In the context of neutrino invisible decay it is also useful to separate the neutrino fluxes for three neutrino families into electronic and non-electronic flavors. Following the discussion presented in Section 2.3.1, we can approximate the probabilities as

$$P_{ee} = c^4_{13} P'_{ee} + s^4_{13} , \tag{4.6}$$

for the electron neutrino survival probability, and

$$P_{e(\mu+\tau)} = c^2_{13} P'_{e\mu} + s^2_{13} c^2_{13} P'_{ee} + s^2_{13} c^2_{13} . \tag{4.7}$$

for the transition probability. On both survival and transition probabilities, the primed probabilities are the two-family probabilities on Equations (4.4) and (4.5).

Due to decay, either in two or three neutrino families, it no longer holds that the sum of probabilities is equal to unity, that is

$$\sum_{\beta=e,\mu,\tau} P_{e\beta} = 1 - c^2_{13} P^{\odot}_{e2} \left(1 - P^{\text{surv}}_2\right) . \tag{4.8}$$

This non-unitary evolution is discussed in more detail in Reference [124].

Another consequence of this scenario is that, for appreciable values of τ_2/m_2, the solar neutrino data can be explained by a combination of standard three neutrino MSW oscillation and decay, leading to a degenerescence between neutrino parameters, specially

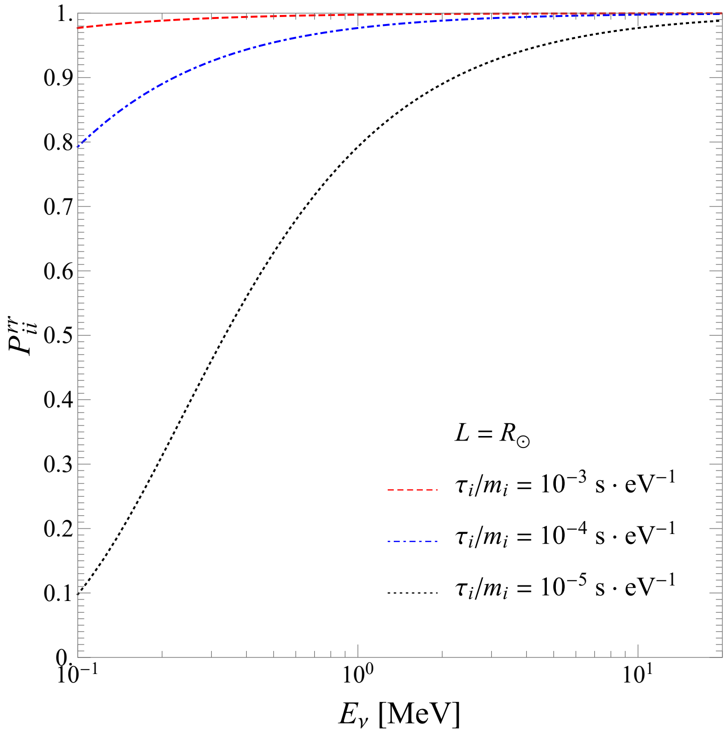

Figure 4.1: Survival Probability $P_i^{\text{surv}} = P_{ii}^{rr}$ as a function of the neutrino energy E_ν as given by Equation (3.55), for selected values of the lifetime τ_i/m_i, for propagation over the solar radius distance.

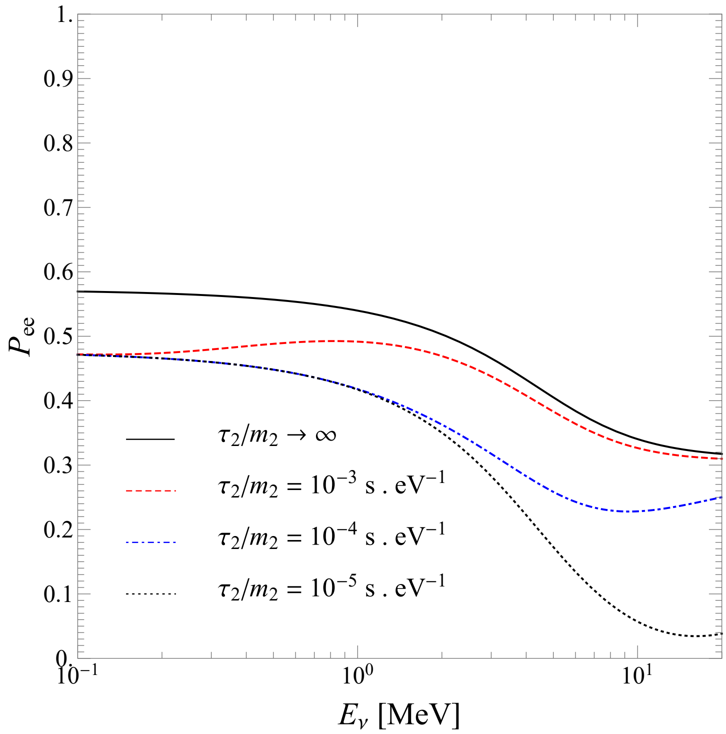

Figure 4.2: Day Survival Probabilities for electron neutrinos produced in the Sun and detected on Earth for different values of τ_2/m_2 with the Earth-Sun distance set to 1 A.U.. Best-fit values for the global fit neutrino oscillation parameters [59] as shown on Table 2.1 are used.

Δm^2_{21} and τ_2/m_2 [99]. As such, solar neutrino data can be used to set lower limits to τ_2/m_2.

4.2 Solar Neutrino Analysis with Decay

For the invisible decay analysis, the author of this thesis modified a code written in Fortran and used for solar neutrino analysis (e.g. in References [125–127]) to account for solar neutrino decay.

In this code, the neutrino survival probabilities as shown in Equations (4.6) and (4.7) are numerically calculated under the assumption of adiabatic evolution inside the Sun. Next, the expected event rate is computed for each relevant experiment and compared to their data. The data included in the analysis are the Homestake total rate [10], GALLEX and GNO combined total rate [128], SAGE total rate [16], SuperKamiokande I full energy and zenith spectrum [22], SNO combined analysis [32] and Borexino 192-day low-energy data [37].

Finally, the χ^2 statistical analysis was performed using a χ^2 function built from the relevant parameters

$$\chi^2_\odot = \chi^2_\odot(\tan^2\theta_{12}, \Delta m^2_{21}, \sin^2\theta_{13}, \tau_2/m_2)\,, \tag{4.9}$$

and the allowed regions are shown in Figure 4.3.

Complementary information can be added from the reactor experiments KamLAND (KL) [62] and Daya Bay (DB) [129], since these experiments give precise constraints on Δm^2_{21} and $\sin^2\theta_{13}$ from their detection of $\bar{\nu}_e$ oscillations. For the currently allowed values of τ_2/m_2, $P_{22} \sim 1$ for the typical baselines of $L/E_\nu \sim 10^{-10}\,\mathrm{s}\cdot\mathrm{eV}^{-1}$ and $\sim 10^{-12}\,\mathrm{s}\cdot\mathrm{eV}^{-1}$ of KamLAND and Daya Bay respectively. In this case, the relevant neutrino probability is the standard three neutrino expression:

$$P(\bar{\nu}_e \to \bar{\nu}_e) = 1 - c^4_{13} S^2_{12} \sin^2\Delta_{21} - S^2_{13}\sin^2\Delta m^2_{ee}\,, \tag{4.10}$$

where $S_{ij} = \sin 2\theta_{ij}$, $\Delta_{ij} = \Delta m^2_{ij}/4E_\nu$ and $\Delta m^2_{ij} \equiv m^2_i - m^2_j$, and an effective mass square difference is defined as $\sin^2\Delta m^2_{ee} \equiv c^2_{12}\sin^2\Delta_{31} + s^2_{12}\sin^2\Delta_{32}$. Hence, decay can be neglected in the context of these experiments and their standard neutrino analysis for three neutrinos can also be used for decay scenario. In other words:

$$\chi^2_{\text{decay; KL / DB}} = \chi^2_{\text{no decay; KL / DB}}\,, \tag{4.11}$$

and their data can be included as reported in the analysis.

For the KamLAND experiment, a χ^2_{KL} function for the standard three neutrino scenario used in Reference [62] is available in table format as a function of $\tan^2\theta_{12}$, Δm^2_{21} and $\sin^2\theta_{13}$. For the Daya Bay experiment, the χ^2_{DB} function is available in table format provided in the supplementary material from Reference [129] as a function of Δm^2_{ee} and $\sin^2(2\theta_{13})$. The

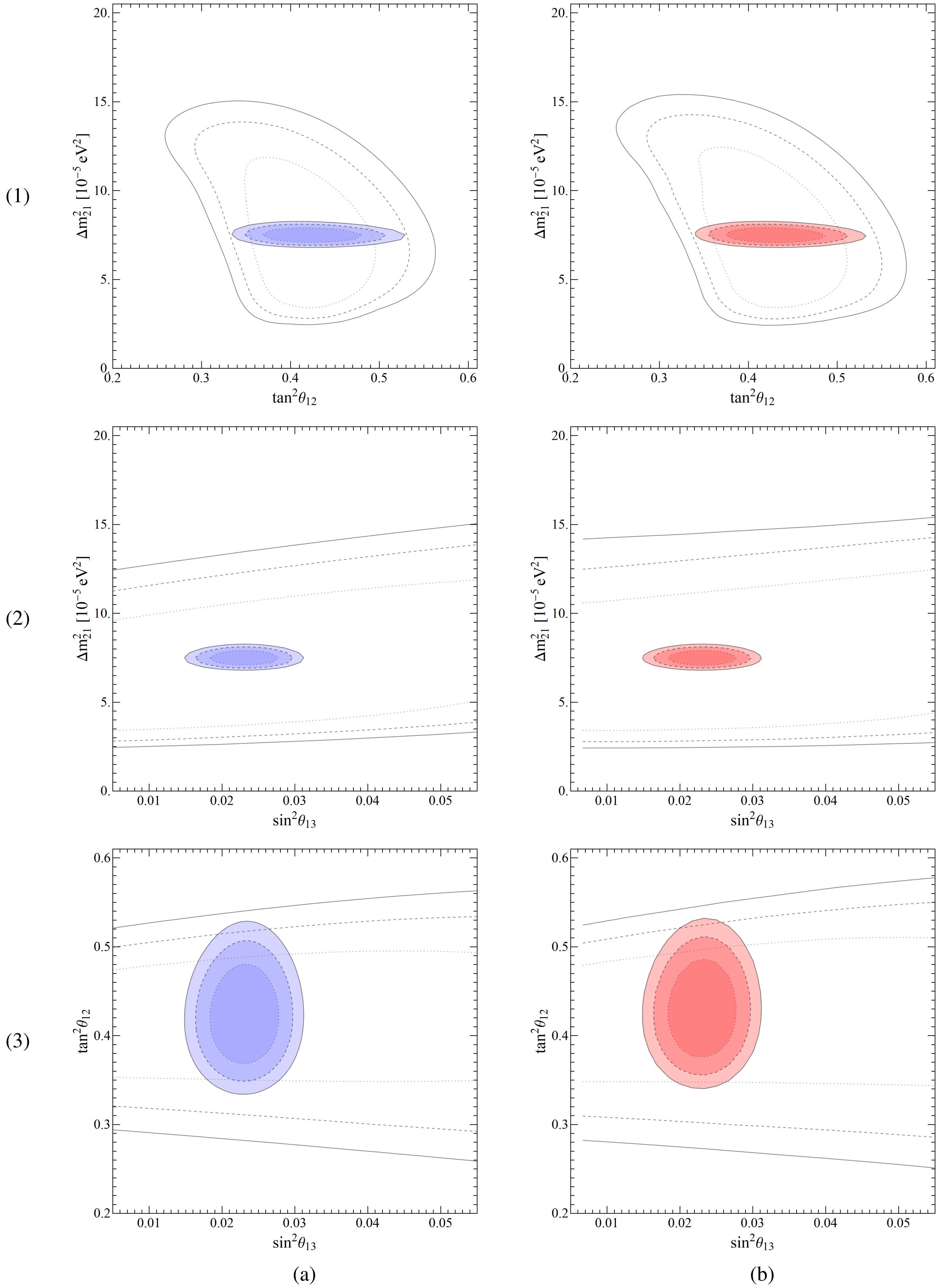

Figure 4.3: Left: Allowed parameter regions for the standard oscillation parameters (Δm^2_{21}, θ_{12} and θ_{13}) without decay. Right: Allowed parameter regions for the standard oscillation parameters (Δm^2_{21}, θ_{12} and θ_{13}) including decay. The hollow curves represent the analysis with only solar neutrino data and the filled curves represent the combined analysis of solar, KamLAND and Daya Bay data. The dotted, dashed and continuous line represent respectively 90% C.L., 99% C.L. and 99.9% C.L.. Plots (1a) through (3b) were made for this thesis.

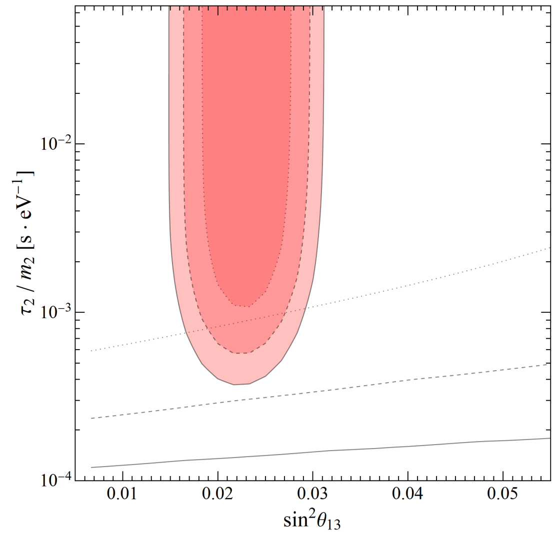

(a)

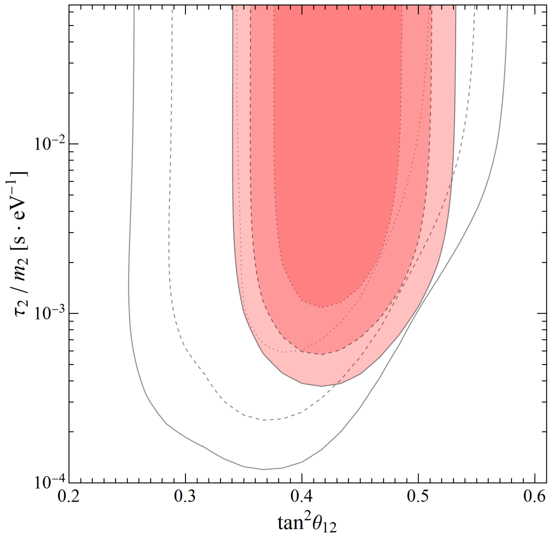

(b)

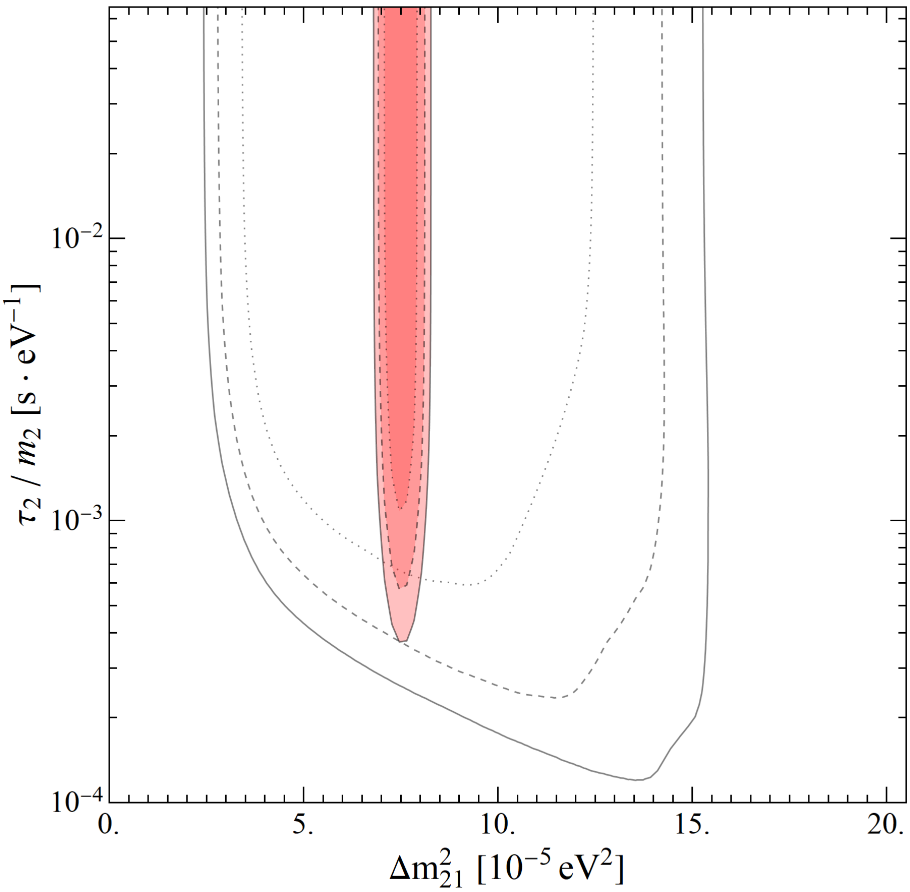

(c)

Figure 4.4: Allowed parameter regions for the standard oscillation parameters (Δm^2_{21}, θ_{12} and θ_{13}) and the decay parameter τ_2/m_2. The hollow curves represent the analysis with only solar neutrino data and the filled curves represent the combined analysis of solar, KamLAND and Daya Bay data. The dotted, dashed and continuous line represent respectively 90% C.L., 99% C.L. and 99.9% C.L.. Plots (a) and (b) were made for this thesis, plot (c) was published alongside our results in [122].

combined χ^2 function for solar, KamLAND and Daya Bay data is written as

$$\begin{aligned}\chi^2 = \chi^2_{\odot}\left(\tan^2\theta_{12}, \Delta m^2_{21}, \sin^2\theta_{13}, \tau_2/m_2\right) + \\ + \chi^2_{\mathrm{KL}}\left(\tan^2\theta_{12}, \Delta m^2_{21}, \sin^2\theta_{13}\right) + \chi^2_{\mathrm{DB}}\left(\Delta m^2_{ee}, \sin^2\theta_{13}\right) ,\end{aligned} \tag{4.12}$$

where Δm^2_{ee} was defined before and over which we can promptly marginalize the χ^2. From Equation (4.12), we find the allowed regions for independent parameters $\tan^2\theta_{12}$, $\sin^2\theta_{13}$, Δm^2_{21}, and τ_2/m_2 as shown in Figures 4.3 and 4.4.

By marginalizing over the first two, we obtain the allowed region for the mass squared difference Δm^2_{21} and the decay parameter τ_2/m_2 as shown in Figure 4.4, where the hollow (filled) regions show the results for the solar neutrino (combined) analysis.

The degenerescence between Δm^2_{21} and τ_2/m_2 is evident in the hollow regions of Figure 4.4, where higher values for Δm^2_{21} are allowed alongside lower values for τ_2/m_2 and lower values for Δm^2_{21} are allowed alongside higher values for τ_2/m_2.

High values of Δm^2_{21} are ruled out in the standard neutrino scenario because it leads to spectral distortions that are disfavored by the solar neutrino data. On the other hand, high values of Δm^2_{21} could become a viable solution at the cost of having lower values of τ_2/m_2. The inclusion of KamLAND and Daya Bay data break this degenerescence due to their precise independent measurement of Δm^2_{21} and $\sin^2\theta_{13}$ respectively. Thus, from the complementary data, it is possible to precisely isolate the contribution of the decay parameter τ_2/m_2. The

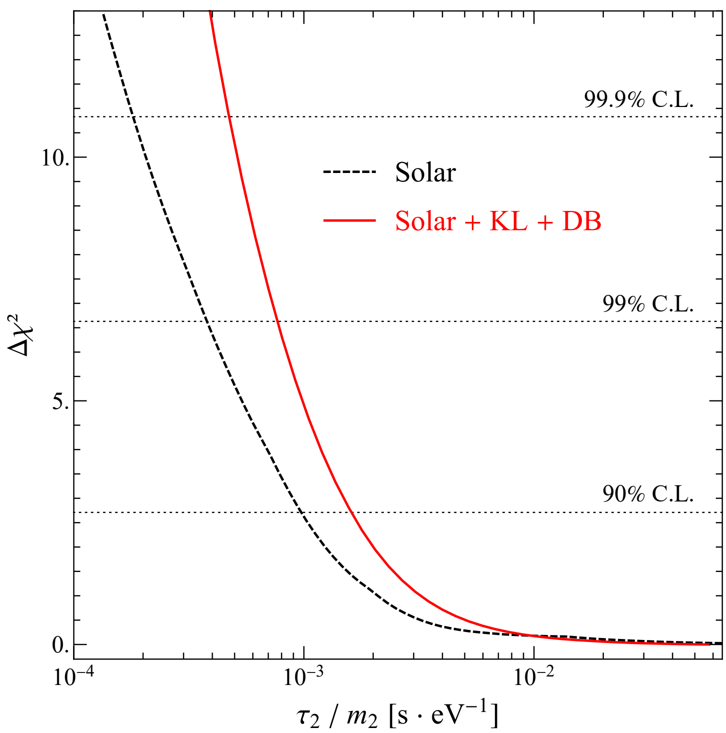

Figure 4.5: $\Delta\chi^2$ for ν_2 lifetime τ_2/m_2. The dashed (continuous) curve shows the solar (combined) neutrino data analysis. Plot published alongside our results in [122].

complete marginalization over the standard parameters results in the curve shown in Figure 4.5 of $\Delta\chi^2$ as a function of τ_2/m_2. From it, we can extract a lower limit to the ν_2 eigenstate lifetime

$$\tau_2\,/\,m_2 \geq 7.7\times 10^{-4}\,\mathrm{s}\cdot\mathrm{eV}^{-1}\,, \quad \text{at } 99\%\ \text{C.L.}\,, \tag{4.13}$$

which corresponds to an upper bound to the decay parameter $\alpha_2 \leq 8.5\times 10^{-13}\,\mathrm{eV}^2$.

4.3 Seasonal Effect due to Decay

One interesting consequence of the decay scenario that had not been previously discussed in the literature is the effect of neutrino decay in the seasonal variation of solar neutrino flux. In the absence of decay, the neutrino flux arriving on Earth is given by

$$\phi_\nu^\oplus = \frac{\phi_\nu^\odot}{4\pi r^2}\,, \tag{4.14}$$

where $r = r(t)$ is the time-dependent Earth-Sun distance. The ratio between maximum (at perihelion) and minimum (at aphelion) fluxes is

$$R_0 = \frac{(1+\varepsilon_0)^2}{(1-\varepsilon_0)^2}\,, \tag{4.15}$$

where $\varepsilon_0 = 0.0167$ is the eccentricity of Earth's orbit.

The inclusion of decay modifies the ratio between maximum and minimum neutrino fluxes and, consequently, also the measured eccentricity ε as given by

$$R = R_0\,\frac{N(r_{\mathrm{per}})}{N(r_{\mathrm{aph}})} = \frac{(1+\varepsilon)^2}{(1-\varepsilon)^2}\,, \tag{4.16}$$

where r_{aph} (r_{per}) is the aphelion (perihelion) distance and N is the number of events calculated from the convolution of the adequate probabilities and cross sections for each experiment.

From Equations (4.6) and (4.7), it follows that $N(r_{\mathrm{per}}) > N(r_{\mathrm{aph}})$ holds also for the decay scenario due to P_{22} dependence on the orbital distance. This implies that $R > R_0$ for all energies and thus, for any neutrino decay scenario, an enhancement in the seasonal variation of the solar neutrino flux would be expected. The measurement of an eccentricity $\varepsilon > \varepsilon_0$ is a hint in the direction of the neutrino decay scenario. In fact, some experiments have measured Earth's orbital eccentricity to be different than the standard value albeit still compatible with ε_0 as shown in Table 4.1.

Figure 4.6 shows the dependence of the neutrino eccentricity ε with the neutrino lifetime τ_2/m_2 as it would be measured by SuperKamiokande (SK), SNO and Borexino (BOR) experiments. As it can be seen, the higher energy ^{8}B solar neutrinos (measured by SK and SNO) would have a greater seasonal variation due to decay than the lower energy ^{7}Be solar

Table 4.1: Experimental best-fit values and errors for Earth's orbital eccentricity ε for different solar neutrino experiments. We also show the ratio between the fitted values and Earth's eccentricity ε_0.

Experiment	$\varepsilon_{\rm exp} \pm \sigma_{exp}$	$\left(\varepsilon_{\rm exp} \pm \sigma_{exp}\right)/\varepsilon_0$
Borexino [36]	0.0398 ± 0.0102	2.38 ± 0.61
SuperKamiokande-I [130]	0.0252 ± 0.0072	1.51 ± 0.43
SNO Phase I [131]	0.0143 ± 0.0086	0.86 ± 0.51

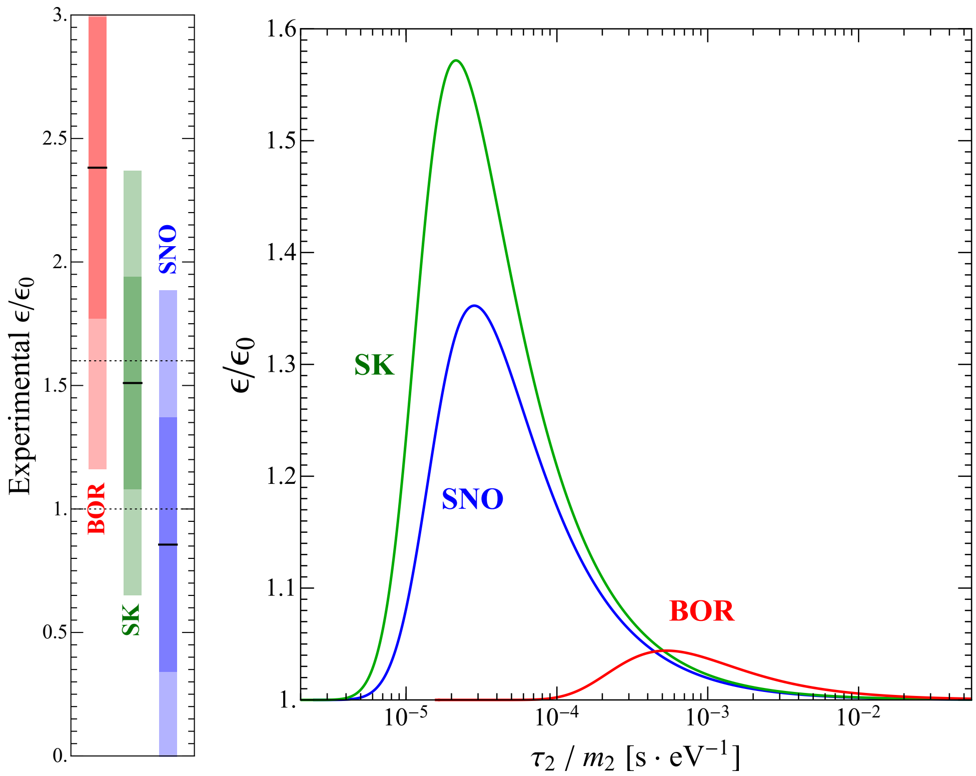

Figure 4.6: Left: Experimental values for $\varepsilon/\varepsilon_0$. Black lines are the best-fit values and darker (lighter) shades are the 1σ (2σ) ranges as shown in Table 4.1. Right: Dependence of the orbital eccentricity ε with the neutrino lifetime τ_2/m_2 as it would be measured by different experiments — the ^{7}Be line in Borexino (BOR), and the ^{8}B spectrum in SuperKamiokande (SK) and SNO. Plots published alongside our results in [122].

neutrinos (measured by Borexino).

Due to the MSW effect, the ν_2 content in the neutrino flux leaving the Sun is energy dependent. At higher energies, there are more ν_2 neutrinos available for decay during the propagation to Earth. On the other hand, for lower energy neutrinos, there are fewer ν_2 leaving the sun and thus fewer ν_2 available for decay. For this reason, the seasonal variation for higher energy neutrinos would be bigger than for lower energy neutrinos and, consequently, also the measured eccentricity. From Figure 4.6, it can be seen that due to the decay survival probability in Equation (3.2), the lower (higher) the energy of the neutrinos, the bigger (smaller) is the lifetime for which the enhancement in the eccentricity is maximum.

We can now include the eccentricity data in the analysis as a penalty function added to the χ^2 for each experiment:

$$\chi^2_{\text{seasonal}} = \frac{(\varepsilon_{\text{exp}} - \varepsilon)^2}{(\sigma_{\text{exp}})^2}. \tag{4.17}$$

The marginalization of the combined $\Delta\chi^2$ results in a slightly lower value

$$\tau_2\,/\,m_2 \geq 7.2 \times 10^{-4}\,\text{s}\cdot\text{eV}^{-1}, \quad \text{at 99\% C.L.} \tag{4.18}$$

for the decay parameter due to the fact that the current eccentricity measurements and errors will favor lower, already excluded, lifetimes, for which the enhancement in the seasonal variation (and hence the measured eccentricity) is higher.

4.4 Results

Our result for ν_2 neutrino lifetime at $\tau_2\,/\,m_2 \geq 7.2 \times 10^{-4}\,\text{s}\cdot\text{eV}^{-1}$, at 99% C.L. can be compared to previous results available. Our result is almost one order higher than the previously established bound in Reference [99] at $\tau_2/m_2 \geq 8.7 \times 10^{-5}\,\text{s}\cdot\text{eV}^{-1}$ at 99% C.L. and it is similar to but more constrained than the bound reported in Reference [132].

Our results were published [122] at Physics Letters B, volume 761, October 10$^{\text{th}}$, 2016, pages 70–73 included in Appendix B. Additionally, this work was presented by O. L. G. Peres at the 38$^{\text{th}}$ International Conference on High Energy Physics (ICHEP 2016) and published [123] at Proceedings of Science, volume 282, April 19$^{\text{th}}$, 2017, page 464.

Later, the SNO collaboration performed a new analysis [112] including all three phases of ^{8}B solar neutrino data taken by the Sudbury Neutrino Observatory (SNO) which, combined with data from other solar neutrino experiments, resulted in an improved limit for ν_2 neutrino lifetime at $\tau_2\,/\,m_2 \geq 1.02 \times 10^{-3}\,\text{s}\cdot\text{eV}^{-1}$, at 99% C.L.. Table 4.2 compares our result to the lower limits to τ_2/m_2 presented in the literature.

Table 4.2: Lower limits to τ_2/m_2 [$\text{s}\cdot\text{eV}^{-1}$] in the literature compared to our results.

Analysis	τ_2/m_2 [$\text{s}\cdot\text{eV}^{-1}$]
Bandyopadhyay *et al.* [99]	8.7×10^{-5} at 99% C.L.
Berryman *et al.* [132]	7.1×10^{-4} at 2σ C.L.
Picoreti *et al.* (this work) [122]	7.2×10^{-4} at 99% C.L.
Aharmim *et al.* (SNO Collaboration) [112]	1.02×10^{-3} at 99% C.L.

Chapter 5

Visible Decay of Solar Neutrinos

As stated in Chapter 3, visible decays [83, 84, 107–111] are those in which the products are visible states, that is, at least one of the daughter particles is in principle detectable, e.g., the decay of a mass eigenstate into at least one lighter active mass-eigenstate. For the analysis of this decay scenario, one is also interested in the daughter particle and how it affects the final neutrino fluxes.

The work described in this Section is original, not yet submitted to publication. This is the first time that an analysis is made in visible decay scenario properly including a neutrino decay model.

5.1 Formalism

In the context of three neutrino families, the set of decay channels available for each neutrino mass eigenstate is schematically shown in Figure 5.1 for both mass hierarchies.

As discussed before, from Figure 2.3, in the LMA-MSW solution, a 10 MeV ν_e will be produced almost as a pure ν_2 and, due to the adiabatic crossing of the resonance region, it will still reach the solar surface as ν_2. Hence, due to the smallness of ν_3 content in the electron neutrino (see Section 2.3.1 and Figure 2.6) and to the smallness of ν_1 content in the solar electron neutrinos in energy range under consideration, the most interesting scenario for the visible decay of solar neutrinos is to assume the mass eigenstate ν_2 is unstable decaying into lighter neutrinos. From Figure 5.1, the possible decay channels for ν_2 are

- $\nu_2 \to \nu_1/\bar{\nu}_1$ in the normal hierarchy, and
- $\nu_2 \to \nu_1/\bar{\nu}_1$ and $\nu_2 \to \nu_3/\bar{\nu}_3$ in the inverted hierarchy.

Each of the decay channels above available for the ν_2 eigenstate will be analyzed in the context of solar neutrino decay so that lifetime limits to ν_2 can be extracted for each mass hierarchy.

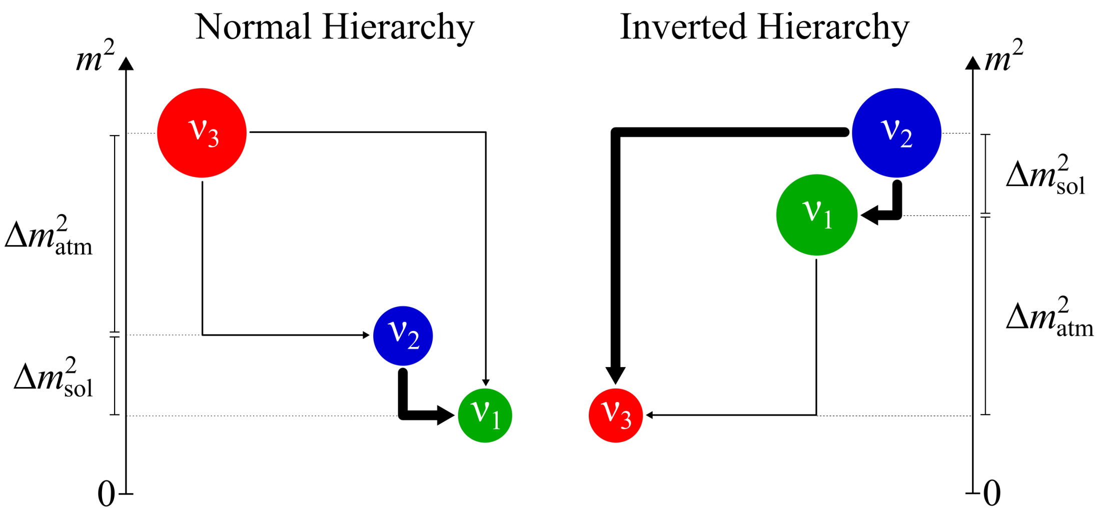

Figure 5.1: Schematics of the possible neutrino decay channels in the context of three neutrino families and for both the normal and inverted hierarchies. Highlighted arrows show the decay channels available for the ν_2 eigenstate which are investigated in the following sections in the context of solar neutrino decay so that lifetime limits to ν_2 can be extracted for each mass hierarchy.

For solar neutrinos, by the same considerations made for the invisible decay scenario, Equation (3.71) can be rewritten as

$$\begin{aligned}\frac{dP^{rs}_{\alpha\beta}}{dE_\beta} &= \left|\sum_i A^{\odot}_{ei} A^{\oplus s}_{i\beta} \exp\left(-\frac{\tilde{m}^2_i l}{2E_\alpha}\right)\right|^2 \delta\left(E_\alpha - E_\beta\right)\delta_{rs} + \\ &+ \int_0^L dl \left|\sum_{i,j;i\neq j} A^{\odot}_{ei} A^{\oplus s}_{i\beta} \left(\frac{\alpha^{rs}_{ij}}{E_\alpha}\frac{d\eta^{rs}_{ij}}{dE_\beta}\right)^{1/2} \exp\left[-\frac{\tilde{m}^2_i}{2E_\alpha} l - \frac{\tilde{m}^2_j}{2E_\beta}(L-l)\right]\right|^2,\end{aligned} \tag{5.1}$$

which, using Equation (3.53), becomes

$$\begin{aligned}\frac{dP^{rs}_{e\beta}}{dE_\beta} &= \left|\sum_i A^{\odot}_{ei} A^{\oplus s}_{i\beta} \exp\left(-\frac{\tilde{m}^2_i l}{2E_\alpha}\right)\right|^2 \delta\left(E_\alpha - E_\beta\right)\delta_{rs} + \\ &+ \int_0^L dl \left|\sum_{i,j;i\neq j} A^{\odot}_{ei} A^{\oplus s}_{j\beta} \left(\frac{d\Gamma^{rs}_{ij}}{dE_\beta}\right)^{1/2} \exp\left[-\frac{\tilde{m}^2_i}{2E_\alpha} l - \frac{\tilde{m}^2_j}{2E_\beta}(L-l)\right]\right|^2.\end{aligned} \tag{5.2}$$

The first term is treated in Chapter 4. Now, we focus on the second term integrand:

$$\frac{dP}{dl} = \left|\sum_{i,j;i\neq j} A^{\odot}_{ei} A^{\oplus s}_{j\beta} \left(\frac{d\Gamma^{rs}_{ij}}{dE_\beta}\right)^{1/2} \exp\left[-\frac{\tilde{m}^2_i}{2E_\alpha} l - \frac{\tilde{m}^2_j}{2E_\beta}(L-l)\right]\right|^2. \tag{5.3}$$

Consider that only one single mass eigenstate ν_i is unstable, with allowed decay channels into ν_j and $\bar{\nu}_j$. As such, the expression above becomes

$$\frac{dP}{dl} = \left| A^{\odot}_{ei} A^{\oplus s}_{j\beta} \left(\frac{d\Gamma^{rs}_{ij}}{dE_\beta} \right)^{1/2} \exp\left[-i\frac{m_i^2}{2E_\alpha} l - \frac{\alpha_i}{2E_\alpha} l - i\frac{m_j^2}{2E_\beta}(L-l) \right] \right|^2 , \tag{5.4}$$

from which it follows that

$$\frac{dP}{dl} = \left|A^{\odot}_{ei}\right|^2 \left|A^{\oplus s}_{j\beta}\right|^2 \left(\frac{d\Gamma^{rs}_{ij}}{dE_\beta} \right) e^{-\Gamma_i l} = P^{\odot}_{ei} P^{\oplus s}_{j\beta} \left(\frac{d\Gamma^{rs}_{ij}}{dE_\beta} \right) e^{-\Gamma_i l} . \tag{5.5}$$

Consequently:

$$\int_0^L dl \frac{dP}{dl} = P^{\odot}_{ei} \left(1 - e^{-\Gamma_i L}\right) \left(\frac{1}{\Gamma_i} \frac{d\Gamma^{rs}_{ij}}{dE_\beta} \right) P^{\oplus s}_{j\beta} = P^{\odot}_{ei} P^{\mathrm{conv}}_i w^{rs}_{ij} P^{\oplus s}_{j\beta} . \tag{5.6}$$

where $P^{\mathrm{conv}}_i = 1 - P^{\mathrm{surv}}_i$ is as defined in Equation (3.58). Hence:

$$\frac{dP^{rs}_{e\beta}}{dE_\alpha} = \left(\sum_k P^{\odot}_{ek} P^{\mathrm{surv}}_k P^{\oplus}_{k\beta} \right) \delta\left(E_\alpha - E_\beta\right) \delta_{rs} + P^{\odot}_{ei} P^{\mathrm{conv}}_i w^{rs}_{ij} P^{\oplus s}_{j\beta} . \tag{5.7}$$

Finally, the neutrino flux of each flavor arriving at the detector is given by

$$\phi^s_\beta(E_\beta) = \phi^{s,\,\mathrm{invis}}_\beta(E_\beta)\, \delta_{rs} + \int dE_\alpha\, \phi^r_\alpha(E_\alpha) P^{\odot}_{ei} P^{\mathrm{conv}}_i w^{rs}_{ij} P^{\oplus s}_{j\beta} , \tag{5.8}$$

with integration limits $\left[E_\beta, E_\beta/\delta^2\right]$ as obtained from Equation (3.6). As before, $P^{\odot}_{ek} = \left|A^{\odot}_{ek}\right|^2$ is the probability of the produced ν_e be found as a ν_k at the surface of the Sun, $P^{\oplus}_{k\beta} = \left|A^{\oplus}_{k\beta}\right|^2$ is the probability of a ν_k be detected as a ν_β on Earth, and P^{conv}_i is the transition probability of an eigenstate i into an eigenstate j upon propagating the Sun-Earth distance L as given in Equation (3.58). Additionally, the weighted differential decay width w^{rs}_{ij} is given in Equations (3.29) and (3.30) for a generic interaction and in Equations (3.31) – (3.37) for three particular cases for the coupling constants. In later sections, the probabilities $P^{\oplus s}_{1\beta}$ are assumed as the day probabilities, that is

$$P^{\oplus}_{1e} = \cos^2\theta_{12} , \quad P^{\oplus}_{1\mu} = \sin^2\theta_{12} , \quad P^{\oplus}_{\bar{1}\bar{e}} = \cos^2\theta_{12} , \quad \text{and } P^{\oplus}_{\bar{1}\bar{\mu}} = \sin^2\theta_{12} . \tag{5.9}$$

5.2 Neutrino Mass Hierarchies and Decay Channels

As presented in Section 3.1, the weighted differential decay width w^{rs}_{ij} depend on the quantity $\delta = m_j/m_i$. In the absence of any other information regarding the absolute values of neutrinos masses, there are two possible simplified scenarios:

- either $m_j = 0$ or $m_i >> m_j$, that is, the neutrino masses are hierarchical and $\delta \to 0$;

- $m_i \approx m_j$, that is, the neutrino masses are quasi-degenerate and $\delta \to 1$.

In the hierarchical scenario, as discussed before, the decay become independent of the coupling constants. As such, from Equations (3.31) - (3.37), we are left with the weighted differential decay width:

$$w_{ij}^{rs} = \begin{cases} \dfrac{1}{E_\alpha}\left(\dfrac{E_\beta}{E_\alpha}\right) & \text{for } \nu_i \to \nu_j \\ \dfrac{1}{E_\alpha}\left(1-\dfrac{E_\beta}{E_\alpha}\right) & \text{for } \nu_i \to \bar{\nu}_j \end{cases} . \tag{5.10}$$

On the other hand, in the quasi-degenerate scenario, according to Equation (3.10), as $\delta \to 1$, $E_\beta \approx E_\alpha$. In other words, the energy shift upon decay is very small and the daughter neutrino is detected with approximately the same energy bin as the parent neutrino would have been detected. Hence, in this scenario, we can approximate η_{ij}^{rs} as

$$\frac{d\eta_{ij}^{rs}}{dE_\beta} = \delta\left(E_\alpha - E_\beta\right) . \tag{5.11}$$

By replacing Equation (5.11) in Equation (5.1) it becomes

$$\begin{aligned} \frac{dP_{e\beta}^{rs}}{dE_\beta} = & \left| \sum_i A_{ei}^{\odot} A_{i\beta}^{\oplus s} \exp\left(-\frac{\tilde{m}_i^2 l}{2E_\alpha}\right)\right|^2 \delta\left(E_\alpha - E_\beta\right)\delta_{rs} + \\ & + \int_0^L dl \left| \sum_{i,j;i\neq j} A_{ei}^{\odot} A_{j\beta}^{\oplus s}\left(\Gamma_{ij}^{rs}\right)^{1/2} \exp\left[-\frac{\tilde{m}_i^2}{2E_\alpha} l - \frac{\tilde{m}_j^2}{2E_\beta}(L-l)\right]\right|^2 \delta\left(E_\alpha - E_\beta\right) . \end{aligned} \tag{5.12}$$

As before, considering that only one single mass eigenstate ν_i is unstable, with allowed decay channels into ν_j and $\bar{\nu}_j$, the second term integrand becomes

$$\frac{dP}{dl} = P_{ei}^{\odot} P_{j\beta}^{\oplus s} \Gamma_{ij}^{rs} e^{-\Gamma_i l} , \tag{5.13}$$

and consequently:

$$\int_0^L dl \frac{dP}{dl} = P_{ei}^{\odot}\left(1 - e^{-\Gamma_i L}\right)\left(\frac{\Gamma_{ij}^{rs}}{\Gamma_i}\right) P_{j\beta}^{\oplus s} = P_{ei}^{\odot} P_i^{\text{conv}} \text{Br}_{ij}^{rs} P_{j\beta}^{\oplus s} . \tag{5.14}$$

Hence, the neutrino flux of each flavor arriving at the detector is given by

$$\phi_\beta^s(E_\beta) = \phi_\beta^{s,\text{invis}}(E_\beta)\,\delta_{rs} + \int dE_\alpha\, \phi_\alpha^r(E_\alpha) P_{ei}^{\odot} P_i^{\text{conv}} \text{Br}_{ij}^{rs} P_{j\beta}^{\oplus s} \delta\left(E_\alpha - E_\beta\right) , \tag{5.15}$$

and thus

$$\phi_\beta^s(E_\beta) = \phi_\beta^{s,\text{invis}}(E_\beta)\,\delta_{rs} + \phi_\alpha^r(E_\beta) P_{ei}^{\odot} P_i^{\text{conv}} \text{Br}_{ij}^{rs} P_{j\beta}^{\oplus s} , \tag{5.16}$$

where, as before, $P^{\odot}_{ek}$ is the probability of the produced ν_e be found as a ν_k at the surface of the Sun, $P^{\oplus}_{k\beta}$ is the probability of a ν_k be detected as a ν_β on Earth, and P^{conv}_i is the transition probability of an eigenstate i into an eigenstate j upon propagating the Sun-Earth distance L. Finally, the branching fractions Br^{rs}_{ij} are given in Equations (3.46) – (3.48) for the three particular cases for the coupling constants in the quasi-degenerate scenario. As it can be seen from Equations (3.46) – (3.48), in the quasi-degenerate scenario, as $\delta \to 1$, only the pure pseudo-scalar case will produce non-vanishing antineutrino fluxes.

Now, for analysing the more general case of $0 < \delta < 1$, it is necessary to take into account the best currently available information on the neutrino masses, which is limited to the mass-squared differences and to constraints to the sum of neutrino masses:

$$\sum m_i = m_1 + m_2 + m_3\,. \tag{5.17}$$

The sum of neutrino masses can be written as a function of the lightest mass eigenstate and the mass-squared differences. As such, for the normal hierarchy (NH):

$$\left(\sum m_i\right)^{\mathrm{NH}} = m_1 + \sqrt{m_1^2 + \Delta m_{21}^2} + \sqrt{m_1^2 + \Delta m_{31}^2}\,, \tag{5.18}$$

and for the inverted hierarchy (IH):

$$\left(\sum m_i\right)^{\mathrm{IH}} = \sqrt{m_3^2 - (\Delta m_{32}^2 + \Delta m_{21}^2)} + \sqrt{m_3^2 - \Delta m_{32}^2} + m_3\,. \tag{5.19}$$

Neutrino oscillations imply that neutrino masses are non-degenerate and at least two of the mass eigenstates are massive. Hence, by supposing that the lightest mass eigenstate's mass in each hierarchy is null, it is possible to obtain a lower bound to the sum of neutrino masses. As such, for the normal hierarchy (NH):

$$\left(\sum m_i\right)^{\mathrm{NH}}_{\mathrm{min}} \geq \sqrt{\Delta m_{21}^2} + \sqrt{\Delta m_{31}^2} \approx 0.06\,\mathrm{eV}\,, \tag{5.20}$$

and for the inverted hierarchy (IH):

$$\left(\sum m_i\right)^{\mathrm{IH}}_{\mathrm{min}} \geq \sqrt{-\Delta m_{32}^2 - \Delta m_{21}^2} + \sqrt{-\Delta m_{32}^2} \approx 0.1\,\mathrm{eV}\,, \tag{5.21}$$

with the mass-squared differences taken at their best-fit values [59], as shown on Table 2.1.

On the other hand, upper bounds to the sum of neutrino masses can be obtained from the analysis of cosmological data. Massive neutrinos thermally produced during the Big Bang — forming today the so-called cosmological neutrino background (CνB) — are expected to impact the anisotropies in the cosmological microwave background (CMB) and large-scale structure formation [133]. Consequently, the 2018 results from the Planck Collaboration [134] set a cosmological upper bound to the sum of neutrino masses at

$$\left(\sum m_i\right)_{\rm max} \leq 0.12\,\mathrm{eV}\,, \quad \text{at } 95\% \text{ C.L.}\,. \tag{5.22}$$

It has been recently argued [135, 136] that this cosmological upper bound may be relaxed if neutrinos are unstable. However, to avoid conflict with well know cosmological parameters, the neutrino lifetime must be such that CνB neutrinos decay well after they become already non-relativistic. This requires lifetimes much larger than the current limits established from neutrino experiments. As such, we take the upper bound in Equation (5.22) as reported.

Now, using the upper and lower limits to the sum of neutrino masses and the mass-squared differences at their best-fit values [59], it is possible to calculate upper and lower limits to δ for each decay channel and each mass hierarchy under analysis.

First, consider the decay channel $\nu_2 \to \nu_1/\bar{\nu}_1$ in the normal hierarchy, for which $\delta_{21}^{\rm NH} = m_1/m_2$. In this hierarchy, since ν_1 is the lightest mass eigenstate, assuming $m_1 = 0$ leads to the lower limit $\delta_{21}^{\rm NH} \geq 0$. On the other hand, the upper limit to $\delta_{21}^{\rm NH}$ is obtained by solving the system:

$$\begin{cases} m_1 + m_2 + m_3 = \left(\sum m_i\right)_{\rm max} \\ m_2^2 - m_1^2 = \Delta m_{21}^2 \\ m_3^2 - m_1^2 = \Delta m_{31}^2 \end{cases} \tag{5.23}$$

for m_1, m_2 and m_3, with the mass-squared differences taken at their best-fit values [59], from which we obtain an upper limit $\delta_{21}^{\rm NH} \leq 0.96$. Hence, for the decay channel $\nu_2 \to \nu_1/\bar{\nu}_1$ in the normal hierarchy:

$$0 \leq \delta_{21}^{\rm NH} \leq 0.96\,. \tag{5.24}$$

For comparison, Planck's previous upper bound [137] at $\sum m_i < 0.23\,\mathrm{eV}$ (at 95% C.L.) implies that $\delta \approx 0.99$. Hence, as the limit on the sum of neutrino masses gets tighter, $\delta \approx 1$ becomes prohibited, and lower values of delta are favored.

Next, consider the decay channel $\nu_2 \to \nu_1/\bar{\nu}_1$ in the inverted hierarchy, for which $\delta_{21}^{\rm IH} = m_1/m_2$. In this decay channel, both m_1 and m_2 mass eigenstates are massive, but with a small mass squared difference. By making $m_3 = 0$, we have that $m_1 = \sqrt{-\Delta m_{32}^2 - \Delta m_{21}^2}$ and $m_2 = \sqrt{-\Delta m_{32}^2}$. Hence, the lower limit to $\delta_{21}^{\rm IH}$ is

$$\delta_{21}^{\rm IH} \geq \sqrt{\frac{\Delta m_{32}^2 + \Delta m_{21}^2}{\Delta m_{32}^2}} \approx 0.985\,, \tag{5.25}$$

with the mass-squared differences taken at their best-fit values [59]. On the other hand, the upper limit to $\delta_{21}^{\rm IH}$ is obtained by solving a system similar to Equation (5.23), with the adequate substitutions for the mass-squared differences, from which we obtain an upper limit

$\delta_{21}^{\mathrm{IH}} \leq 0.987$. Hence, for the decay channel $\nu_2 \to \nu_1/\bar{\nu}_1$ in the inverted hierarchy:

$$0.985 \leq \delta_{21}^{\mathrm{IH}} \leq 0.987\,. \tag{5.26}$$

Finally, consider the decay channel $\nu_2 \to \nu_3/\bar{\nu}_3$ in the inverted hierarchy, for which $\delta_{23}^{\mathrm{IH}} = m_3/m_2$. In this hierarchy, since ν_3 is the lightest mass eigenstate, assuming $m_3 = 0$ leads to the lower limit $\delta_{23}^{\mathrm{IH}} \geq 0$. On the other hand, the upper limit to $\delta_{23}^{\mathrm{IH}}$ is obtained by solving a system similar to Equation (5.23), with the adequate substitutions for the mass-squared differences, from which we obtain an upper limit $\delta_{23}^{\mathrm{IH}} \leq 0.3$. Hence, for the decay channel $\nu_2 \to \nu_3/\bar{\nu}_3$ in the inverted hierarchy:

$$0 \leq \delta_{23}^{\mathrm{IH}} \leq 0.3\,. \tag{5.27}$$

The range of allowed values of δ for each decay channel and each mass hierarchy will help us determine the lower limits to neutrino lifetime in the following sections.

5.3 Neutrino Fluxes Produced on Decay in Three Neutrino Families

In the context of neutrino visible decay it is also useful to separate the neutrino and antineutrino fluxes for three neutrino families into electronic and non-electronic flavors.

First, we can write the evolution equation for the flavor states in a general form:

$$i\frac{d}{dt}\begin{pmatrix} \nu \\ \bar{\nu} \end{pmatrix} = \left[\underline{\mathbf{U}}\left(\underline{\mathbf{M}}^2 - i\underline{\mathbf{D}}\right)\underline{\mathbf{U}}^\dagger + \underline{\mathbf{V}}\right]\begin{pmatrix} \nu \\ \bar{\nu} \end{pmatrix}, \tag{5.28}$$

where each of the underlined matrices are given by $\underline{\mathbf{A}} = \mathbf{diag}\left(\mathbf{A}_\nu, \mathbf{A}_{\bar{\nu}}\right)$ except for $\underline{\mathbf{D}}$. As before, $\mathbf{U}$ is the PMNS mixing matrix, $\mathbf{M}^2$ is the mass-squared difference matrix and $\mathbf{V}$ is the matrix describing matter effects.

The matrix $\underline{\mathbf{D}}$ describes the coupling between neutrinos and antineutrinos due to decay, and is given in general as

$$\underline{\mathbf{D}} = \begin{pmatrix} \mathbf{D}^{rr} & \mathbf{D}^{r'r} \\ \mathbf{D}^{rr'} & \mathbf{D}^{r'r'} \end{pmatrix}, \tag{5.29}$$

where each submatrix $\mathbf{D}^{rs}$ describes $\nu^r \to \nu^s$ and are given in three neutrino families as

$$\mathbf{D}^{rs} = \begin{pmatrix} d_{11}^{rs} & d_{21}^{rs} & d_{31}^{rs} \\ d_{12}^{rs} & d_{22}^{rs} & d_{32}^{rs} \\ d_{13}^{rs} & d_{23}^{rs} & d_{33}^{rs} \end{pmatrix}, \tag{5.30}$$

where each element $\mathbf{D}_{ji}^{rs} = \mathbf{d}_{ij}^{rs}$ describes $\nu_i^r \to \nu_j^s$. Hence, elements d_{ii}^{ss} describe the survival of ν_i^s neutrino mass eigenstates, while all other elements describe conversions between mass eigenstates. Additionally, in the decay model under consideration, transitions $\nu_i^r \to \nu_i^{r'}$ are not allowed and the matrices $\mathbf{D}^{r'r}$ and $\mathbf{D}^{rr'}$ diagonal elements are null, while elements d_{ij}^{rs} are null if $m_i \leq m_j$.

As before, a rotation in the basis can be made by multiplying both sides by $\underline{\mathbf{R}}_{13}^\dagger \underline{\mathbf{R}}_{23}^\dagger$ on the left, and using the relation $\underline{\mathbf{R}}_{23}\underline{\mathbf{R}}_{13}\underline{\mathbf{R}}_{13}^\dagger\underline{\mathbf{R}}_{23}^\dagger = \mathbf{I}$ in Equation (5.28). Hence, it can be rewritten as

$$i\frac{d}{dt}\begin{pmatrix} \nu' \\ \bar{\nu}' \end{pmatrix} = \left[\underline{\mathbf{R}}_{12}\left(\underline{\mathbf{M}}^2 - i\underline{\mathbf{D}}\right)\underline{\mathbf{R}}_{12}^\dagger + \underline{\mathbf{R}}_{13}^\dagger\underline{\mathbf{R}}_{23}^\dagger\underline{\mathbf{V}}\underline{\mathbf{R}}_{23}\underline{\mathbf{R}}_{13}\right]\begin{pmatrix} \nu' \\ \bar{\nu}' \end{pmatrix}. \tag{5.31}$$

Now, it is necessary evaluate how each mass hierarchy, and consequently how each decay channel, affects the evolution of neutrino states.

5.3.1 Normal Hierarchy

First, we consider the decay channel $\nu_2/\bar{\nu}_2 \to \nu_1/\bar{\nu}_1$ in the normal hierarchy. As such, the elements of matrix $\underline{\mathbf{D}}$ are given by

$$\mathbf{D}^{\nu\nu} = \begin{pmatrix} 0 & d_{21} & 0 \\ 0 & d_{22} & 0 \\ 0 & 0 & 0 \end{pmatrix}, \quad \mathbf{D}^{\nu\bar{\nu}} = \begin{pmatrix} 0 & d_{2\bar{1}} & 0 \\ 0 & 0 & 0 \\ 0 & 0 & 0 \end{pmatrix}, \tag{5.32}$$

and similarly for $\mathbf{D}^{\bar{\nu}\nu}$ and $\mathbf{D}^{\bar{\nu}\bar{\nu}}$. As such, from Equation (5.31), the rotated matrix $\underline{\mathbf{D}}' = \underline{\mathbf{R}}_{12}\underline{\mathbf{D}}\underline{\mathbf{R}}_{12}^\dagger$ becomes

$$\underline{\mathbf{D}}' = \left(\begin{array}{ccc|ccc} d'_{ee} & d'_{\mu e} & 0 & d'_{\bar{e}e} & d'_{\bar{\mu}e} & 0 \\ d'_{e\mu} & d'_{\mu\mu} & 0 & d'_{\bar{e}\mu} & d'_{\bar{\mu}\mu} & 0 \\ 0 & 0 & 0 & 0 & 0 & 0 \\ \hline d'_{e\bar{e}} & d'_{\mu\bar{e}} & 0 & d'_{\bar{e}\bar{e}} & d'_{\bar{\mu}\bar{e}} & 0 \\ d'_{e\bar{\mu}} & d'_{\mu\bar{\mu}} & 0 & d'_{\bar{e}\bar{\mu}} & d'_{\bar{\mu}\bar{\mu}} & 0 \\ 0 & 0 & 0 & 0 & 0 & 0 \end{array}\right), \tag{5.33}$$

where the diagonal submatrices' elements contain terms describing mass-eigenstates' survival and the conversion, while the antidiagonal submatrices' elements only contain terms describing mass-eigenstates' conversion.

Hence, from Equation (5.31), the time-dependent matrix $\mathbf{S}'$ describing the evolution of the primed states, under the same assumptions used for Equation (2.58), is given by

$$\begin{pmatrix} \nu'_e(t) \\ \nu'_\mu(t) \\ \nu'_\tau(t) \\ \bar{\nu}'_e(t) \\ \bar{\nu}'_\mu(t) \\ \bar{\nu}'_\tau(t) \end{pmatrix} = \left(\begin{array}{ccc|ccc} S'_{ee} & S'_{\mu e} & 0 & S'_{\bar{e}e} & S'_{\bar{\mu}e} & 0 \\ S'_{e\mu} & S'_{\mu\mu} & 0 & S'_{\bar{e}\mu} & S'_{\bar{\mu}\mu} & 0 \\ 0 & 0 & S'_{\tau\tau} & 0 & 0 & 0 \\ \hline S'_{e\bar{e}} & S'_{\mu\bar{e}} & 0 & S'_{\bar{e}\bar{e}} & S'_{\bar{\mu}\bar{e}} & 0 \\ S'_{e\bar{\mu}} & S'_{\mu\bar{\mu}} & 0 & S'_{\bar{e}\bar{\mu}} & S'_{\bar{\mu}\bar{\mu}} & 0 \\ 0 & 0 & 0 & 0 & 0 & S'_{\bar{\tau}\bar{\tau}} \end{array}\right) \begin{pmatrix} \nu'_e(0) \\ \nu'_\mu(0) \\ \nu'_\tau(0) \\ \bar{\nu}'_e(0) \\ \bar{\nu}'_\mu(0) \\ \bar{\nu}'_\tau(0) \end{pmatrix}, \tag{5.34}$$

which we can transform back into the unprimed basis by the transformation:

$$\mathbf{S} = \underline{\mathbf{R}}_{23}\,\underline{\mathbf{R}}_{13}\,\mathbf{S}'\,\underline{\mathbf{R}}_{13}^{\dagger}\,\underline{\mathbf{R}}_{23}^{\dagger}\,. \tag{5.35}$$

The survival and transition probabilities into neutrinos are

$$P_{ee} = |\langle \nu_e(t)|\mathbf{S}|\nu_e(0)\rangle|^2 = |S_{ee}|^2\,, \tag{5.36}$$

$$P_{e\mu} + P_{e\tau} = |\langle \nu_\mu(t)|\mathbf{S}|\nu_e(0)\rangle|^2 + |\langle \nu_\tau(t)|\mathbf{S}|\nu_e(0)\rangle|^2 = |S_{e\mu}|^2 + |S_{e\tau}|^2\,, \tag{5.37}$$

while the transition probabilities into antineutrinos are given by

$$P_{e\bar{e}} = |\langle \bar{\nu}_e(t)|\mathbf{S}|\nu_e(0)\rangle|^2 = |S_{e\bar{e}}|^2\,, \tag{5.38}$$

$$P_{e\bar{\mu}} + P_{e\bar{\tau}} = |\langle \bar{\nu}_\mu(t)|\mathbf{S}|\nu_e(0)\rangle|^2 + |\langle \bar{\nu}_\tau(t)|\mathbf{S}|\nu_e(0)\rangle|^2 = |S_{e\bar{\mu}}|^2 + |S_{e\bar{\tau}}|^2\,. \tag{5.39}$$

From Equation (5.35), we have:

$$S_{ee} = c_{13}^2 S'_{ee} + s_{13}^2 S'_{\tau\tau}\,, \tag{5.40}$$

$$S_{e\mu} = -c_{13}s_{13}s_{23}S'_{ee} + c_{13}c_{23}S'_{e\mu} + c_{13}s_{13}s_{23}S'_{\tau\tau}\,, \tag{5.41}$$

$$S_{e\tau} = -c_{13}c_{23}s_{13}S'_{ee} - c_{13}s_{23}S'_{e\mu} + c_{13}s_{13}c_{23}S'_{\tau\tau}\,, \tag{5.42}$$

$$S_{e\bar{e}} = c_{13}^2 S'_{e\bar{e}}\,, \tag{5.43}$$

$$S_{e\bar{\mu}} = -c_{13}s_{13}s_{23}S'_{e\bar{e}} + c_{13}c_{23}S'_{e\bar{\mu}}\,, \tag{5.44}$$

$$S_{e\bar{\tau}} = -c_{13}s_{13}c_{23}S'_{e\bar{e}} - c_{13}s_{23}S'_{e\bar{\mu}}\,. \tag{5.45}$$

Once more neglecting the interference effects in Equations (5.36) to (5.39), and making

$|S'_{\tau\tau}|^2 = 1$, the survival and transition probabilities become

$$P_{ee} = c_{13}^4 P'_{ee} + s_{13}^4 , \tag{5.46}$$

$$P_{e(\mu+\tau)} = c_{13}^2 P'_{e\mu} + s_{13}^2 c_{13}^2 P'_{ee} + s_{13}^2 c_{13}^2 , \tag{5.47}$$

$$P_{e\bar{e}} = c_{13}^4 P'_{e\bar{e}} , \tag{5.48}$$

$$P_{e(\bar{\mu}+\bar{\tau})} = c_{13}^2 P'_{e\bar{\mu}} + s_{13}^2 c_{13}^2 P'_{e\bar{e}} , \tag{5.49}$$

where the primed probabilities are the survival and transition probabilities for two neutrino families. Now, to account for the energy shift in the neutrino spectrum due to visible decay, the probabilities are written as

$$\frac{dP_{ee}}{dE_\beta} = c_{13}^4 \frac{dP'_{ee}}{dE_\beta} + s_{13}^4 \delta\left(E_\alpha - E_\beta\right) , \tag{5.50}$$

$$\frac{dP_{e(\mu+\tau)}}{dE_\beta} = c_{13}^2 \frac{dP'_{e\mu}}{dE_\beta} + s_{13}^2 c_{13}^2 \frac{dP'_{ee}}{dE_\beta} + s_{13}^2 c_{13}^2 \delta\left(E_\alpha - E_\beta\right) , \tag{5.51}$$

$$\frac{dP_{e\bar{e}}}{dE_\beta} = c_{13}^4 \frac{dP'_{e\bar{e}}}{dE_\beta} , \tag{5.52}$$

$$\frac{dP_{e(\bar{\mu}+\bar{\tau})}}{dE_\beta} = c_{13}^2 \frac{dP'_{e\bar{\mu}}}{dE_\beta} + s_{13}^2 c_{13}^2 \frac{dP'_{e\bar{e}}}{dE_\beta} , \tag{5.53}$$

where the primed probabilities are the survival and transition probabilities for two neutrino families as defined on Equation (5.7). Hence, the solar neutrino and antineutrino fluxes arriving in the detector are finally given by Equation (3.72):

$$\Phi_\beta(E_\beta) = \int dE_\alpha \, \phi_e^0(E_\alpha) \frac{dP_{\alpha\beta}}{dE_\beta}(E_\alpha, E_\beta) , \tag{3.72}$$

which finally yields the three-family neutrino fluxes in the visible decay scenario for the decay channel $\nu_2/\bar{\nu}_2 \to \nu_1/\bar{\nu}_1$ in the normal hierarchy as

$$\Phi_e = c_{13}^4 \, \phi_e + s_{13}^4 \, \phi_e^0 , \tag{5.54}$$

$$\Phi_{(\mu+\tau)} = c_{13}^2 \, \phi_\mu + s_{13}^2 c_{13}^2 \, \phi_e + s_{13}^2 c_{13}^2 \, \phi_e^0 , \tag{5.55}$$

$$\Phi_{\bar{e}} = c_{13}^4 \, \phi_{\bar{e}} , \tag{5.56}$$

$$\Phi_{(\bar{\mu}+\bar{\tau})} = c_{13}^2 \, \phi_{\bar{\mu}} + s_{13}^2 c_{13}^2 \, \phi_{\bar{e}} , \tag{5.57}$$

where ϕ_e, $\phi_{\bar{e}}$, ϕ_μ, and $\phi_{\bar{\mu}}$ are the two-family oscillated neutrino fluxes modified by the visible decay as given by Equation (5.8), while ϕ_e^0 is the unoscillated neutrino flux.

5.3.2 Inverted Hierarchy

The evolution of neutrinos and antineutrinos in the inverted hierarchy for the decay channel $\nu_2/\bar{\nu}_2 \to \nu_1/\bar{\nu}_1$ is the same as in the normal hierarchy. Hence, Equations (5.54) to (5.57) obtained above are also valid for this case.

Now, for the decay channel $\nu_2/\bar{\nu}_2 \to \nu_3/\bar{\nu}_3$, the elements of matrix $\underline{\mathbf{D}}$ are given by

$$\mathbf{D}^{\nu\nu} = \begin{pmatrix} 0 & 0 & 0 \\ 0 & d_{22} & 0 \\ 0 & d_{23} & 0 \end{pmatrix}, \quad \mathbf{D}^{\nu\bar{\nu}} = \begin{pmatrix} 0 & 0 & 0 \\ 0 & 0 & 0 \\ 0 & d_{2\bar{3}} & 0 \end{pmatrix}, \tag{5.58}$$

and similarly for $\mathbf{D}^{\bar{\nu}\nu}$ and $\mathbf{D}^{\bar{\nu}\bar{\nu}}$. As such, from Equation (5.31), the rotated matrix $\underline{\mathbf{D}}' = \underline{\mathbf{R}}_{12}\underline{\mathbf{D}}\underline{\mathbf{R}}_{12}^{\dagger}$ becomes

$$\underline{\mathbf{D}}' = \left(\begin{array}{ccc|ccc} d'_{ee} & d'_{\mu e} & 0 & 0 & 0 & 0 \\ d'_{e\mu} & d'_{\mu\mu} & 0 & 0 & 0 & 0 \\ d'_{e\tau} & d'_{\mu\tau} & 0 & d'_{\bar{e}\tau} & d'_{\bar{\mu}\tau} & 0 \\ \hline 0 & 0 & 0 & d'_{\bar{e}\bar{e}} & d'_{\bar{\mu}\bar{e}} & 0 \\ 0 & 0 & 0 & d'_{\bar{e}\bar{\mu}} & d'_{\bar{\mu}\bar{\mu}} & 0 \\ d'_{e\bar{\tau}} & d'_{\mu\bar{\tau}} & 0 & d'_{\bar{e}\bar{\tau}} & d'_{\bar{\mu}\bar{\tau}} & 0 \end{array}\right), \tag{5.59}$$

where, once more, the diagonal submatrices' elements contain terms describing mass-eigenstates' survival and conversion, while the antidiagonal submatrices' elements only contain terms describing mass-eigenstates' conversion. In this case, however, the elements ${d'}^{rs}_{\alpha\tau}$, highlighted above in gray, contain only terms describing mass-eigenstates' conversion upon decay, while the other elements contain only terms describing mass-eigenstates' survival.

As such, from Equation (5.31), the time dependent matrix $\mathbf{S}'$ describing the evolution of the primed states, under the same assumptions used for Equation (2.58), is given by

$$\begin{pmatrix} \nu'_e(t) \\ \nu'_\mu(t) \\ \nu'_\tau(t) \\ \bar{\nu}'_e(t) \\ \bar{\nu}'_\mu(t) \\ \bar{\nu}'_\tau(t) \end{pmatrix} = \left(\begin{array}{ccc|ccc} S'_{ee} & S'_{\mu e} & 0 & 0 & 0 & 0 \\ S'_{e\mu} & S'_{\mu\mu} & 0 & 0 & 0 & 0 \\ S'_{e\tau} & S'_{\mu\tau} & S'_{\tau\tau} & S'_{\bar{e}\tau} & S'_{\bar{\mu}\tau} & 0 \\ \hline 0 & 0 & 0 & S'_{\bar{e}\bar{e}} & S'_{\bar{\mu}\bar{e}} & 0 \\ 0 & 0 & 0 & S'_{\bar{e}\bar{\mu}} & S'_{\bar{\mu}\bar{\mu}} & 0 \\ S'_{e\bar{\tau}} & S'_{\mu\bar{\tau}} & 0 & S'_{\bar{e}\bar{\tau}} & S'_{\bar{\mu}\bar{\tau}} & S'_{\bar{\tau}\bar{\tau}} \end{array}\right) \begin{pmatrix} \nu'_e(0) \\ \nu'_\mu(0) \\ \nu'_\tau(0) \\ \bar{\nu}'_e(0) \\ \bar{\nu}'_\mu(0) \\ \bar{\nu}'_\tau(0) \end{pmatrix}, \tag{5.60}$$

where the elements $S'_{e\tau}$ and $S'_{\mu\tau}$, highlighted above in gray, are the amplitudes for production of the eigenstate ${\nu'}^{s}_{\tau} = \nu^{s}_{3}$ upon decay, while the other elements are the amplitudes for the two-flavor oscillation and survival from decay, i.e., the invisible decay amplitudes. $\mathbf{S}'$ is again transformed back into the unprimed basis by the transformation in Equation (5.35), from which we have:

$$S_{ee} = c_{13}^2 S'_{ee} + s_{13}c_{13}S'_{e\tau} + s_{13}^2 S'_{\tau\tau}\,, \tag{5.61}$$
$$S_{e\mu} = -c_{13}s_{13}s_{23}S'_{ee} + c_{13}c_{23}S'_{e\mu} + c_{13}^2 s_{23}S'_{e\tau} + c_{13}s_{13}s_{23}S'_{\tau\tau}\,, \tag{5.62}$$
$$S_{e\tau} = -c_{13}s_{13}c_{23}S'_{ee} - c_{13}s_{23}S'_{e\mu} + c_{13}^2 c_{23}S'_{e\tau} + c_{13}s_{13}c_{23}S'_{\tau\tau}\,, \tag{5.63}$$
$$S_{e\bar{e}} = c_{13}s_{13}S'_{e\bar{\tau}}\,, \tag{5.64}$$
$$S_{e\bar{\mu}} = c_{13}^2 s_{23}S'_{e\bar{\tau}}\,, \tag{5.65}$$
$$S_{e\bar{\tau}} = c_{13}^2 c_{23}S'_{e\bar{\tau}}\,. \tag{5.66}$$

The survival and transition probabilities into neutrinos are given as in Equations (5.36) to (5.39):

$$P_{ee} = c_{13}^4 P'_{ee} + s_{13}^4 + c_{13}^2 s_{13}^2 P_{e3}\,, \tag{5.67}$$
$$P_{e(\mu+\tau)} = c_{13}^2 s_{13}^2 P'_{ee} + c_{13}^2 P'_{e\mu} + c_{13}^2 s_{13}^2 + c_{13}^4 P_{e3}\,, \tag{5.68}$$
$$P_{e\bar{e}} = c_{13}^2 s_{13}^2 P_{e\bar{3}}\,, \tag{5.69}$$
$$P_{e(\bar{\mu}+\bar{\tau})} = c_{13}^4 P_{e\bar{3}}\,. \tag{5.70}$$

where $P_{e3} = |S'_{e\tau}|^2$ and $P_{e\bar{3}} = |S'_{e\bar{\tau}}|^2$ are the probabilities for the production of ν_3 and $\bar{\nu}_3$ upon the decay of the ν_2 mass-eigenstate content in the ν_e solar neutrinos. The primed probabilities are the survival and transition probabilities for the invisible decay of the ν_2 in two neutrino families, following the discussion above regarding the amplitudes, and are given in Equations (4.4) and (4.5), Consequently:.

$$P_{ee} = P_{ee}^{\mathrm{inv}} + c_{13}^2 s_{13}^2 P_{e3}\,, \tag{5.71}$$
$$P_{e(\mu+\tau)} = P_{e(\mu+\tau)}^{\mathrm{inv}} + c_{13}^4 P_{e3}\,, \tag{5.72}$$
$$P_{e\bar{e}} = c_{13}^2 s_{13}^2 P_{e\bar{3}}\,, \tag{5.73}$$
$$P_{e(\bar{\mu}+\bar{\tau})} = c_{13}^4 P_{e\bar{3}}\,. \tag{5.74}$$

Now, to account for the energy shift in the neutrino spectrum due to visible decay, the probabilities are written as

$$\frac{dP_{ee}}{dE_\beta} = P_{ee}^{\mathrm{inv}}\delta\left(E_\alpha - E_\beta\right) + c_{13}^2 s_{13}^2 \frac{dP'_{e3}}{dE_\beta}\,, \tag{5.75}$$
$$\frac{dP_{e(\mu+\tau)}}{dE_\alpha} = P_{e(\mu+\tau)}^{\mathrm{inv}}\delta\left(E_\alpha - E_\beta\right) + c_{13}^4 \frac{dP'_{e3}}{dE_\beta}\,, \tag{5.76}$$
$$\frac{dP_{e\bar{e}}}{dE_\alpha} = c_{13}^2 s_{13}^2 \frac{dP'_{e3}}{dE_\beta}\,, \tag{5.77}$$
$$\frac{dP_{e(\bar{\mu}+\bar{\tau})}}{dE_\beta} = c_{13}^4 \frac{dP'_{e3}}{dE_\beta}\,. \tag{5.78}$$

where P_{ee}^{inv} and $P_{e(\mu+\tau)}^{\text{inv}}$ are the three-family survival and transition probabilities in the invisible decay scenario as given by Equations (4.6) and (4.7), and dP'_{e3}/dE_β from Equation (5.7) as

$$\frac{dP'_{e3}}{dE_\beta} = P_{e2}^{\odot} P_{23} w_{23}^{rs} \,. \tag{5.79}$$

where $P_{e2}^{\odot}$ is the probability of the produced ν_e be found as a ν_2 at the surface of the Sun, P_{23} is the transition probability of the eigenstate ν_2 into an eigenstate ν_3 upon propagating the Sun-Earth distance L, and w_{23}^{rs} is the weighted differential decay width given in Equations (3.29) and (3.30). Hence, the solar neutrino and antineutrino fluxes arriving in the detector are finally given by Equation (3.72):

$$\Phi_\beta(E_\beta) = \int dE_\alpha \, \phi_e^0(E_\alpha) \frac{dP_{\alpha\beta}}{dE_\beta}(E_\alpha, E_\beta) \,, \tag{3.72}$$

which finally yields the three-family neutrino fluxes in the visible decay scenario for the decay channel $\nu_2/\bar{\nu}_2 \to \nu_3/\bar{\nu}_3$ in the inverted hierarchy as

$$\Phi_e = \Phi_e^{\text{inv}} + c_{13}^2 s_{13}^2 \, \phi_3 \,, \tag{5.80}$$

$$\Phi_{(\mu+\tau)} = \Phi_{(\mu+\tau)}^{\text{inv}} + c_{13}^4 \, \phi_3 \,, \tag{5.81}$$

$$\Phi_{\bar{e}} = c_{13}^2 s_{13}^2 \, \phi_{\bar{3}} \,, \tag{5.82}$$

$$\Phi_{(\bar{\mu}+\bar{\tau})} = c_{13}^4 \, \phi_{\bar{3}} \,, \tag{5.83}$$

where Φ_e^{inv} and $\Phi_{(\mu+\tau)}^{\text{inv}}$ are the three-family invisible decay fluxes and ϕ_3 and $\phi_{\bar{3}}$ are given by

$$\phi_3^s(E_\beta) = \int dE_\alpha \, \phi_e^0 P_{e2}^{\odot} P_{23} w_{23}^{rs} \,. \tag{5.84}$$

Figures 5.2 – 5.5 show neutrino and antineutrino fluxes produced in the visible decay of the ^{8}B solar neutrinos for selected values of τ_2/m_2 and δ, and for each case of the coupling constants, in the context of three neutrino families.

Figure 5.2 accounts for the hierarchical mass scenario, that is, $\delta = 0$, for the decay channel $\nu_2 \to \nu_1/\bar{\nu}_1$ (in both normal and inverted hierarchy) and for the decay channel $\nu_2 \to \nu_3/\bar{\nu}_3$ (in the inverted hierarchy).

Figures 5.3 – 5.5 accounts for values of δ close to the upper limit allowed in each decay channel and mass hierarchy, as discussed in Section 5.2. Figures 5.3 and 5.4 show the results for the decay channel $\nu_2 \to \nu_1/\bar{\nu}_1$ (in both normal and inverted hierarchy). Figure 5.5 shows the results for the decay channel $\nu_2 \to \nu_3/\bar{\nu}_3$ (in the inverted hierarchy).

As it can be seen in Figures 5.2 and 5.5, for small values of δ, daughter neutrinos can be produced in a much lower energy than their mother particle, which, combined with the overall suppression of decay at higher energies, causes very few antineutrinos to be produced at higher energies.

On the other hand, as it can be seen in Figures 5.3 and 5.4, for $\delta \approx 1$, daughter neutrinos are produced at roughly the same energy as their mother particle. As such, neutrino and antineutrino fluxes follow a similar shape. For increasing values of δ, the behavior of the antineutrino fluxes depends on the dominant coupling constant, as discussed in Section 3.1.

At any case, increasing the neutrino lifetime leads to the smaller antineutrino production. *In the next sections, these theoretical antineutrino fluxes obtained above are compared to experimental upper limits to antineutrinos of solar origin in order to set limits to the neutrino lifetime.*

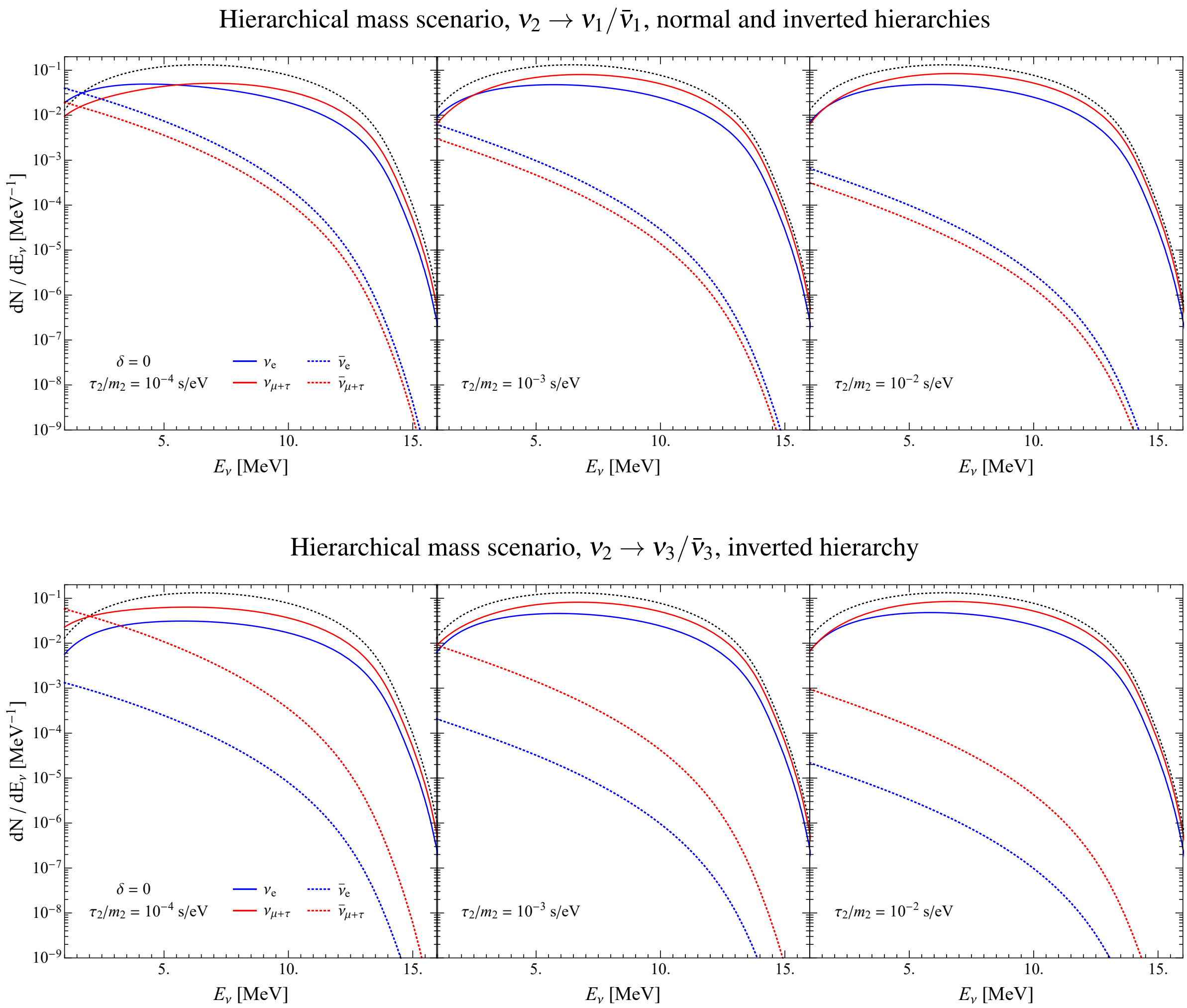

Figure 5.2: Expected normalized neutrino and antineutrino energy spectra resultant from the visible decay of the ^{8}B solar neutrinos in the hierarchical mass scenario, for the decay channel $\nu_2 \to \nu_1/\bar{\nu}_1$ in both normal and inverted hierarchies and $\nu_2 \to \nu_3/\bar{\nu}_3$ in the inverted hierarchy for different values of the neutrino lifetime τ_2/m_2, in the context of three neutrino families. Blue and red curves represent ν_e and $\nu_{\mu+\tau}$ neutrinos respectively, while solid lines neutrinos and dotted lines represent antineutrinos. The black dotted line represents the unoscillated ^{8}B neutrino flux. Best-fit values for the global fit neutrino oscillation parameters [59] as shown on Table 2.1 are used.

(a) Scalar case, $\nu_2 \to \nu_1/\bar{\nu}_1$, normal and inverted hierarchies

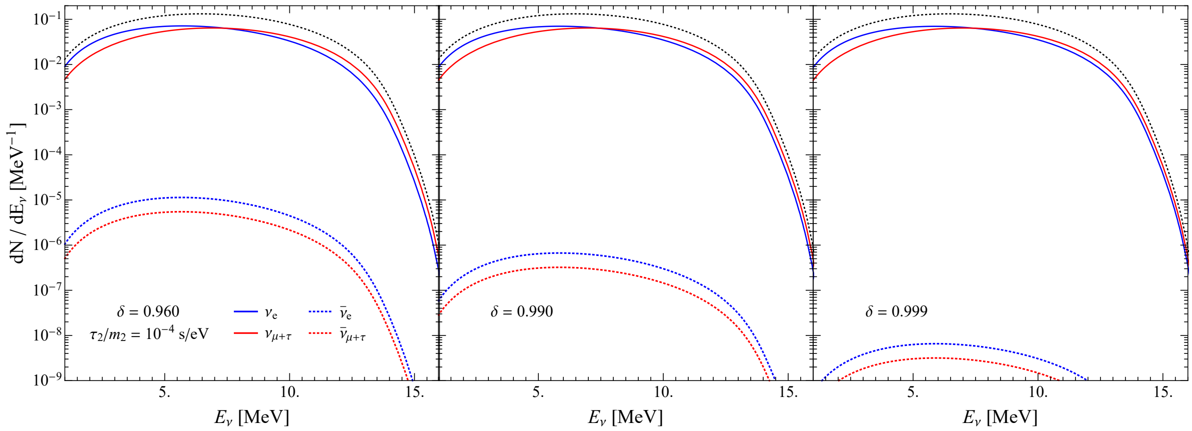

(b) Democratic case, $\nu_2 \to \nu_1/\bar{\nu}_1$, normal and inverted hierarchies

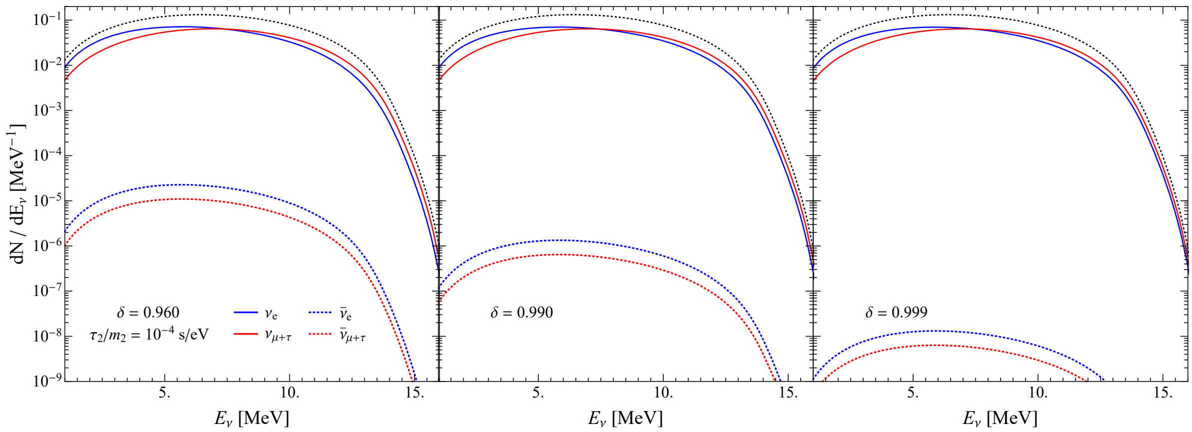

(c) Pseudo-scalar case, $\nu_2 \to \nu_1/\bar{\nu}_1$, normal and inverted hierarchies

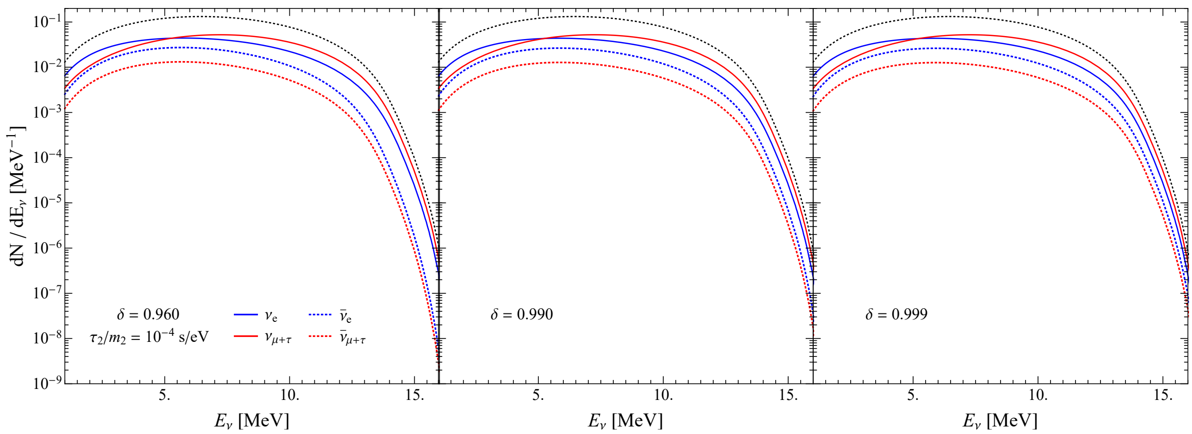

Figure 5.3: Expected normalized neutrino and antineutrino energy spectra resultant from the visible decay of the ^{8}B neutrinos produced in the Sun, for the decay channel $\nu_2 \to \nu_1/\bar{\nu}_1$ in both normal and inverted hierarchy, for $\tau_2/m_2 = 1 \times 10^{-4}\,\mathrm{s}\cdot\mathrm{eV}^{-1}$ and $\delta = 0.960$ (left), 0.990 (center) and 0.999 (right), for each of the coupling constant cases, in the context of three neutrino families. Blue and red curves represent ν_e and $\nu_{\mu+\tau}$ neutrinos respectively, while solid lines neutrinos and dotted lines represent antineutrinos. The black dotted line represents the unoscillated ^{8}B neutrino flux. Best-fit values for the global fit neutrino oscillation parameters [59] as shown on Table 2.1 are used.

(a) Scalar case, $\nu_2 \to \nu_1/\bar{\nu}_1$, normal and inverted hierarchies

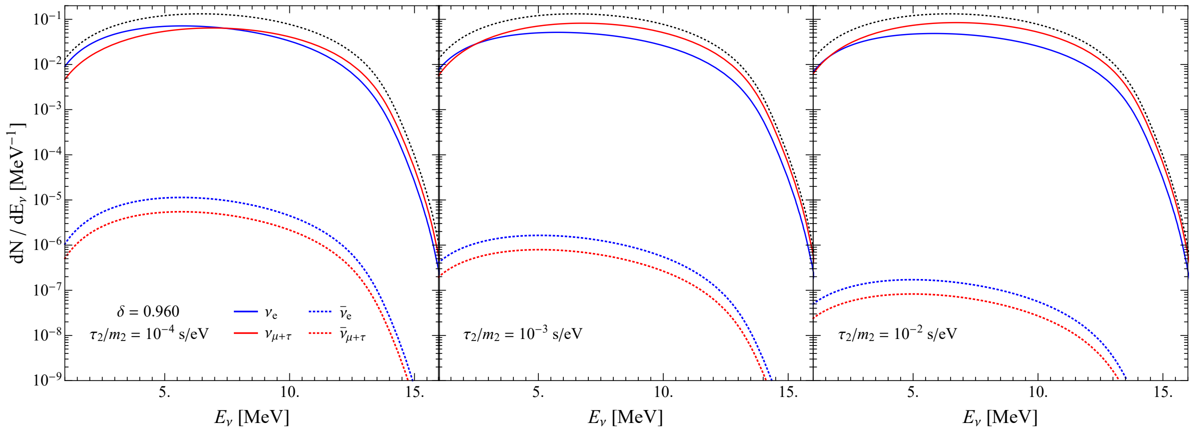

(b) Democratic case, $\nu_2 \to \nu_1/\bar{\nu}_1$, normal and inverted hierarchies

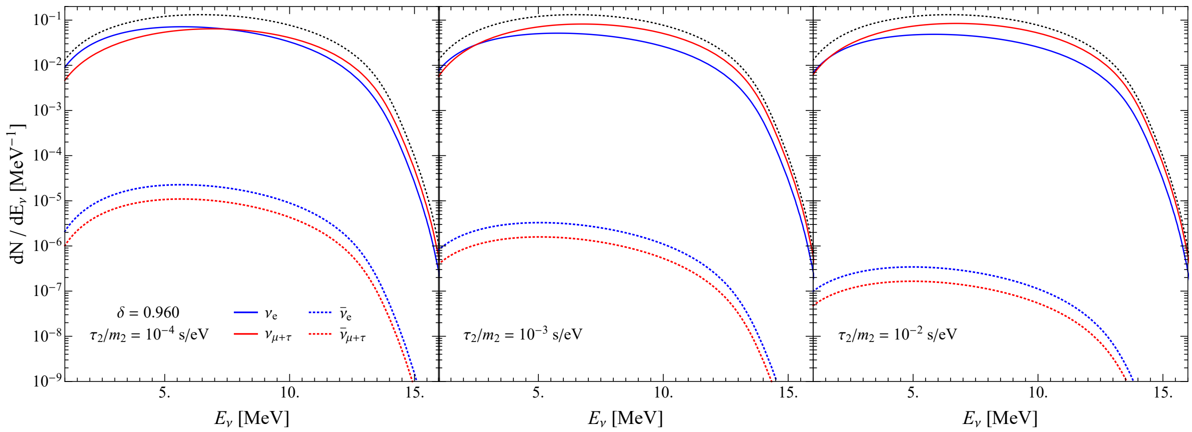

(c) Pseudo-scalar Case, $\nu_2 \to \nu_1/\bar{\nu}_1$, normal and inverted hierarchies

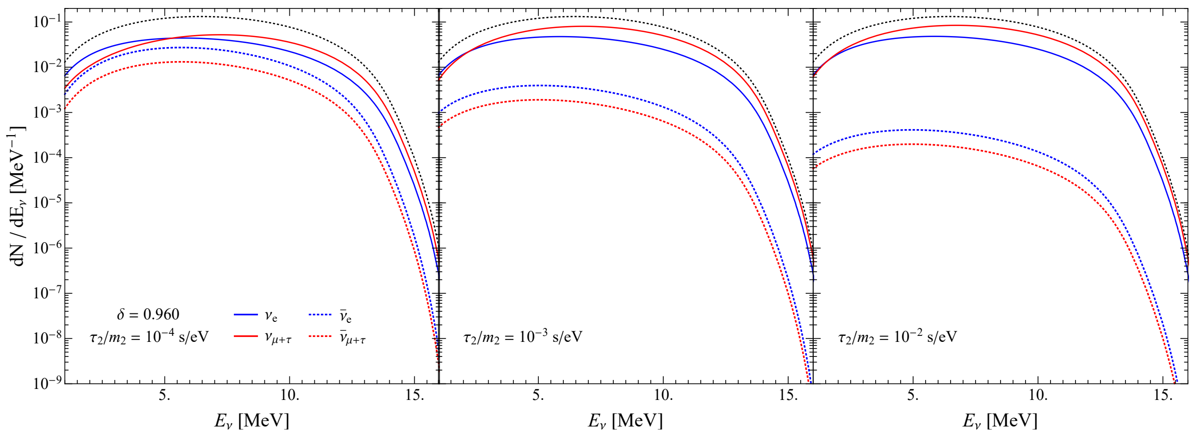

Figure 5.4: Expected normalized neutrino and antineutrino energy spectra resultant from the visible decay of the ^{8}B neutrinos produced in the Sun, for the decay channel $\nu_2 \to \nu_1/\bar{\nu}_1$ in both normal and inverted hierarchy, for $\delta = 0.96$ and $\tau_2/m_2 = 1\times10^{-4}\,\mathrm{s}\cdot\mathrm{eV}^{-1}$ (left), $1\times10^{-3}\,\mathrm{s}\cdot\mathrm{eV}^{-1}$ (center) and $1\times10^{-2}\,\mathrm{s}\cdot\mathrm{eV}^{-1}$ (right), for each of the coupling constant cases, in the context of three neutrino families. Blue and red curves represent ν_e and $\nu_{\mu+\tau}$ neutrinos respectively, while solid lines neutrinos and dotted lines represent antineutrinos. The black dotted line represents the unoscillated ^{8}B neutrino flux. Best-fit values for the global fit neutrino oscillation parameters [59] as shown on Table 2.1 are used.

(a) Scalar case, $\nu_2 \to \nu_3/\bar{\nu}_3$, inverted hierarchy

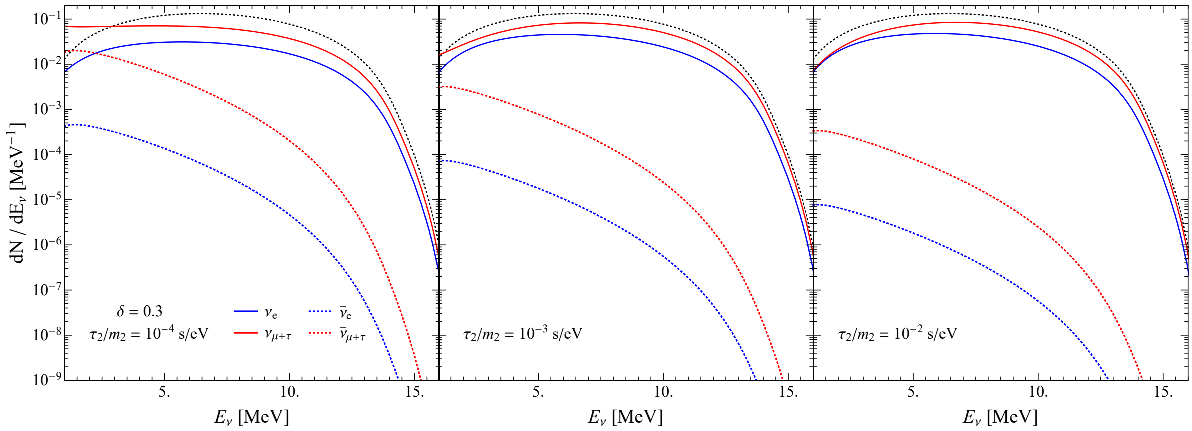

(b) Democratic case, $\nu_2 \to \nu_3/\bar{\nu}_3$, inverted hierarchy

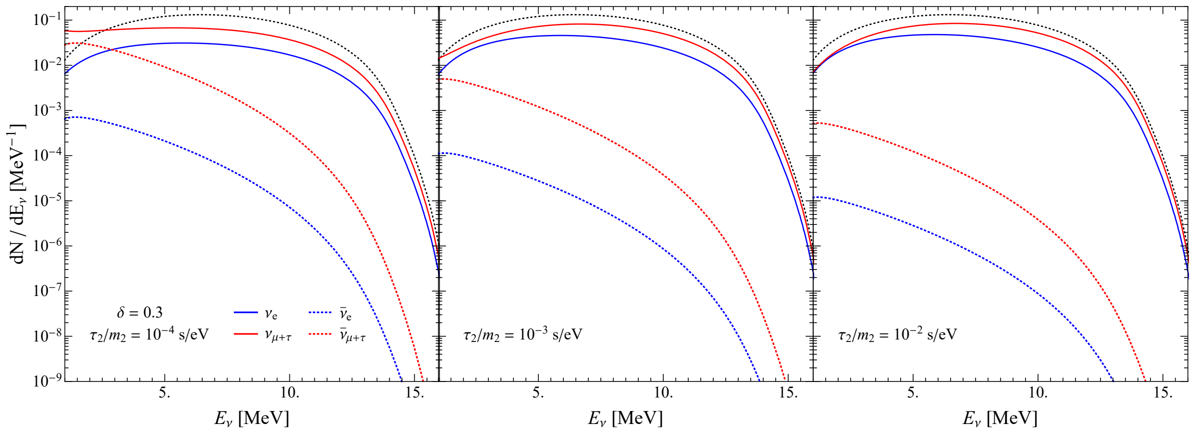

(c) Pseudo-scalar case, $\nu_2 \to \nu_3/\bar{\nu}_3$, inverted hierarchy

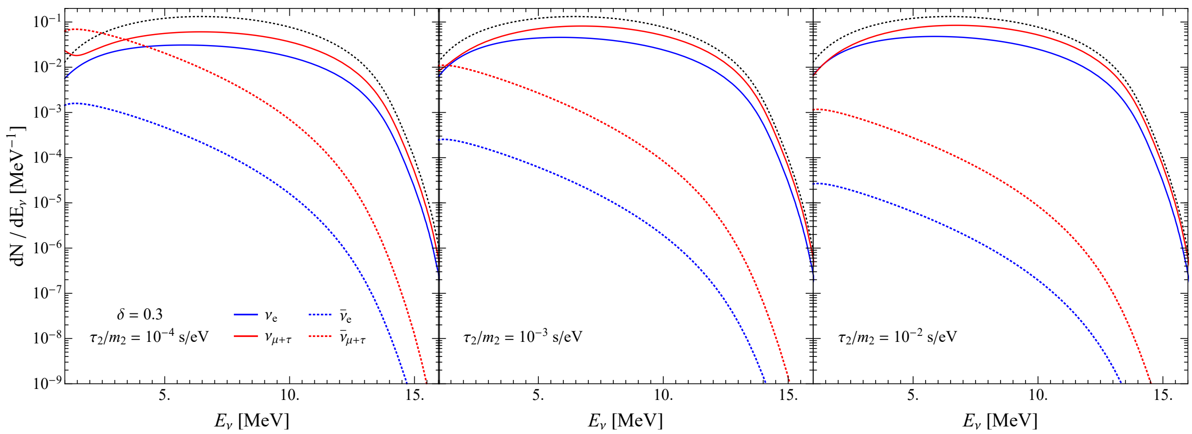

Figure 5.5: Expected normalized neutrino and antineutrino energy spectra resultant from the visible decay of the ^{8}B neutrinos produced in the Sun, for the decay channel $\nu_2 \to \nu_3/\bar{\nu}_3$ in the inverted hierarchy, for $\delta = 0.3$ and $\tau_2/m_2 = 1\times10^{-4}\,\mathrm{s\cdot eV^{-1}}$ (left), $1\times10^{-3}\,\mathrm{s\cdot eV^{-1}}$ (center) and $1\times10^{-2}\,\mathrm{s\cdot eV^{-1}}$ (right), for each of the coupling constant cases, in the context of three neutrino families. Blue and red curves represent ν_e and $\nu_{\mu+\tau}$ neutrinos respectively, while solid lines neutrinos and dotted lines represent antineutrinos. The black dotted line represents the unoscillated ^{8}B neutrino flux. Best-fit values for the global fit neutrino oscillation parameters [59] as shown on Table 2.1 are used.

5.4 Experimental Limits to Solar Antineutrinos

Solar neutrino experiments can probe and set upper limits to antineutrinos originating in the Sun.

In water Cherenkov experiments neutrinos are detected through the Cherenkov light emitted by elastically scattered electrons ($\nu + e^- \rightarrow \nu + e^-$). Similarly, liquid scintillation experiments also detect neutrinos through elastically scattered electrons. However, these electrons excite atoms and molecules on their path, which produce radiation upon de-excitation providing the signal for measuring the neutrino's energy and direction.

In either case, antineutrinos may also be detected by the Inverse Beta Decay (IBD) process ($\bar{\nu}_e + p \rightarrow e^+ + n$). The positron in this reaction deposits its energy in the medium and is promptly annihilated into two photons, while the neutron is captured by a proton in the medium producing a delayed 2.2 MeV photon. The detection of both signals in a delayed coincidence is the signal for this antineutrino interaction [103, 138–141]. As such, other antineutrino sources are backgrounds for this reaction, such as antineutrinos produced by the decay of Earth's radioactive isotopes, part of the so-called geo-neutrinos, up to 3.26 MeV; antineutrinos produced by the decay of radioactive isotopes used in nuclear reactors, up to $\approx$ 10 MeV; and atmospheric neutrinos, for energies above 10 MeV. Another important background source are cosmic-ray muons, which produce neutrons or radioactive isotopes by spallation in the detector volume mimicking the signals of interest.

The SuperKamiokande (SK) experiment analyzed 1496 days of data from its first phase and reported [138] no excess of events corresponding to electron antineutrinos. With that, it was possible to set an upper limit to the flux of electron antineutrinos coming from the Sun at 90% C.L. at 0.8% of the SSM neutrino flux for the energy range 8 – 20 MeV. Additionally, the collaboration reported model-independent limits for the energy range 10 – 17 MeV shown in Figure 5.6.

Next, the KamLAND experiment [103] reported an upper limit of $Q_{\bar{\nu}_e} < 3.7 \times 10^2\,\mathrm{cm}^{-2} \cdot \mathrm{s}^{-1}$ at 90% C.L. for antineutrinos originating in the conversion of ^{8}B solar neutrinos, in the 8.3 – 14.8 MeV energy range, and based on data a 0.28 kton-year exposure of the detector which found no candidate events.

Meanwhile, the Borexino [140] experiment has also analyzed 736 days of data looking for antineutrinos of solar origin and set an upper limit of $Q_{\bar{\nu}_e} < 760\,\mathrm{cm}^{-2} \cdot \mathrm{s}^{-1}$ (at 90% C.L.) for $E_{\bar{\nu}_e} > 1.8\,\mathrm{MeV}$. In addition, model-independent limits were provided for the energy range 1.8 – 17.8 MeV, as shown in Figure 5.6.

Later, the KamLAND collaboration reported [139], for a 4.53 kton-year exposure, an upper limit on the probability of ^{8}B solar neutrinos converting into $\bar{\nu}_e$ at $P_{\nu_e \rightarrow \bar{\nu}_e} = 5.3 \times 10^{-5}$ at 90% CL. Assuming an unoscillated ^{8}B neutrino flux of $Q_{^8\mathrm{B}} = 5.94 \times 10^6\,\mathrm{cm}^{-2} \cdot \mathrm{s}^{-1}$, the collaboration reports an upper limit to solar electron antineutrino flux at $Q_{\bar{\nu}_e} < 93\,\mathrm{cm}^{-2} \cdot \mathrm{s}^{-1}$ at 90% C.L., for energies above the experiment's energy threshold $E_{\nu_e} > 8.3\,\mathrm{MeV}$. For this analysis, the collaboration also provides the model-independent limits for the energy range 8.3 – 18.3 MeV shown in Figure 5.6.

Recently, another report from the SK collaboration [142] using 960 days of data from SK-IV placed an upper limit for antineutrinos coming from the Sun at 0.042% at 90% C.L. of the SSM neutrino flux for $E_{\bar{\nu}_e} > 13.3\,\text{MeV}$, which is 20 times more stringent than their previous SK result, but less stringent than the KamLAND limit [139] because of the higher neutrino energy threshold. Model-independent limits are also provided for the energy range 13.3 – 17.3 MeV and shown in Figure 5.6.

Finally, the most recent Borexino collaboration report [141] set new limits for solar electron antineutrinos at $Q_{\bar{\nu}_e} < 138\,\text{cm}^{-2}\cdot\text{s}^{-1}$ at 90% C.L. for the energy range $> 7.8\,\text{MeV}$. This energy range corresponds to 36% of the ^{8}B neutrino flux. As such, a limit for the energy range $> 1.8\,\text{MeV}$ is reported at $Q_{\bar{\nu}_e} < 384\,\text{cm}^{-2}\cdot\text{s}^{-1}$ at 90% C.L., again assuming an undistorted ^{8}B neutrinos energy spectrum. The collaboration also reports model-independent limits for the energy range 1.8 – 16.8 MeV as shown in Figure 5.6.

The reported experimental limits to the solar electron antineutrino flux are summarized at Table 5.1. For comparison, we also include an early limit reported by the SNO collaboration [104] looked into positrons produced by the charged current interaction of antineutrinos with deuterium, which also produces two neutrons in coincidence. Two candidate events were found and, supposing that both are of solar origin, the collaboration could set an upper limit of $Q_{\bar{\nu}_e} < 3.4\times10^4\,\text{cm}^{-2}\cdot\text{s}^{-1}$ at 90% C.L. in the energy range 4.0 – 14.8 MeV.

Table 5.1: Experimental limits at 90% C.L. to electron antineutrino fluxes of solar origin as reported by different experiments, as described in the text. Included in this table are upper limits to the neutrino lifetime also investigated in some of the references. *Regarding the reported lifetime, top value corresponds to hierarchical scenario and bottom value corresponds to the quasi-degenerate scenario.

Experiment	Ref.	Total $\phi_{\bar{\nu}_e}(^8\text{B})$ [$\text{cm}^{-2}\cdot\text{s}^{-1}$]	Energy Range [MeV]	Report Lifetime [$\text{s}\cdot\text{eV}^{-1}$]
SuperKamiokande, 2002	[138]	$< 4.0\times10^4$	8 – 20	—
*SNO, 2004	[104]	$< 3.4\times10^4$	4 – 14.8	$> 4.4\times10^{-5}$ $> 4.0\times10^{-3}$
*KamLAND, 2003	[103]	< 370	8.3 – 14.8	$> 1.1\times10^{-3}$ $> 6.7\times10^{-2}$
Borexino, 2010	[140]	< 760	> 1.8	—
KamLAND, 2011	[139]	< 93	> 8.3	—
SuperKamiokande, 2013	[142]	$< 2.1\times10^3$	> 13.3	—
Borexino, 2019	[141]	< 138	> 7.8	—

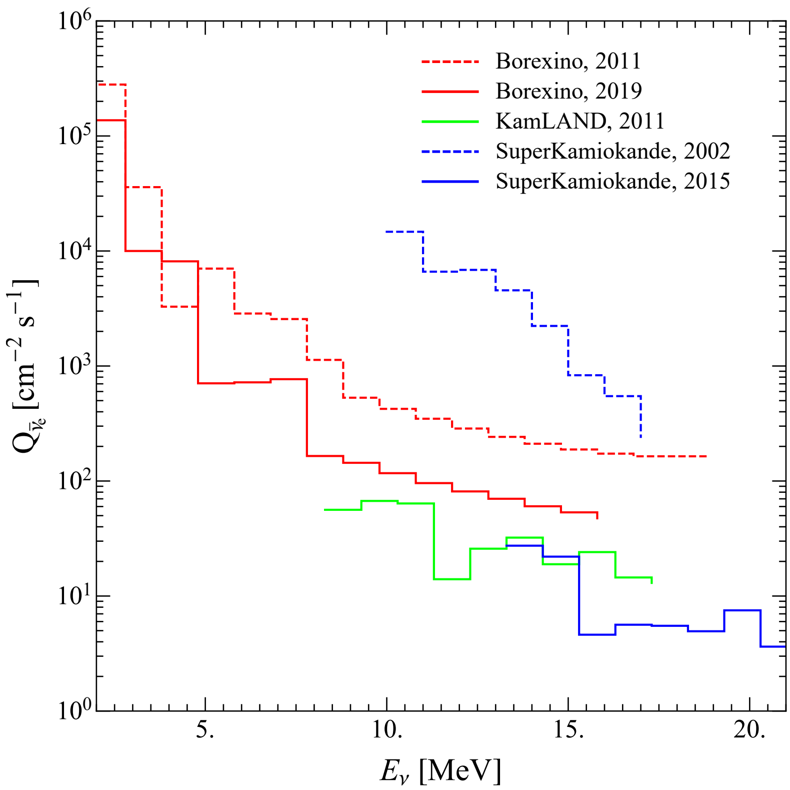

Figure 5.6: Model-independent upper limits to electron antineutrino fluxes reported by the Borexino [140, 141], SuperKamiokande [138, 142] and KamLAND [139] experiments. Figure made for this thesis based on plot by Reference [141].

By comparing the aforementioned solar electron antineutrino experimental limits to the theoretical fluxes expected in the context of solar neutrino decays, it is possible to set reliable limits to the neutrino lifetime in the context of each visible decay scenario as presented in the following sections. This part is original and not yet published.

5.5 Model Dependent Analysis

The number of antineutrinos detected in a given experiment is defined as

$$N = T \cdot n_p \cdot \varepsilon \cdot \int dE_\nu \Phi(E_\nu)\sigma(E_\nu)\,, \tag{5.85}$$

where T is the experiment's data collection time, n_p is the number of target protons in the experiment's fiducial volume, ε is the detection efficiency, and σ is the cross section for the inverse beta decay reaction. Equation (5.85) can be rewritten as

$$N = T \cdot n_p \cdot \varepsilon \cdot \frac{\left(\int dE_\nu \Phi(E_\nu)\sigma(E_\nu)\right)}{\left(\int dE_\nu \Phi(E_\nu)\right)} \left(\int dE_\nu \Phi(E_\nu)\right)\,, \tag{5.86}$$

and hence

$$N = T \cdot n_p \cdot \varepsilon \cdot \bar{\sigma} \cdot Q\,, \tag{5.87}$$

where $\bar{\sigma}$ is defined as the averaged cross section weighted over the incident antineutrino flux in the energy range of interest and Q is the total incident flux given in units of $\mathrm{cm}^{-2} \cdot \mathrm{s}^{-1}$. Thus, upon detection of events compatible with antineutrinos arriving from the Sun, the total incident antineutrino flux Q_{exp} can be calculated from the number of events N_{exp} as

$$Q_{\mathrm{exp}} = \frac{N_{\mathrm{exp}}}{T \cdot n_p \cdot \varepsilon \cdot \bar{\sigma}}\,. \tag{5.88}$$

In the experimental results reported in Section 5.4, the limits to Q_{exp} assume that the solar antineutrino flux follows the unoscillated ^{8}B neutrino flux modified by an energy-independent transition probability, i.e., they assume a **model** for the incoming antineutrino flux such that

$$\phi_{\bar{e}}^{\mathrm{naive}}(E_\nu) = a\,\phi_e^0(E_\nu)\,, \tag{5.89}$$

where ϕ_e^0 is the unoscillated ^{8}B solar neutrino flux and a is the energy-independent transition probability. Consequently, the averaged cross section weighted over $\phi_{\bar{e}}^{\mathrm{naive}}$ is given by

$$\bar{\sigma}_{\mathrm{naive}} = \frac{\left(\int dE_\nu \phi_e^0(E_\nu)\sigma(E_\nu)\right)}{\left(\int dE_\nu \phi_e^0(E_\nu)\right)}\,. \tag{5.90}$$

Consequently, the total incident antineutrino flux Q_{exp}^{naive} obtained and reported by the experiments is given by

$$Q_{\mathrm{exp}}^{\mathrm{naive}} = \frac{N_{\mathrm{exp}}}{T \cdot n_p \cdot \varepsilon \cdot \bar{\sigma}_{\mathrm{naive}}}\,. \tag{5.91}$$

However, as it is clear from Figures 5.2 – 5.5, the transition probabilities in the decay scenario are not energy-independent. As such, antineutrinos fluxes produced on decay may be very different from the original unoscillated ^{8}B solar neutrino flux ϕ_e^0.

Now, let $Q_{\mathrm{th}}^{\mathrm{decay}}$ be the theoretical total antineutrino flux expected from the decay of solar neutrinos, such that

$$Q_{\mathrm{th}}^{\mathrm{decay}} = \int dE_\nu \Phi_{\bar{e}}^{\mathrm{decay}}(E_\nu)\,, \tag{5.92}$$

where $\Phi_{\bar{e}}^{\mathrm{decay}}$ is the antineutrino flux produced in the decay of ^{8}B solar neutrinos, as given in Equations (5.8), (5.56) and (5.82). The averaged cross section $\bar{\sigma}^{\mathrm{decay}}$ weighted over $\Phi_{\bar{e}}^{\mathrm{decay}}$ is:

$$\bar{\sigma}_{\mathrm{decay}} = \frac{\left(\int dE_\nu \Phi_{\bar{e}}^{\mathrm{decay}}(E_\nu)\sigma(E_\nu)\right)}{\left(\int dE_\nu \Phi_{\bar{e}}^{\mathrm{decay}}(E_\nu)\right)}\,, \tag{5.93}$$

which is in general different from $\bar{\sigma}_{\text{naive}}$. Hence, before we can compare $Q_{\text{th}}^{\text{decay}}$ to $Q_{\text{exp}}^{\text{naive}}$, the reported experimental limits must be rescaled taking into account the energy-dependent transition probabilities of the decay scenarios. Since $N_{\text{exp}}^{\text{decay}} = N_{\text{exp}}^{\text{naive}}$, that is, the number of events detected by the experiment must be the same across models, and supposing the detection efficiency ε is independent of the shape of the incident flux, we can estimate the rescaled experimental flux limit $Q_{\text{exp}}^{\text{decay}}$ as

$$Q_{\text{exp}}^{\text{decay}} = \frac{\bar{\sigma}_{\text{naive}}}{\bar{\sigma}_{\text{decay}}} Q_{\text{exp}}^{\text{naive}}, \tag{5.94}$$

where $\bar{\sigma}_{\text{naive}}$ is weighted over the unoscillated ^{8}B solar neutrino spectrum ϕ_e^0 and $\bar{\sigma}_{\text{decay}}$ is weighted over the antineutrino fluxes produced in the decay of ^{8}B solar neutrinos $\Phi_{\bar{e}}^{\text{decay}}$. Finally, by enforcing $Q_{\text{th}}^{\text{decay}}$ less or equal to the rescaled experimental $Q_{\text{exp}}^{\text{decay}}$, that is

$$Q_{\text{th}}^{\text{decay}} \leq Q_{\text{exp}}^{\text{decay}}, \tag{5.95}$$

in the adequate energy range, we can extract lower limits to the neutrino lifetime in the context of different neutrino visible decay scenarios.

In the following sections, we calculate the antineutrino fluxes produced on decay $\Phi_{\bar{e}}^{\text{decay}}$ as given by Equations (5.8), (5.56) and (5.82). Next, we calculate $Q_{\text{th}}^{\text{decay}}$ as defined in Equation (5.92) and compare it to $Q_{\text{exp}}^{\text{decay}}$ as discussed above. For calculating $\Phi_{\bar{e}}^{\text{decay}}$, we assume the unoscillated total ^{8}B solar neutrino flux at production to be the best-fit value determined by Reference [143], from a global analysis of the solar and terrestrial neutrino data in the framework of three-neutrino mixing, given by

$$Q_{^8\text{B}} = 5.16^{(1+0.025)}_{(1-0.017)} \times 10^6\,\text{cm}^{-2}\cdot\text{s}^{-1}, \tag{5.96}$$

which is consistent with both high and low metallicity solar standard models [144].

5.5.1 Antineutrino Inverse Beta Decay Cross Section

The cross section for the inverse beta decay of antineutrinos ($\bar{\nu}_e + p \to e^+ + n$) is calculated in Reference [145]. The differential cross section at tree-level in the weak interaction, averaged over initial polarization and summed over final polarizations, is given by

$$\frac{d\sigma}{dE_e} = m_p \frac{G_F}{\pi} \cos^2\theta_c \frac{|\mathscr{M}^2|}{(s-m_p^2)^2}, \tag{5.97}$$

where G_F is the Fermi coupling constant, θ_c is the Cabbibo angle and $\mathscr{M}$ is the matrix element of the interaction, given by

$$|\mathscr{M}^2| = A(t) - (s-u)B(t) + (s-u)^2 C(t), \tag{5.98}$$

with the Mandelstam variables s, u and t given in the rest frame of the target proton as

$$s = 2m_p E_\nu + m_p^2\,, \tag{5.99}$$

$$s-u = 2m_p\left(E_\nu + E_e\right) - m_e^2\,, \tag{5.100}$$

$$t = m_n^2 - m_p^2 - 2m_p\left(E_\nu - E_e\right)\,, \tag{5.101}$$

where m_p, m_n, m_e, are the masses of protons, neutrons, and electrons respectively. From the expansion of $|\mathscr{M}^2|$ in powers of $\varepsilon = E_\nu/m_p$, the expressions for $A(t)$, $B(t)$ and $C(t)$ up to second order in ε (which is accurate enough up to supernova neutrino energies [145]) are given by

$$A \approx M^2(f_1^2 - g_1^2)(t - m_e^2) - M^2\Delta^2(f_1^2 + g_1^2) - 2m_e^2 M\Delta g_1(f_1 + f_2)\,, \tag{5.102}$$

$$B \approx t\, g_1(f_1 + f_2)\,, \tag{5.103}$$

$$C \approx \left(f_1^2 + g_1^2\right)/4\,, \tag{5.104}$$

where $M = (m_p + m_n)/2$ and $\Delta = m_n - m_p$. In this order of the expansion, the adimensional form factors f_i, g_i are constants approximated as $f_1 \approx 1$, $f_2 \approx \xi$ and $g_1 \approx \lambda$, where $\lambda = g_A/g_V = -1.270 \pm 0.003$ is the ratio of the axial vector to the vector coupling constant and $\xi = \kappa_p - \kappa_n = 3.706$, which is the difference between the anomalous magnetic moments of proton and neutron. The threshold energy E_{thr} for this reaction is

$$E_{\text{thr}} = \frac{(m_n + m_e)^2 - m_p^2}{2m_p} \approx 1.806\,\text{MeV}\,, \tag{5.105}$$

and the allowed values of E_e for a given value of E_ν are between the limits:

$$E_{\text{max/min}} = E_\nu - \frac{1}{2m_p}\left(m_n^2 - m_p^2 - m_e^2\right) - \frac{1}{m_p} E_\nu^{\text{CM}}\left(E_e^{\text{CM}} \pm p_e^{\text{CM}}\right)\,, \tag{5.106}$$

where the center-of-mass quantities E_ν^{CM}, E_e^{CM} and p_e^{CM} are given as

$$E_\nu^{\text{CM}} = \frac{1}{2\sqrt{s}}\,(s - m_p^2)\,, \tag{5.107}$$

$$E_e^{\text{CM}} = \frac{1}{2\sqrt{s}}\,(s - m_n^2 + m_e^2)\,, \tag{5.108}$$

$$p_e^{\text{CM}} = \frac{1}{2\sqrt{s}}\sqrt{s - (m_n - m_e)^2}\sqrt{s - (m_n + m_e)^2}\,. \tag{5.109}$$

Finally, the total cross section is obtained with the integration:

$$\sigma(E_\nu) = \Theta(E_\nu - E_{\text{thr}})\int_{E_{min}}^{E_{max}} dE_e \frac{d\sigma(E_\nu, E_e)}{dE_e}\,. \tag{5.110}$$

5.5.2 Model Dependent Analysis in the Normal Hierarchy

First, we investigate how upper limits to the total incident solar electron antineutrino fluxes defined for different energy ranges affect the bound we obtain for the neutrino lifetime. In this analysis, we focus on the decay channel $\nu_2 \to \nu_1/\bar{\nu}_1$ in the normal hierarchy. However, the general conclusions also apply to the other decay channels in the inverted hierarchy.

Here, we use the upper limits reported by the Borexino [141] collaboration, henceforward referenced simply as Borexino in text and as "BOR" in equations. Recalling Section 5.4, Borexino reports the upper limit

$$Q^{7.8}_{\mathrm{BOR}} \;<\; 138\,\mathrm{cm}^{-2}\cdot\mathrm{s}^{-1}\,, \quad \text{at 90\% C.L., for } E_{\nu_e} \;>\; 7.8\,\mathrm{MeV}\,, \tag{5.111}$$

which covers the energy range corresponding to 36% of the ^{8}B neutrino flux. As such, by extending $Q^{7.8}_{\mathrm{BOR}}$ to the whole energy spectrum covered by the experiment, $> 1.8\,\mathrm{MeV}$, another limit is reported at

$$Q^{1.8}_{\mathrm{BOR}} \;<\; 384\,\mathrm{cm}^{-2}\cdot\mathrm{s}^{-1}\,, \quad \text{at 90\% C.L., for } E_{\nu_e} \;>\; 1.8\,\mathrm{MeV}\,. \tag{5.112}$$

Below, we compare the bounds obtained for the neutrino lifetime for both solar electron antineutrino fluxes presented above.

Figure 5.7 shows the lower limits obtained to τ_2/m_2 as a function of $\delta = m_1/m_2$ for each of the coupling constant cases in the context of the model-dependent 90% C.L. upper limits to antineutrino fluxes $Q^{1.8}_{\mathrm{BOR}}$ and $Q^{7.8}_{\mathrm{BOR}}$ defined above.

As expected from Figure 3.2, at $\delta = 0$, corresponding to the hierarchical scenario of neutrino masses, the different coupling constants cases reduce to one single bound to the neutrino lifetime as seen in Figure 5.7:

$$\left(\frac{\tau_2}{m_2}\right)^{\mathrm{NH}}_{2\to 1} > 6.6\times 10^{-3}\,\mathrm{s}\cdot\mathrm{eV}^{-1}\,, \quad \text{at 90\% C.L., for } Q^{7.8}_{\mathrm{BOR}}\,, \tag{5.113}$$

$$\left(\frac{\tau_2}{m_2}\right)^{\mathrm{NH}}_{2\to 1} > 2.6\times 10^{-2}\,\mathrm{s}\cdot\mathrm{eV}^{-1}\,, \quad \text{at 90\% C.L., for } Q^{1.8}_{\mathrm{BOR}}\,. \tag{5.114}$$

As it can be seen, there is a substantial difference between the lifetime obtained for $Q^{1.8}_{\mathrm{BOR}}$ and $Q^{7.8}_{\mathrm{BOR}}$. This is explained by the fact that, in the hierarchical scenario, daughter neutrinos can be produced in a much lower energy than their mother particle, as it can be seen in Figure 5.2. As such, limits to antineutrino fluxes covering lower energies will produce stronger bounds to neutrino lifetime than equivalent limits covering only higher energies.

On the other hand, as δ grows, the different cases for the coupling constants diverge into separate limits, with the stronger limit always set by the purely pseudoscalar case. For

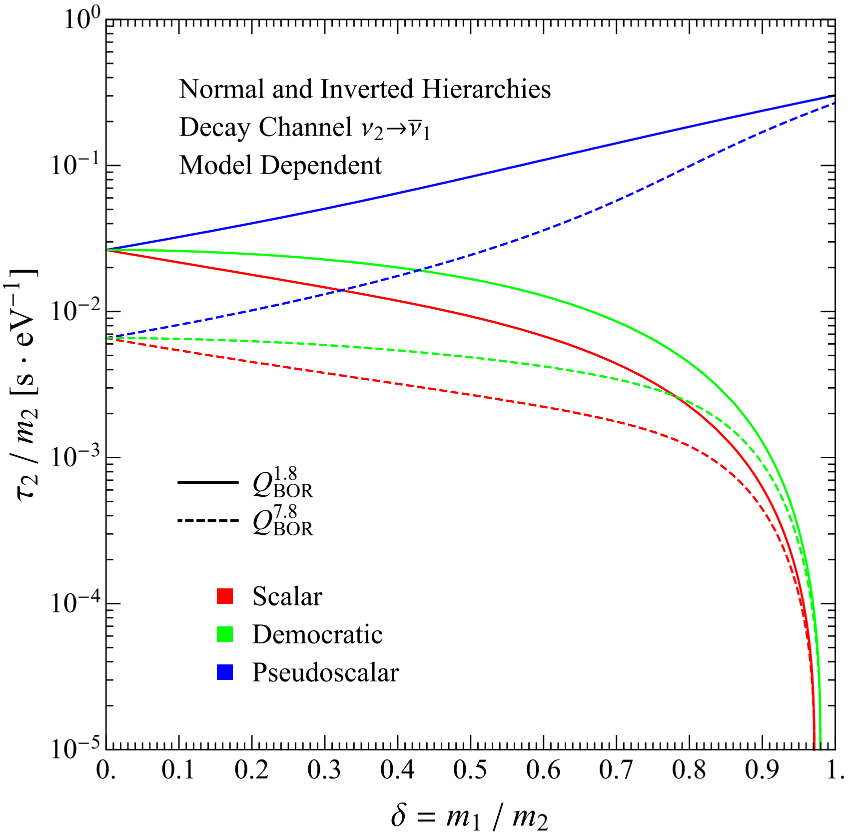

Figure 5.7: Lower limits to τ_2/m_2 at 90% C.L. on the decay channel $\nu_2 \to \nu_1/\bar{\nu}_1$ in the normal hierarchy as a function of $\delta = m_1/m_2$ for each of the coupling constant cases in the context of the model-dependent 90% C.L. upper limits to antineutrino fluxes reported by Borexino, $Q^{1.8}_{\rm BOR}$ and $Q^{7.8}_{\rm BOR}$. Curves correspond to $Q^{\rm decay}_{\rm th} = Q^{\rm decay}_{\rm exp}$. Best-fit values for the global fit neutrino oscillation parameters [59] as shown on Table 2.1 are used. This plot is an original work made for this thesis.

instance, for $\delta = 0.96$:

$$\left(\frac{\tau_2}{m_2}\right)^{\rm NH}_{2\to1} > 2.3 \times 10^{-1}\,{\rm s \cdot eV^{-1}}\,, \quad \text{at 90\% C.L., for } Q^{7.8}_{\rm BOR}\,, \tag{5.115}$$

$$\left(\frac{\tau_2}{m_2}\right)^{\rm NH}_{2\to1} > 2.7 \times 10^{-1}\,{\rm s \cdot eV^{-1}}\,, \quad \text{at 90\% C.L., for } Q^{1.8}_{\rm BOR}\,. \tag{5.116}$$

As it can be seen, there is much a smaller difference between the lifetime obtained for $Q^{1.8}_{\rm BOR}$ and $Q^{7.8}_{\rm BOR}$. This is explained by the fact that, for higher values of δ, daughter neutrinos are produced at roughly the same energy as their mother particle, as it can be seen in Figures 5.3 and 5.4. As such, the energy range covered by the antineutrino flux limits will have a much smaller influence on the bounds to neutrino lifetime.

Although $Q^{1.8}_{\rm BOR}$ yields stronger limits to τ_2/m_2 than $Q^{7.8}_{\rm BOR}$, since $Q^{1.8}_{\rm BOR}$ is obtained by extending $Q^{7.8}_{\rm BOR}$ to the whole energy spectrum covered by the experiment, we consider $Q^{7.8}_{\rm BOR}$ to be the more adequate value to be taken and further compared to other experimental limits to the total incident solar electron antineutrino fluxes. This choice is further justified by comparing the model dependent analysis below with the model independent analysis presented in Section 5.6.

Now, we analyze to bound to neutrino lifetime obtained from the upper limit at 90% C.L. to the total incident solar electron antineutrino fluxes as reported by the KamLAND [139] collaboration, henceforward referenced simply as KamLAND in text and as "KL" in equations.

Recalling Section 5.4, KamLAND sets the upper limit on the probability of ^{8}B solar neutrinos converting into $\bar{\nu}_e$ at $P_{\nu_e \to \bar{\nu}_e} = 5.3 \times 10^{-5}$ at 90% CL. The collaboration assumes an unoscillated ^{8}B neutrino flux of $Q_{^8\mathrm{B}} = 5.94 \times 10^6\,\mathrm{cm}^{-2} \cdot \mathrm{s}^{-1}$, and reports $Q_{\bar{\nu}_e} < 93\,\mathrm{cm}^{-2} \cdot \mathrm{s}^{-1}$ at 90% C.L. to the upper limit to solar electron antineutrino flux for energies above the experiment's energy threshold $E_{\nu_e} > 8.3\,\mathrm{MeV}$. However, for our choice of $Q_{^8\mathrm{B}} = 5.16 \times 10^6\,\mathrm{cm}^{-2} \cdot \mathrm{s}^{-1}$ in Equation (5.96), the limit is recalculated to:

$$Q_{\mathrm{KL}}^{8.3} < 81\,\mathrm{cm}^{-2} \cdot \mathrm{s}^{-1}\,, \quad \text{at 90\% C.L., for } E_{\nu_e} > 8.3\,\mathrm{MeV}\,, \tag{5.117}$$

which we use in the analysis below. For comparison, we use $Q_{\mathrm{BOR}}^{7.8}$, discussed previously, which covers an energy range similar to $Q_{\mathrm{KL}}^{8.3}$.

Figure 5.8 shows the lower limits obtained to τ_2/m_2 as a function of δ for each of the coupling constant cases in the context of the model-dependent 90% C.L. upper limits $Q_{\mathrm{BOR}}^{7.8}$ and $Q_{\mathrm{KL}}^{8.3}$. For comparison, we also present the invisible decay limit $1.92 \times 10^{-3}\,\mathrm{s} \cdot \mathrm{eV}^{-1}$ at 90% C.L. as reported by the SNO Collaboration [112]. In Table 5.2 lower limits to τ_2/m_2 are shown for selected values of δ.

As before, at $\delta = 0$ the different coupling constants cases reduce to one single lifetime limit for each of the antineutrino flux experimental limits:

$$\left(\frac{\tau_2}{m_2}\right)_{2\to 1}^{\mathrm{NH}} > 6.6 \times 10^{-3}\,\mathrm{s} \cdot \mathrm{eV}^{-1}\,, \quad \text{at 90\% C.L., for } Q_{\mathrm{BOR}}^{7.8}, \tag{5.118}$$

$$\left(\frac{\tau_2}{m_2}\right)_{2\to 1}^{\mathrm{NH}} > 7.5 \times 10^{-3}\,\mathrm{s} \cdot \mathrm{eV}^{-1}\,, \quad \text{at 90\% C.L., for } Q_{\mathrm{KL}}^{8.3}. \tag{5.119}$$

For higher values of δ, the strongest lifetime limit is as expected set by the purely pseudoscalar case. Again, for $\delta = 0.96$:

$$\left(\frac{\tau_2}{m_2}\right)_{2\to 1}^{\mathrm{NH}} > 2.3 \times 10^{-1}\,\mathrm{s} \cdot \mathrm{eV}^{-1}\,, \quad \text{at 90\% C.L., for } Q_{\mathrm{BOR}}^{7.8}, \tag{5.120}$$

$$\left(\frac{\tau_2}{m_2}\right)_{2\to 1}^{\mathrm{NH}} > 3.1 \times 10^{-1}\,\mathrm{s} \cdot \mathrm{eV}^{-1}\,, \quad \text{at 90\% C.L., for } Q_{\mathrm{KL}}^{8.3}. \tag{5.121}$$

As it can be seen, for either value of δ, the stronger is upper limit to the total incident solar electron antineutrino flux in a given energy range, the stronger is the bound obtained for the neutrino lifetime.

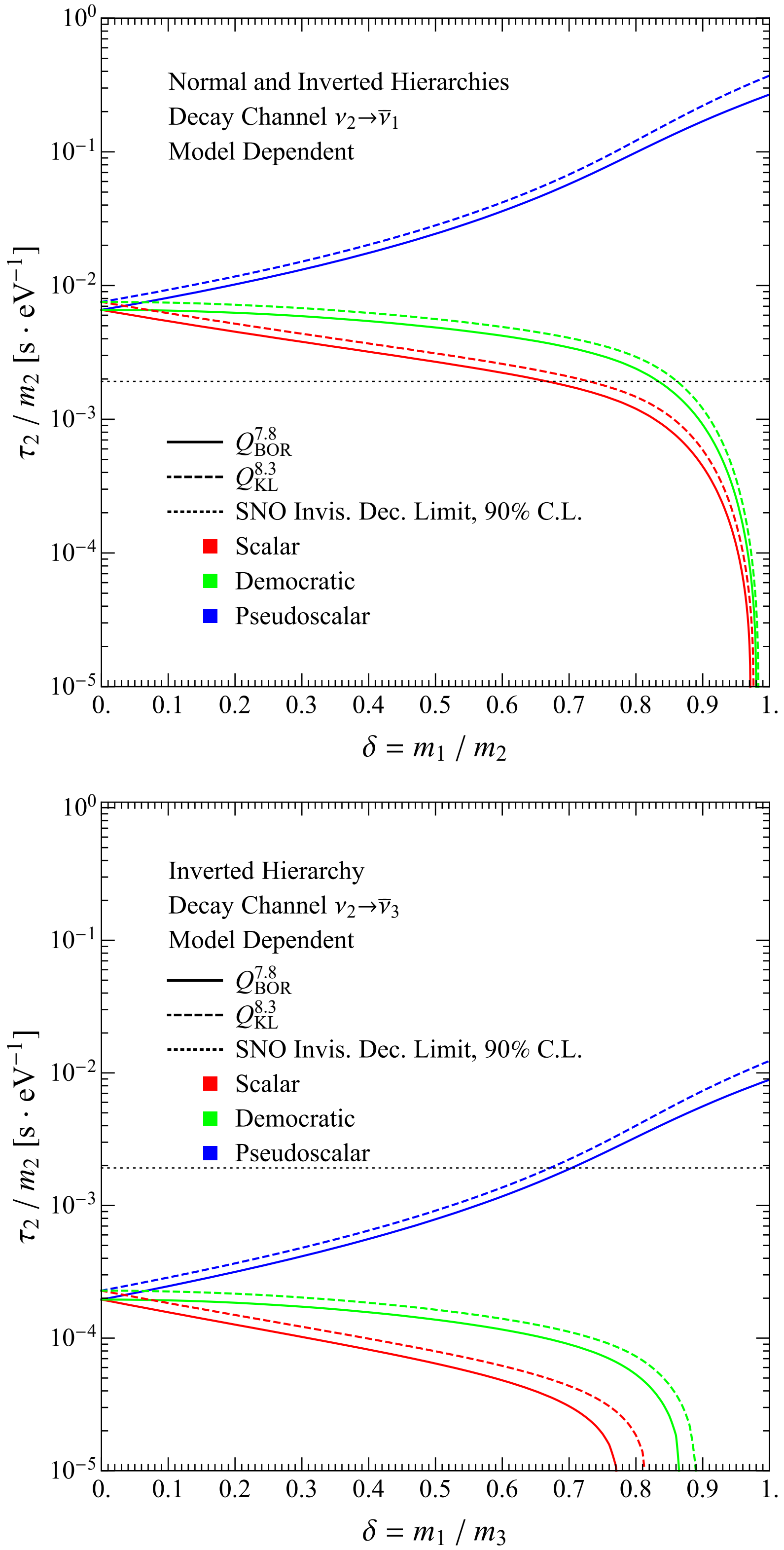

Figure 5.8: Lower limits to τ_2/m_2 at 90% C.L. as function of $\delta = m_1/m_2$ for each of the coupling constant cases in the context of the model-dependent 90% C.L. upper limits to antineutrino fluxes reported by Borexino and KamLAND. Top: decay channel $\nu_2 \to \nu_1/\bar{\nu}_1$ in the normal and inverted hierarchies. Bottom: decay channel $\nu_2 \to \nu_3/\bar{\nu}_3$ in inverted hierarchy. In both plots, the dotted black line represents the 90% C.L. lower limit to τ_2/m_2 in the context of invisible decays as reported by the SNO Collaboration [112]. Curves correspond to $Q^{\text{decay}}_{\text{th}} = Q^{\text{decay}}_{\text{exp}}$. Best-fit values for the global fit neutrino oscillation parameters [59] as shown on Table 2.1 are used.

Table 5.2: Selected lower limit values to τ_2/m_2 [$\mathrm{s} \cdot \mathrm{eV}^{-1}$] at 90% C.L. for different values of $\delta = m_1/m_2$ for each of the coupling constant cases in the context of the model-dependent 90% C.L. upper limits to antineutrino fluxes reported by Borexino and KamLAND. Highlighted lifetimes are discussed in the text.

(a) $\nu_2 \to \nu_1/\bar{\nu}_1$, normal and inverted hierarchies

	Borexino			KamLAND		
δ	Scalar Coupling	Democratic Coupling	Pseudoscalar Coupling	Scalar Coupling	Democratic Coupling	Pseudoscalar Coupling
0	6.6×10^{-3}	6.6×10^{-3}	6.6×10^{-3}	7.5×10^{-3}	7.5×10^{-3}	7.5×10^{-3}
0.3	3.8×10^{-3}	5.9×10^{-3}	1.3×10^{-2}	4.4×10^{-3}	6.8×10^{-3}	1.5×10^{-2}
0.7	1.8×10^{-3}	3.4×10^{-3}	5.7×10^{-2}	2.1×10^{-3}	4.1×10^{-3}	6.7×10^{-2}
0.9	4.4×10^{-4}	9.1×10^{-3}	1.7×10^{-1}	5.9×10^{-4}	1.2×10^{-3}	2.2×10^{-1}
0.96	6.6×10^{-5}	1.6×10^{-4}	2.3×10^{-1}	1.1×10^{-4}	2.3×10^{-4}	3.1×10^{-1}
0.99	$< 10^{-8}$	$< 10^{-8}$	2.6×10^{-1}	$< 10^{-8}$	$< 10^{-8}$	3.5×10^{-1}

(b) $\nu_2 \to \nu_3/\bar{\nu}_3$, inverted hierarchy

	Borexino			KamLAND		
δ	Scalar Coupling	Democratic Coupling	Pseudoscalar Coupling	Scalar Coupling	Democratic Coupling	Pseudoscalar Coupling
0	1.9×10^{-4}	1.9×10^{-4}	1.9×10^{-4}	2.3×10^{-4}	2.3×10^{-4}	2.3×10^{-4}
0.3	1.0×10^{-4}	1.7×10^{-4}	4.1×10^{-4}	1.2×10^{-4}	2.0×10^{-4}	4.8×10^{-4}
0.7	3.1×10^{-5}	9.0×10^{-5}	1.9×10^{-3}	4.4×10^{-5}	1.1×10^{-4}	2.2×10^{-3}
0.9	$< 10^{-8}$	$< 10^{-8}$	5.6×10^{-3}	$< 10^{-8}$	$< 10^{-8}$	7.3×10^{-3}
0.96	$< 10^{-8}$	$< 10^{-8}$	7.5×10^{-3}	$< 10^{-8}$	$< 10^{-8}$	1.0×10^{-2}
0.99	$< 10^{-8}$	$< 10^{-8}$	8.5×10^{-3}	$< 10^{-8}$	$< 10^{-8}$	1.2×10^{-2}

5.5.3 Model Dependent Analysis in the Inverted Hierarchy

Figure 5.8 shows the lower limits obtained to τ_2/m_2 as a function of δ for each of the coupling constant cases in the context of the model-dependent 90% C.L. upper limits $Q^{7.8}_{\rm BOR}$ and $Q^{8.3}_{\rm KL}$. For comparison, we also present the invisible decay limit $\tau_2/m_2 > 1.92 \times 10^{-3}\,\mathrm{s}\cdot\mathrm{eV}^{-1}$ at 90% C.L. as reported by the SNO Collaboration [112]. In Table 5.2 lower limits to τ_2/m_2 are shown for selected values of δ.

For the decay channel $\nu_2 \to \nu_1/\bar{\nu}_1$ in the inverted hierarchy, the electron antineutrino flux follows the same expression as in the normal hierarchy, as discussed in Section 5.3. The difference comes from allowed values of δ, as discussed in Section 5.2, which is $0.985 \le \delta \le 0.987$. In this range, only the pseudoscalar case leads to a stronger lower limit to τ_2/m_2 lifetime when compared to the invisible decay limit. For $\delta = 0.987$, this limit is

$$\left(\frac{\tau_2}{m_2}\right)^{\rm IH}_{2\to1} > 2.5\times10^{-1}\,\mathrm{s}\cdot\mathrm{eV}^{-1}\,, \quad \text{at 90\% C.L., for } Q^{7.8}_{\rm BOR}, \tag{5.122}$$

$$\left(\frac{\tau_2}{m_2}\right)^{\rm IH}_{2\to1} > 3.5\times10^{-1}\,\mathrm{s}\cdot\mathrm{eV}^{-1}\,, \quad \text{at 90\% C.L., for } Q^{8.3}_{\rm KL}. \tag{5.123}$$

On the other hand, for the decay channel $\nu_2 \to \nu_3/\bar{\nu}_3$, the limits to τ_2/m_2 are substantially weaker than the limits obtained for the decay channel $\nu_2 \to \nu_1/\bar{\nu}_1$ in either hierarchy. Additionally, since the allowed values for δ in this case are $0 \le \delta \le 0.3$, all obtained limits are also weaker than the invisible decay limit. For comparison, the pseudoscalar case provides the strongest limit, which, for $\delta = 0.3$, is

$$\left(\frac{\tau_2}{m_2}\right)^{\rm IH}_{2\to3} > 4.1\times10^{-4}\,\mathrm{s}\cdot\mathrm{eV}^{-1}\,, \quad \text{at 90\% C.L., for } Q^{7.8}_{\rm BOR}, \tag{5.124}$$

$$\left(\frac{\tau_2}{m_2}\right)^{\rm IH}_{2\to3} > 4.8\times10^{-4}\,\mathrm{s}\cdot\mathrm{eV}^{-1}\,, \quad \text{at 90\% C.L., for } Q^{8.3}_{\rm KL}. \tag{5.125}$$

5.6 Model Independent Analysis

In addition to the previous analysis, it is possible to compare the theoretical fluxes expected in the context of solar neutrino decay to the model-independent limits reported by Borexino and KamLAND, shown in Figure 5.6. The bin-per-bin analysis is performed using the χ^2 function defined in [139]:

$$\chi^2 = \sum_i \frac{v_i^2}{(u_i/\sqrt{2.71})^2}\,, \tag{5.126}$$

where v_i is the expected antineutrino flux for each bin, u_i is the experiment's upper limit for each bin, and $\sqrt{2.71}$ is the conversion factor of limits from 90% C.L. to 1σ C.L., corresponding to $\Delta\chi^2_{90\%\mathrm{C.L.}}/\Delta\chi^2_{1\sigma}$.

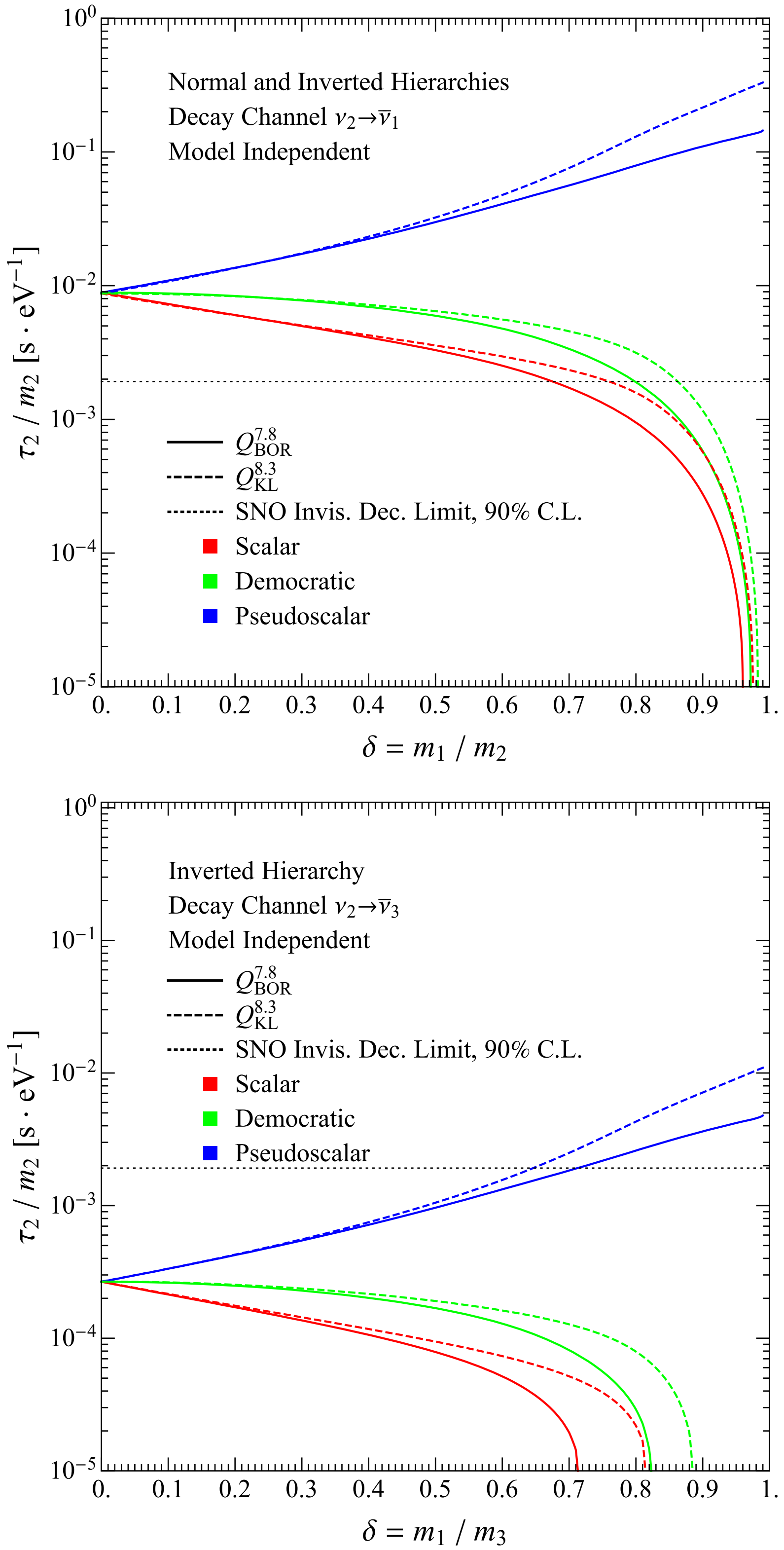

Figure 5.9: Lower limits to τ_2/m_2 as function of $\delta = m_1/m_2$ for each of the coupling constant cases in the context of the model-independent 90% C.L. upper limits to antineutrino fluxes reported by Borexino and KamLAND. Top: decay channel $\nu_2 \to \nu_1/\bar{\nu}_1$ in the normal and inverted hierarchies. Bottom: decay channel $\nu_2 \to \nu_3/\bar{\nu}_3$ in inverted hierarchy. Curves correspond to $\Delta\chi^2 = 2.71$, or 90% C.L.. In both plots, the dotted black line represents the 90% C.L. lower limit to τ_2/m_2 in the context of invisible decays as reported by the SNO Collaboration [112]. Best-fit values for the global fit neutrino oscillation parameters [59] as shown on Table 2.1 are used. These plots are original works made for this thesis.

Table 5.3: Selected lower limit values to τ_2/m_2 [$\mathrm{s \cdot eV^{-1}}$] at 90% C.L. for different values of $\delta = m_1/m_2$ for each of the coupling constant cases in the context of the model-independent 90% C.L. upper limits to antineutrino fluxes reported by Borexino and KamLAND.

(a) $\nu_2 \to \nu_1/\bar{\nu}_1$, normal and inverted hierarchies

	Borexino			KamLAND		
δ	Scalar Coupling	Democratic Coupling	Pseudoscalar Coupling	Scalar Coupling	Democratic Coupling	Pseudoscalar Coupling
0	8.9×10^{-3}	8.9×10^{-3}	8.9×10^{-3}	8.7×10^{-3}	8.7×10^{-3}	8.7×10^{-3}
0.3	5.0×10^{-3}	7.8×10^{-3}	1.7×10^{-2}	5.0×10^{-3}	7.8×10^{-3}	1.7×10^{-2}
0.7	1.7×10^{-3}	3.4×10^{-3}	5.6×10^{-2}	2.3×10^{-3}	4.6×10^{-3}	7.6×10^{-2}
0.9	2.8×10^{-4}	5.8×10^{-4}	1.1×10^{-1}	5.7×10^{-4}	1.2×10^{-3}	2.2×10^{-1}
0.96	1.0×10^{-5}	7.8×10^{-5}	1.3×10^{-1}	9.3×10^{-5}	2.1×10^{-4}	2.9×10^{-1}
0.99	$< 10^{-8}$	$< 10^{-8}$	1.4×10^{-1}	$< 10^{-8}$	$< 10^{-8}$	3.3×10^{-1}

(b) $\nu_2 \to \nu_3/\bar{\nu}_3$, inverted hierarchy

	Borexino			KamLAND		
δ	Scalar Coupling	Democratic Coupling	Pseudoscalar Coupling	Scalar Coupling	Democratic Coupling	Pseudoscalar Coupling
0	2.7×10^{-4}	2.7×10^{-4}	2.7×10^{-4}	2.7×10^{-4}	2.7×10^{-4}	2.7×10^{-4}
0.3	1.4×10^{-4}	2.3×10^{-4}	5.5×10^{-4}	1.4×10^{-4}	2.4×10^{-4}	5.6×10^{-4}
0.7	1.9×10^{-5}	8.1×10^{-5}	1.8×10^{-3}	5.2×10^{-5}	1.3×10^{-4}	2.5×10^{-3}
0.9	$< 10^{-8}$	$< 10^{-8}$	3.6×10^{-3}	$< 10^{-8}$	$< 10^{-8}$	7.1×10^{-3}
0.96	$< 10^{-8}$	$< 10^{-8}$	4.3×10^{-3}	$< 10^{-8}$	$< 10^{-8}$	9.5×10^{-3}
0.99	$< 10^{-8}$	$< 10^{-8}$	4.8×10^{-3}	$< 10^{-8}$	$< 10^{-8}$	1.1×10^{-2}

Figure 5.9 shows the lower limits obtained to τ_2/m_2 as a function of δ for each of the coupling constant cases in the context of the model-independent 90% C.L. upper limits reported by Borexino and KamLAND. Again, we present the invisible decay limit $\tau_2/m_2 > 1.92 \times 10^{-3}\,\mathrm{s \cdot eV^{-1}}$ at 90% C.L. as reported by the SNO Collaboration [112] for comparison. In Table 5.3 lower limits to τ_2/m_2 are shown for selected values of δ. In Figure 5.9, the labels $Q^{7.8}_{\mathrm{BOR}}$ and $Q^{8.3}_{\mathrm{KL}}$ are used to denote the model-independent limits only as means to facilitate the comparison between model -dependent and -independent analyses.

As it can be seen in Figure 5.10, the results are fairly similar to those obtained for the model-dependent limits, qualitatively and quantitatively, for both decay channels and hierarchies. In general, for small values of δ the model-independent analysis leads to better limits to the lifetime, while for large values of δ the model-dependent analysis leads to better limits to the lifetime.

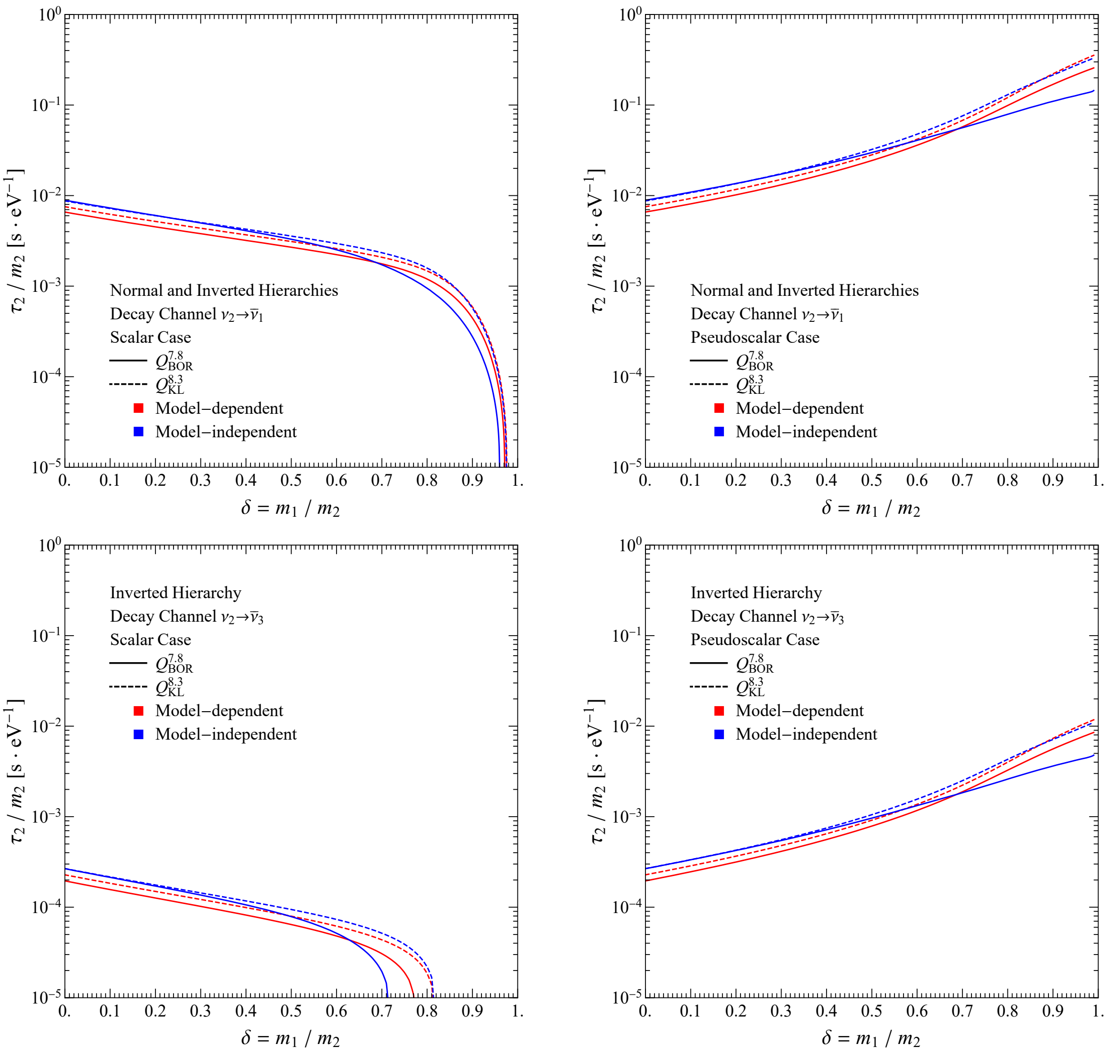

Figure 5.10: Comparison between model-dependent and -independent lower limits to τ_2/m_2 in the scalar and pseudo-scalar cases as a function of $\delta = m_1/m_2$. Top: $\nu_2 \to \nu_1/\bar{\nu}_1$. Bottom: $\nu_2 \to \nu_3/\bar{\nu}_3$. Best-fit values for the global fit neutrino oscillation parameters [59] as shown on Table 2.1 are used. These plots are original works made for this thesis.

5.7 Comparison to Current Lifetime Limits

As shown in Table 5.1, the latest limits to the τ_2/m_2 lifetime in the context of the visible decay of solar neutrinos are reported by the KamLAND collaboration [103]:

$$\left(\frac{\tau_2}{m_2}\right)_{\mathrm{KL}} > 1.1\times 10^{-3}\,\mathrm{s}\cdot\mathrm{eV}^{-1}\,, \quad \text{at 90\% C.L.}, \tag{5.127}$$

in the hierarchical scenario ($\delta = 0$), and

$$\left(\frac{\tau_2}{m_2}\right)_{\mathrm{KL}} > 6.7\times 10^{-2}\,\mathrm{s}\cdot\mathrm{eV}^{-1}\,, \quad \text{at 90\% C.L.}, \tag{5.128}$$

in the quasi-degenerate scenario ($\delta \to 1$), for the decay channel $\nu_2 \to \nu_1/\bar{\nu}_1$ in the normal hierarchy.

Among the results presented in the previous sections, we conservatively choose the model-dependent analysis results to the τ_2/m_2 lifetime, which are overall slightly weaker than the model-independent results. However, we choose the results obtained from KamLAND stronger antineutrino flux limit $Q_{\mathrm{KL}}^{8.3}$. As such, we have:

$$\left(\frac{\tau_2}{m_2}\right)_{2\to 1}^{\mathrm{NH}} > 7.5\times 10^{-3}\,\mathrm{s}\cdot\mathrm{eV}^{-1}\,, \quad \text{at 90\% C.L., for } \delta = 0, \tag{5.129}$$

in any coupling constant case, and

$$\left(\frac{\tau_2}{m_2}\right)_{2\to 1}^{\mathrm{NH}} > 3.1\times 10^{-1}\,\mathrm{s}\cdot\mathrm{eV}^{-1}\,, \quad \text{at 90\% C.L., for } \delta = 0.96, \tag{5.130}$$

in the pseudoscalar case. As it can be seen, our analysis represent a fivefold improvement upon the previously reported limit due to the use of most recent KamLAND [139] results. Our analysis for the visible decay also presents stronger limits to the τ_2/m_2 lifetime than the invisible decay limit $\tau_2/m_2 > 1.92\times 10^{-3}\,\mathrm{s}\cdot\mathrm{eV}^{-1}$ at 90% C.L..

Additionally, we have investigated limits to the τ_2/m_2 lifetime in the inverted hierarchy for both decay channels $\nu_2 \to \nu_1/\bar{\nu}_1$ and $\nu_2 \to \nu_3/\bar{\nu}_3$, which have not been previously discussed in the literature. For the decay channel $\nu_2 \to \nu_1/\bar{\nu}_1$ in the inverted hierarchy, since the allowed values for δ are very constrained, a slightly stronger limit is set at

$$\left(\frac{\tau_2}{m_2}\right)_{2\to 1}^{\mathrm{IH}} > 3.5\times 10^{-1}\,\mathrm{s}\cdot\mathrm{eV}^{-1}\,, \quad \text{at 90\% C.L., for } \delta = 0.987, \tag{5.131}$$

in the pseudoscalar case. Finally, for the decay channel $\nu_2 \to \nu_3/\bar{\nu}_3$, as discussed before, the limits to τ_2/m_2 are substantially weaker than those in the decay channel $\nu_2 \to \nu_1/\bar{\nu}_1$ in either hierarchy, and, for all allowed values of δ, those limits are also weaker than the invisible decay limit.

Conclusion

Solar neutrinos are produced in the thermonuclear fusion processes that power the Sun. Early experiments detected a solar neutrino flux lower than the predicted by the Solar Standard Models, a deficit known as the Solar Neutrino Problem (SNP). Over the years, results from neutrino experiments eventually established the Neutrino Flavor Oscillation model with Large Mixing Angle and Mikheyev-Smirnov-Wolfenstein Resonant Flavor Conversion (LMA-MSW) as the best solution to the SNP, establishing beyond reasonable doubt the massive nature of neutrinos. Being massive, it is possible for neutrinos to decay into other particles. Hence, although previously ruled out as a leading process in the SNP, we analysed neutrino decay as a sub-leading effect in the propagation of solar neutrinos to extract new limits to neutrino lifetime in a range of decay scenarios using the most recent experimental data.

From the combined analysis of data of solar neutrino experiments and KamLAND and Daya Bay data, we have obtained [122] a new upper bound to the ν_2 eigenstate lifetime $\tau_2/m_2 \geq 7.2\times10^{-4}\,\mathrm{s}\cdot\mathrm{eV}^{-1}$ at 99% C.L. in the context of the invisible decay scenario, improving in almost one order the previous established bound [99]. We have also shown how decay can enhance the seasonal variation of solar neutrino fluxes and how it affects the measurement of Earth's orbital eccentricity using neutrinos.

Additionally, from the most recent limits on antineutrinos fluxes originating in the Sun, we obtained new limits to ν_2 eigenstate lifetime τ_2/m_2 in the context of neutrino visible decays. As such, we set the limits at $\tau_2/m_2 > 7.5\times10^{-3}\,\mathrm{s}\cdot\mathrm{eV}^{-1}$ at 90% C.L., for $\delta = 0$ corresponding to the hierarchical scenario of neutrino masses; and at $\tau_2/m_2 > 3.1\times10^{-1}\,\mathrm{s}\cdot\mathrm{eV}^{-1}$ at 90% C.L., for $\delta = 0.96$ corresponding to the current cosmological limit to the sum of neutrino masses. Our limits are an improvement upon previous limits in the context of visible [103] and invisible decays [112]. This is an original result and not yet published.

Bibliography

1. Pauli, W. Offener Brief an die Gruppe der Radioaktiven bei der Gauvereins-Tagung zu Tübingen — Open letter to the group of radioactive people at the Gauverein meeting in Tübingen (1930). https://cds.cern.ch/record/83282.

2. Longair, M. S. *High Energy Astrophysics* (Cambridge University Press, 2011).

3. Bahcall, J. N. *Neutrino Astrophysics* (Cambridge University Press, 1989).

4. Zyla, P. *et al.* Review of Particle Physics. *PTEP* **2020**, 083C01 (2020). doi:10.1093/ptep/ptaa104.

5. Bahcall, J. N., Serenelli, A. M. & Basu, S. New solar opacities, abundances, helioseismology, and neutrino fluxes. *Astrophys. J.* **621**, L85–L88 (2005). doi:10.1086/428929. arXiv:astro-ph/0412440.

6. Tayler, R. J. *The Sun as a star* (Cambridge University Press, 1997).

7. Giunti, C. & Kim, C. W. *Fundamentals of Neutrino Physics and Astrophysics* (Oxford University Press, 2007).

8. Prialnik, D. *An Introduction to the Theory of Stellar Structure and Evolution - Second Edition* (Cambridge University Press, 2010).

9. Mitalas, R. & Sills, K. R. On the Photon Diffusion Time Scale for the Sun. *The Astrophysical Journal* **401**, 759 (1992). doi:10.1086/172103.

10. Cleveland, B. T. *et al.* Measurement of the solar electron neutrino flux with the Homestake chlorine detector. *Astrophys. J.* **496**, 505–526 (1998). doi:10.1086/305343.

11. Bahcall, J. N., Serenelli, A. M. & Basu, S. 10,000 standard solar models: a Monte Carlo simulation. *Astrophys. J. Suppl.* **165**, 400–431 (2006). doi:10.1086/504043. arXiv:astro-ph/0511337.

12. Davis, R., Jr., Harmer, D. S. & Hoffman, K. C. Search for neutrinos from the sun. *Phys. Rev. Lett.* **20**, 1205–1209 (1968). doi:10.1103/PhysRevLett.20.1205.

13. Bahcall, J. N. & Pinsonneault, M. H. Solar models with helium and heavy element diffusion. *Rev. Mod. Phys.* **67**, 781–808 (1995). doi:10.1103/RevModPhys.67.781. arXiv:hep-ph/9505425.

14. Hampel, W. *et al.* GALLEX solar neutrino observations: Results for GALLEX IV. *Phys. Lett.* **B447**, 127–133 (1999). doi:10.1016/S0370-2693(98)01579-2.

15. Altmann, M. *et al.* Complete results for five years of GNO solar neutrino observations. *Phys. Lett.* **B616**, 174–190 (2005). doi:10.1016/j.physletb.2005.04.068. arXiv:hep-ex/0504037.

16. Abdurashitov, J. N. *et al.* Measurement of the solar neutrino capture rate with gallium metal. III: Results for the 2002–2007 data-taking period. *Phys. Rev.* **C80**, 015807 (2009). doi:10.1103/PhysRevC.80.015807. arXiv:0901.2200.

17. Arisaka, K. *et al.* KAMIOKA nucleon decay experiments; status and performance. *AIP Conf. Proc.* **114**, 54–76 (1984). doi:10.1063/1.34507.

18. Hirata, K. S. *et al.* Observation of ^{8}B solar neutrinos in the Kamiokande-II detector. *Phys. Rev. Lett.* **63**, 16 (1989). doi:10.1103/PhysRevLett.63.16.

19. Hirata, K. S. *et al.* Results from one thousand days of real time directional solar neutrino data. *Phys. Rev. Lett.* **65**, 1297–1300 (1990). doi:10.1103/PhysRevLett.65.1297.

20. Fukuda, Y. *et al.* Solar neutrino data covering solar cycle 22. *Phys. Rev. Lett.* **77**, 1683–1686 (1996). doi:10.1103/PhysRevLett.77.1683.

21. Bahcall, J. N. & Pinsonneault, M. H. Standard solar models, with and without helium diffusion and the solar neutrino problem. *Rev. Mod. Phys.* **64**, 885–926 (1992). doi:10.1103/RevModPhys.64.885.

22. Hosaka, J. *et al.* Solar neutrino measurements in Super-Kamiokande-I. *Phys. Rev.* **D73**, 112001 (2006). doi:10.1103/PhysRevD.73.112001. arXiv:hep-ex/0508053.

23. Cravens, J. P. *et al.* Solar neutrino measurements in Super-Kamiokande-II. *Phys. Rev. D* **78**, 032002 (2008). doi:10.1103/PhysRevD.78.032002. arXiv:0803.4312.

24. Abe, K. *et al.* Solar neutrino results in Super-Kamiokande-III. *Phys. Rev.* **D83**, 052010 (2011). doi:10.1103/PhysRevD.83.052010. arXiv:1010.0118.

25. Abe, K. *et al.* Solar neutrino measurements in Super-Kamiokande-IV. *Phys. Rev.* **D94**, 052010 (2016). doi:10.1103/PhysRevD.94.052010. arXiv:1606.07538.

26. Nakano, Y. Latest result of solar neutrino analysis in Super-Kamiokande. *J. Phys. Conf. Ser.* **1468**, 012189 (2020). doi:10.1088/1742-6596/1468/1/012189.

27. Marti-Magro, L. SuperK-Gd: The Gd future of Super-Kamiokande. *PoS* **ICRC2019**, 957 (2020). doi:10.22323/1.358.0957.

28. Ahmad, Q. R. *et al.* Measurement of the rate of $\nu_e + d \to p + p + e^-$ interactions produced by ^{8}B solar neutrinos at the Sudbury Neutrino Observatory. *Phys. Rev. Lett.* **87**, 071301 (2001). doi:10.1103/PhysRevLett.87.071301. arXiv:nucl-ex/0106015.

29. Aharmim, B. *et al.* Electron energy spectra, fluxes, and day-night asymmetries of ^{8}B solar neutrinos from measurements with NaCl dissolved in the heavy-water detector at the Sudbury Neutrino Observatory. *Phys. Rev.* **C72**, 055502 (2005). doi:10.1103/PhysRevC.72.055502. arXiv:nucl-ex/0502021.

30. Aharmim, B. *et al.* An independent measurement of the total active ^{8}B solar neutrino flux using an array of ^{3}He proportional counters at the Sudbury Neutrino Observatory. *Phys. Rev. Lett.* **101**, 111301 (2008). doi:10.1103/PhysRevLett.101.111301. arXiv:0806.0989.

31. Aharmim, B. *et al.* Measurement of the ν_e and total ^{8}B solar neutrino fluxes with the Sudbury Neutrino Observatory phase-III data set. *Phys. Rev.* **C87**, 015502 (2013). doi:10.1103/PhysRevC.87.015502. arXiv:1107.2901.

32. Aharmim, B. *et al.* Combined analysis of all three phases of solar neutrino data from the Sudbury Neutrino Observatory. *Phys. Rev.* **C88**, 025501 (2013). doi:10.1103/PhysRevC.88.025501. arXiv:1109.0763.

33. NobelPrize.org. *The 2015 Nobel Prize in Physics - Press Release* (Nobel Media AB 2020, 2020). https://www.nobelprize.org/prizes/physics/2015/press-release/.

34. Alimonti, G. *et al.* The Borexino detector at the Laboratori Nazionali del Gran Sasso. *Nucl. Instrum. Meth.* **A600**, 568–593 (2009). doi:10.1016/j.nima.2008.11.076. arXiv:0806.2400.

35. Alimonti, G. *et al.* Science and technology of BOREXINO: A real time detector for low-energy solar neutrinos. *Astropart. Phys.* **16**, 205–234 (2002). doi:10.1016/S0927-6505(01)00110-4. arXiv:hep-ex/0012030.

36. Bellini, G. *et al.* Final results of borexino phase-I on low-energy solar neutrino spectroscopy. *Phys. Rev. D* **89**, 112007 (2014). doi:10.1103/PhysRevD.89.112007. arXiv:1308.0443.

37. Arpesella, C. *et al.* Direct measurement of the ^{7}Be solar neutrino flux with 192 days of Borexino data. *Phys. Rev. Lett.* **101**, 091302 (2008). doi:10.1103/PhysRevLett.101.091302. arXiv:0805.3843.

38. Bellini, G. *et al.* Neutrinos from the primary proton–proton fusion process in the Sun. *Nature* **512**, 383–386 (2014). doi:10.1038/nature13702.

39. Bellini, G. *et al.* First evidence of pep solar neutrinos by direct detection in Borexino. *Phys. Rev. Lett.* **108**, 051302 (2012). doi:10.1103/PhysRevLett.108.051302. arXiv:1110.3230.

40. Agostini, M. *et al.* First Simultaneous Precision Spectroscopy of pp, ^{7}Be, and pep Solar Neutrinos with Borexino Phase-II. *Phys. Rev. D* **100**, 082004 (2019). doi:10.1103/PhysRevD.100.082004. arXiv:1707.09279.

41. Agostini, M. *et al.* Experimental evidence of neutrinos produced in the CNO fusion cycle in the Sun. *Nature* **587**, 577–582 (2020). doi:10.1038/s41586-020-2934-0. arXiv:2006.15115.

42. Pontecorvo, B. Mesonium and anti-mesonium. *Sov. Phys. JETP* **6**, 429 (1957). [Zh. Eksp. Teor. Fiz.33,549(1957)].

43. Pontecorvo, B. Inverse beta processes and nonconservation of lepton charge. *Sov. Phys. JETP* **7**, 172–173 (1958).

44. Bilenky, S. M. Bruno Pontecorvo and Neutrino Oscillations. *Adv. High Energy Phys.* **2013**, 873236 (2013). doi:10.1155/2013/873236.

45. Gell-Mann, M. & Pais, A. Behavior of neutral particles under charge conjugation. *Phys. Rev.* **97**, 1387–1389 (1955). doi:10.1103/PhysRev.97.1387.

46. Lande, K., Booth, E. T., Impeduglia, J., Lederman, L. M. & Chinowsky, W. Observation of long-lived neutral particles. *Phys. Rev.* **103**, 1901–1904 (1956). doi:10.1103/PhysRev.103.1901.

47. Lande, K., Lederman, L. M. & Chinowsky, W. Report on long-lived K^0 mesons. *Phys. Rev.* **105**, 1925–1927 (1957). doi:10.1103/PhysRev.105.1925.2.

48. Muller, F. *et al.* Regeneration and mass difference of neutral K mesons. *Phys. Rev. Lett.* **4**, 418–421 (1960). doi:10.1103/PhysRevLett.4.418.

49. Maki, Z., Nakagawa, M. & Sakata, S. Remarks on the unified model of elementary particles. *Prog. Theor. Phys.* **28**, 870–880 (1962). doi:10.1143/PTP.28.870.

50. Gribov, V. & Pontecorvo, B. Neutrino astronomy and lepton charge. *Physics Letters B* **28**, 493–496 (1969). doi:10.1016/0370-2693(69)90525-5.

51. Bilenky, S. M. & Pontecorvo, B. Lepton Mixing and Neutrino Oscillations. *Phys. Rept.* **41**, 225–261 (1978). doi:10.1016/0370-1573(78)90095-9.

52. Schael, S. *et al.* Precision electroweak measurements on the *Z* resonance. *Phys. Rept.* **427**, 257–454 (2006). doi:10.1016/j.physrep.2005.12.006. arXiv:hep-ex/0509008.

53. Kim, C. & Pevsner, A. *Neutrinos in physics and astrophysics* (Harwood Academic, 1993).

54. Wolfenstein, L. Oscillations among three neutrino types and CP violation. *Phys. Rev.* **D18**, 958–960 (1978). doi:10.1103/PhysRevD.18.958.

55. Wolfenstein, L. Neutrino oscillations in matter. *Phys. Rev. D* **17**, 2369–2374 (1978). doi:10.1103/PhysRevD.17.2369.

56. Mikheev, S. P. & Smirnov, A. Y. Resonant amplification of neutrino oscillations in matter and solar-neutrino spectroscopy. *Nuovo Cimento C* **9**, 17–26 (1986). doi:10.1007/BF02508049.

57. Dighe, A. S., Liu, Q. Y. & Smirnov, A. Y. Coherence and the day-night asymmetry in the solar neutrino flux (1999). arXiv:hep-ph/9903329.

58. Meyer, M. & Zuber, K. *Solar Neutrinos* (World Scientific, 2019).

59. Esteban, I., Gonzalez-Garcia, M. C., Hernandez-Cabezudo, A., Maltoni, M. & Schwetz, T. Global analysis of three-flavour neutrino oscillations: synergies and tensions in the determination of θ_{23}, δ_{CP}, and the mass ordering. *JHEP* **01**, 106 (2019). doi:10.1007/JHEP01(2019)106. arXiv:1811.05487.

60. Dziewonski, A. & Anderson, D. Preliminary reference earth model. *Phys. Earth Planet. Interiors* **25**, 297–356 (1981). doi:10.1016/0031-9201(81)90046-7.

61. Wendell, R. *et al.* Atmospheric neutrino oscillation analysis with sub-leading effects in Super-Kamiokande I, II, and III. *Phys. Rev.* **D81**, 092004 (2010). doi:10.1103/PhysRevD.81.092004. arXiv:1002.3471.

62. Gando, A. *et al.* Constraints on θ_{13} from a three-flavor oscillation analysis of reactor antineutrinos at KamLAND. *Phys. Rev.* **D83**, 052002 (2011). doi:10.1103/PhysRevD.83.052002. arXiv:1009.4771.

63. Adamson, P. *et al.* Combined analysis of ν_μ disappearance and $\nu_\mu \to \nu_e$ appearance in MINOS using accelerator and atmospheric neutrinos. *Phys. Rev. Lett.* **112**, 191801 (2014). doi:10.1103/PhysRevLett.112.191801. arXiv:1403.0867.

64. Gonzalez-Garcia, M. C. & Nir, Y. Neutrino masses and mixing: Evidence and implications. *Rev. Mod. Phys.* **75**, 345–402 (2003). doi:10.1103/RevModPhys.75.345. arXiv:hep-ph/0202058.

65. Gonzalez-Garcia, M. C., Maltoni, M. & Schwetz, T. Updated fit to three neutrino mixing: status of leptonic CP violation. *JHEP* **11**, 052 (2014). doi:10.1007/JHEP11(2014)052. arXiv:1409.5439.

66. Giunti, C., Gonzalez-Garcia, M. C. & Pena-Garay, C. Four-neutrino oscillation solutions of the solar neutrino problem. *Phys. Rev.* **D62**, 013005 (2000). doi:10.1103/PhysRevD.62.013005. arXiv:hep-ph/0001101.

67. Spergel, D. N. & Press, W. H. Effect of hypothetical, weakly interacting, massive particles on energy transport in the solar interior. *Astrophys. J.* **294**, 663–673 (1985). doi:10.1086/163336.

68. Roulet, E. MSW effect with flavor changing neutrino interactions. *Phys. Rev.* **D44**, R935–R938 (1991). doi:10.1103/PhysRevD.44.R935.

69. Bahcall, J. N., Cabibbo, N. & Yahil, A. Are neutrinos stable particles? *Phys. Rev. Lett.* **28**, 316–318 (1972). doi:10.1103/PhysRevLett.28.316.

70. Cisneros, A. Effect of neutrino magnetic moment on solar neutrino observations. *Astrophys. Space Sci.* **10**, 87–92 (1971). doi:10.1007/BF00654607.

71. Dodelson, S., Gyuk, G. & Turner, M. S. Primordial nucleosynthesis with a decaying tau-neutrino. *Phys. Rev.* **D49**, 5068–5079 (1994). doi:10.1103/PhysRevD.49.5068. arXiv:astro-ph/9312062.

72. White, M. J., Gelmini, G. & Silk, J. Structure formation with decaying neutrinos. *Phys. Rev.* **D51**, 2669–2676 (1995). doi:10.1103/PhysRevD.51.2669. arXiv:astro-ph/9411098.

73. Beacom, J. F., Bell, N. F., Hooper, D., Pakvasa, S. & Weiler, T. J. Decay of high-energy astrophysical neutrinos. *Phys. Rev. Lett.* **90**, 181301 (2003). doi:10.1103/PhysRevLett.90.181301. arXiv:hep-ph/0211305.

74. Beacom, J. F., Bell, N. F., Hooper, D., Pakvasa, S. & Weiler, T. J. Measuring flavor ratios of high-energy astrophysical neutrinos. *Phys. Rev.* **D68**, 093005 (2003). [Erratum: Phys. Rev.D72,019901(2005)]. doi:10.1103/PhysRevD.68.093005, 10.1103/PhysRevD.72.019901. arXiv:hep-ph/0307025.

75. Maltoni, M. & Winter, W. Testing neutrino oscillations plus decay with neutrino telescopes. *JHEP* **0807**, 064 (2008). doi:10.1088/1126-6708/2008/07/064. arXiv:0803.2050.

76. Baerwald, P., Bustamante, M. & Winter, W. Neutrino decays over cosmological distances and the implications for neutrino telescopes. *JCAP* **1210**, 020 (2012). doi:10.1088/1475-7516/2012/10/020. arXiv:1208.4600.

77. Dorame, L., , O. G. & Valle, J. W. F. Invisible decays of ultra-high energy neutrinos. *Frontiers in Physics* **1**, 25 (2013). doi:10.3389/fphy.2013.00025. arXiv:1303.4891.

78. Pagliaroli, G., Palladino, A., Vissani, F. & Villante, F. Testing neutrino decay scenarios with icecube data. *Phys. Rev.* **D92**, 113008 (2015). arXiv:1506.02624.

79. Frieman, J. A., Haber, H. E. & Freese, K. Neutrino mixing, decays and supernova SN1987A. *Phys. Lett.* **B200**, 115 (1988). doi:10.1016/0370-2693(88)91120-3.

80. Berezhiani, Z. G. & Smirnov, A. Y. Matter induced neutrino decay and supernova SN1987A. *Phys. Lett.* **B220**, 279–284 (1989). doi:10.1016/0370-2693(89)90052-X.

81. Jaffe, A. H. & Turner, M. S. Gamma-rays and the decay of neutrinos from sn1987a. *Phys. Rev.* **D55**, 7951–7959 (1997). doi:10.1103/PhysRevD.55.7951. arXiv:astro-ph/9601104.

82. Lindner, M., Ohlsson, T. & Winter, W. Decays of supernova neutrinos. *Nucl. Phys.* **B622**, 429–456 (2002). doi:10.1016/S0550-3213(01)00603-4. arXiv:astro-ph/0105309.

83. Ando, S. Decaying neutrinos and implications from the supernova relic neutrino observation. *Phys. Lett.* **B570**, 11 (2003). doi:10.1016/j.physletb.2003.07.009. arXiv:hep-ph/0307169.

84. Fogli, G., Lisi, E., Mirizzi, A. & Montanino, D. Three generation flavor transitions and decays of supernova relic neutrinos. *Phys. Rev.* **D70**, 013001 (2004). doi:10.1103/PhysRevD.70.013001. arXiv:hep-ph/0401227.

85. Ando, S. Appearance of neutronization peak and decaying supernova neutrinos. *Phys. Rev.* **D70**, 033004 (2004). doi:10.1103/PhysRevD.70.033004. arXiv:hep-ph/0405200.

86. Zatsepin, G. T. & Smirnov, A. Yu. Neutrino decay in gauge theories. *Yad. Fiz.* **28**, 1569–1579 (1978).

87. Schechter, J. & Valle, J. W. F. Neutrino masses in SU(2) x U(1) theories. *Phys. Rev.* **D22**, 2227 (1980). doi:10.1103/PhysRevD.22.2227.

88. Bahcall, J. N., Petcov, S. T., Toshev, S. & Valle, J. W. F. Tests of neutrino stability. *Phys. Lett.* **B181**, 369–374 (1986). doi:10.1016/0370-2693(86)90065-1.

89. Berezhiani, Z. G. & Vysotsky, M. I. Neutrino decay in matter. *Phys. Lett.* **B199**, 281 (1987). doi:10.1016/0370-2693(87)91375-X.

90. Acker, A., Pakvasa, S. & Pantaleone, J. T. The Solar neutrino problem: Some old solutions revisited. *Phys. Rev.* **D43**, 1754–1758 (1991). doi:10.1103/PhysRevD.43.1754.

91. Acker, A., Pakvasa, S. & Pantaleone, J. T. Decaying Dirac neutrinos. *Phys. Rev.* **D45**, 1–4 (1992). doi:10.1103/PhysRevD.45.1.

92. Berezhiani, Z. G., Fiorentini, G., Moretti, M. & Rossi, A. Fast neutrino decay and solar neutrino detectors. *Z. Phys.* **C54**, 581–586 (1992). doi:10.1007/BF01559483.

93. Berezhiani, Z. G., Fiorentini, G., Rossi, A. & Moretti, M. Neutrino decay solution of the solar neutrino problem revisited. *JETP Lett.* **55**, 151–156 (1992). [Pisma Zh. Eksp. Teor. Fiz.55,159(1992)].

94. Acker, A., Joshipura, A. & Pakvasa, S. A Neutrino decay model, solar anti-neutrinos and atmospheric neutrinos. *Phys. Lett.* **B285**, 371–375 (1992). doi:10.1016/0370-2693(92)91520-J.

95. Acker, A. & Pakvasa, S. Solar neutrino decay. *Phys. Lett.* **B320**, 320–322 (1994). doi:10.1016/0370-2693(94)90663-7. arXiv:hep-ph/9310207.

96. Choubey, S., Goswami, S. & Majumdar, D. Status of the neutrino decay solution to the solar neutrino problem. *Phys. Lett.* **B484**, 73–78 (2000). doi:10.1016/S0370-2693(00)00608-0. arXiv:hep-ph/0004193.

97. Joshipura, A. S., Masso, E. & Mohanty, S. Constraints on decay plus oscillation solutions of the solar neutrino problem. *Phys. Rev.* **D66**, 113008 (2002). doi:10.1103/PhysRevD.66.113008. arXiv:hep-ph/0203181.

98. Beacom, J. F. & Bell, N. F. Do solar neutrinos decay? *Phys. Rev.* **D65**, 113009 (2002). doi:10.1103/PhysRevD.65.113009. arXiv:hep-ph/0204111.

99. Bandyopadhyay, A., Choubey, S. & Goswami, S. Neutrino decay confronts the SNO data. *Phys. Lett.* **B555**, 33–42 (2003). doi:10.1016/S0370-2693(03)00044-3. arXiv:hep-ph/0204173.

100. Pakvasa, S. & Valle, J. W. F. Neutrino properties before and after KamLAND. *Proc. Indian Natl. Sci. Acad.* **A70**, 189–222 (2004). arXiv:hep-ph/0301061.

101. Giunti, C. & Studenikin, A. Neutrino electromagnetic interactions: a window to new physics. *Rev. Mod. Phys.* **87**, 531 (2015). doi:10.1103/RevModPhys.87.531. arXiv:1403.6344.

102. Mirizzi, A., Montanino, D. & Serpico, P. D. Revisiting cosmological bounds on radiative neutrino lifetime. *Phys. Rev.* **D76**, 053007 (2007). doi:10.1103/PhysRevD.76.053007. arXiv:0705.4667.

103. Eguchi, K. *et al.* A high sensitivity search for anti-nu(e)'s from the sun and other sources at KamLAND. *Phys. Rev. Lett.* **92**, 071301 (2004). doi:10.1103/PhysRevLett.92.071301. arXiv:hep-ex/0310047.

104. Aharmim, B. *et al.* Electron antineutrino search at the Sudbury Neutrino Observatory. *Phys. Rev.* **D70**, 093014 (2004). doi:10.1103/PhysRevD.70.093014. arXiv:hep-ex/0407029.

105. Das, C. R. & Pulido, J. Improving LMA predictions with non-standard interactions: Neutrino decay in solar matter? *Phys. Rev.* **D83**, 053009 (2011). doi:10.1103/PhysRevD.83.053009. arXiv:1007.2167.

106. Raghavan, R. S., He, X.-G. & Pakvasa, S. MSW catalyzed neutrino decay. *Phys. Rev.* **D38**, 1317–1320 (1988). doi:10.1103/PhysRevD.38.1317.

107. Palomares-Ruiz, S., Pascoli, S. & Schwetz, T. Explaining lsnd by a decaying sterile neutrino. *JHEP* **0509**, 048 (2005). doi:10.1088/1126-6708/2005/09/048. arXiv:hep-ph/0505216.

108. Adamson, P. *et al.* Search for sterile neutrino mixing in the MINOS long baseline experiment. *Phys. Rev.* **D81**, 052004 (2010). doi:10.1103/PhysRevD.81.052004. arXiv:1001.0336.

109. Barger, V. D., Learned, J. G., Pakvasa, S. & Weiler, T. J. Neutrino decay as an explanation of atmospheric neutrino observations. *Phys. Rev. Lett.* **82**, 2640–2643 (1999). doi:10.1103/PhysRevLett.82.2640. arXiv:astro-ph/9810121.

110. Bandyopadhyay, A., Choubey, S. & Goswami, S. MSW mediated neutrino decay and the solar neutrino problem. *Phys. Rev.* **D63**, 113019 (2001). doi:10.1103/PhysRevD.63.113019. arXiv:hep-ph/0101273.

111. Gonzalez-Garcia, M. & Maltoni, M. Status of oscillation plus decay of atmospheric and long-baseline neutrinos. *Phys. Lett.* **B663**, 405–409 (2008). arXiv:0802.3699.

112. Aharmim, B. *et al.* Constraints on neutrino lifetime from the Sudbury Neutrino Observatory. *Phys. Rev.* **D99**, 032013 (2019). doi:10.1103/PhysRevD.99.032013. arXiv:1812.01088.

113. Abdullahi, A. & Denton, P. B. Visible Decay of Astrophysical Neutrinos at IceCube. *Phys. Rev. D* **102**, 023018 (2020). doi:10.1103/PhysRevD.102.023018. arXiv:2005.07200.

114. Bustamante, M. New limits on neutrino decay from the Glashow resonance of high-energy cosmic neutrinos (2020). arXiv:2004.06844.

115. Gomes, R. A., Gomes, A. L. G. & Peres, O. L. G. Constraints on neutrino decay lifetime using accelerator neutrino and anti-neutrino disappearance data. *Phys. Lett.* **B740**, 345–352 (2015). arXiv:1407.5640.

116. Porto-Silva, Y. P., Prakash, S., Peres, O. L. G., Nunokawa, H. & Minakata, H. Constraining visible neutrino decay at KamLAND and JUNO. *Eur. Phys. J. C* **80**, 999 (2020). doi:10.1140/epjc/s10052-020-08573-9. arXiv:2002.12134.

117. Coloma, P. & Peres, O. L. G. Visible neutrino decay at DUNE (2017). arXiv:1705.03599.

118. Chikashige, Y., Mohapatra, R. N. & Peccei, R. D. Are there real goldstone bosons associated with broken lepton number? *Phys. Lett.* **98B**, 265–268 (1981). doi:10.1016/0370-2693(81)90011-3.

119. Gelmini, G. B. & Roncadelli, M. Left-handed neutrino mass scale and spontaneously broken lepton number. *Phys. Lett.* **99B**, 411–415 (1981). doi:10.1016/0370-2693(81)90559-1.

120. Lindner, M., Ohlsson, T. & Winter, W. A Combined treatment of neutrino decay and neutrino oscillations. *Nucl. Phys.* **B607**, 326–354 (2001). doi:10.1016/S0550-3213(01)00237-1. arXiv:hep-ph/0103170.

121. Gago, A. M., Gomes, R. A., Gomes, A. L. G., Jones-Perez, J. & Peres, O. L. G. Visible neutrino decay in the light of appearance and disappearance long baseline experiments. *JHEP* **11**, 022 (2017). doi:10.1007/JHEP11(2017)022. arXiv:1705.03074.

122. Picoreti, R., Guzzo, M. M., de Holanda, P. C. & Peres, O. L. G. Neutrino decay and solar neutrino seasonal effect. *Phys. Lett.* **B761**, 70–73 (2016). doi:10.1016/j.physletb.2016.08.007. arXiv:1506.08158.

123. Picoreti, R., Guzzo, M., de Holanda, P. & Peres, O. Neutrino decay and Solar Neutrino Seasonal effect. *PoS* **ICHEP2016**, 464 (2017). doi:10.22323/1.282.0464.

124. Berryman, J. M., de Gouvêa, A., Hernández, D. & Oliviera, R. L. N. Non-Unitary neutrino propagation from neutrino decay. *Phys. Lett.* **B742**, 74–79 (2015). doi:10.1016/j.physletb.2015.01.002. arXiv:1407.6631.

125. de Holanda, P. C. & Smirnov, A. Y. LMA MSW solution of the solar neutrino problem and first KamLAND results. *JCAP* **02**, 001 (2003). doi:10.1088/1475-7516/2003/02/001. arXiv:hep-ph/0212270.

126. de Holanda, P. C. & Smirnov, A. Y. Solar neutrinos: Global analysis with day and night spectra from SNO. *Phys. Rev. D* **66**, 113005 (2002). doi:10.1103/PhysRevD.66.113005. arXiv:hep-ph/0205241.

127. de Holanda, P. C. & Smirnov, A. Y. Solar neutrinos: The SNO salt phase results and physics of conversion. *Astropart. Phys.* **21**, 287–301 (2004). doi:10.1016/j.astropartphys.2004.01.007. arXiv:hep-ph/0309299.

128. Kaether, F., Hampel, W., Heusser, G., Kiko, J. & Kirsten, T. Reanalysis of the GALLEX solar neutrino flux and source experiments. *Phys. Lett.* **B685**, 47–54 (2010). doi:10.1016/j.physletb.2010.01.030. arXiv:1001.2731.

129. An, F. P. *et al.* Spectral measurement of electron antineutrino oscillation amplitude and frequency at Daya Bay. *Phys. Rev. Lett.* **112**, 061801 (2014). doi:10.1103/PhysRevLett.112.061801. arXiv:1310.6732.

130. Smy, M. B. *et al.* Precise measurement of the solar neutrino day/night and seasonal variation in Super-Kamiokande-I. *Phys. Rev.* **D69**, 011104 (2004). doi:10.1103/PhysRevD.69.011104. arXiv:hep-ex/0309011.

131. Aharmim, B. *et al.* A Search for periodicities in the ^{8}B solar neutrino flux measured by the Sudbury neutrino observatory. *Phys. Rev.* **D72**, 052010 (2005). doi:10.1103/PhysRevD.72.052010. arXiv:hep-ex/0507079.

132. Berryman, J. M., de Gouvea, A. & Hernandez, D. Solar neutrinos and the decaying neutrino hypothesis. *Phys. Rev.* **D92**, 073003 (2015). doi:10.1103/PhysRevD.92.073003. arXiv:1411.0308.

133. Lesgourgues, J. & Pastor, S. Massive neutrinos and cosmology. *Phys. Rept.* **429**, 307–379 (2006). doi:10.1016/j.physrep.2006.04.001. arXiv:astro-ph/0603494.

134. Aghanim, N. *et al.* Planck 2018 results. VI. Cosmological parameters. *Astron. Astrophys.* **641**, A6 (2020). doi:10.1051/0004-6361/201833910. arXiv:1807.06209.

135. Chacko, Z., Dev, A., Du, P., Poulin, V. & Tsai, Y. Cosmological Limits on the Neutrino Mass and Lifetime. *JHEP* **04**, 020 (2020). doi:10.1007/JHEP04(2020)020. arXiv:1909.05275.

136. Escudero, M., Lopez-Pavon, J., Rius, N. & Sandner, S. Relaxing Cosmological Neutrino Mass Bounds with Unstable Neutrinos. *JHEP* **12**, 119 (2020). doi:10.1007/JHEP12(2020)119. arXiv:2007.04994.

137. Ade, P. A. R. *et al.* Planck 2015 results. XIII. Cosmological parameters. *Astron. Astrophys.* **594**, A13 (2016). doi:10.1051/0004-6361/201525830. arXiv:1502.01589.

138. Gando, Y. *et al.* Search for anti-nu(e) from the sun at Super-Kamiokande I. *Phys. Rev. Lett.* **90**, 171302 (2003). doi:10.1103/PhysRevLett.90.171302. arXiv:hep-ex/0212067.

139. Gando, A. *et al.* A study of extraterrestrial antineutrino sources with the KamLAND detector. *Astrophys. J.* **745**, 193 (2012). doi:10.1088/0004-637X/745/2/193. arXiv:1105.3516.

140. Bellini, G. *et al.* Study of solar and other unknown anti-neutrino fluxes with Borexino at LNGS. *Phys. Lett.* **B696**, 191–196 (2011). doi:10.1016/j.physletb.2010.12.030. arXiv:1010.0029.

141. Agostini, M. *et al.* Search for low-energy neutrinos from astrophysical sources with Borexino. *Astropart. Phys.* **125**, 102509 (2021). doi:10.1016/j.astropartphys.2020.102509. arXiv:1909.02422.

142. Zhang, H. *et al.* Supernova relic neutrino search with neutron tagging at Super-Kamiokande-IV. *Astropart. Phys.* **60**, 41–46 (2015). doi:10.1016/j.astropartphys.2014.05.004. arXiv:1311.3738.

143. Bergstrom, J. *et al.* Updated determination of the solar neutrino fluxes from solar neutrino data. *JHEP* **03**, 132 (2016). doi:10.1007/JHEP03(2016)132. arXiv:1601.00972.

144. Vinyoles, N. *et al.* A new Generation of Standard Solar Models. *Astrophys. J.* **835**, 202 (2017). doi:10.3847/1538-4357/835/2/202. arXiv:1611.09867.

145. Strumia, A. & Vissani, F. Precise quasielastic neutrino/nucleon cross-section. *Phys. Lett.* **B564**, 42–54 (2003). doi:10.1016/S0370-2693(03)00616-6. arXiv:astro-ph/0302055.

146. Viaux, N. *et al.* Particle-physics constraints from the globular cluster M5: Neutrino Dipole Moments. *Astron. Astrophys.* **558**, A12 (2013). doi:10.1051/0004-6361/201322004. arXiv:1308.4627.

147. Pehlivan, Y., Balantekin, A. B. & Kajino, T. Neutrino Magnetic Moment, CP Violation and Flavor Oscillations in Matter. *Phys. Rev.* **D90**, 065011 (2014). doi:10.1103/PhysRevD.90.065011. arXiv:1406.5489.

148. de Gouvea, A. & Shalgar, S. Effect of Transition Magnetic Moments on Collective Supernova Neutrino Oscillations. *JCAP* **1210**, 027 (2012). doi:10.1088/1475-7516/2012/10/027. arXiv:1207.0516.

149. de Gouvea, A. & Shalgar, S. Transition Magnetic Moments and Collective Neutrino Oscillations:Three-Flavor Effects and Detectability. *JCAP* **1304**, 018 (2013). doi:10.1088/1475-7516/2013/04/018. arXiv:1301.5637.

150. Miller Bertolami, M. M. Limits on the neutrino magnetic dipole moment from the luminosity function of hot white dwarfs. *Astron. Astrophys.* **562**, A123 (2014). doi:10.1051/0004-6361/201322641. arXiv:1407.1404.

151. Córsico, A. H., Althaus, L. G., Miller Bertolami, M. M., Kepler, S. O. & García-Berro, E. Constraining the neutrino magnetic dipole moment from white dwarf pulsations. *JCAP* **1408**, 054 (2014). doi:10.1088/1475-7516/2014/08/054. arXiv:1406.6034.

152. Barranco, J., Miranda, O. G., Moura, C. A. & Parada, A. A reduction in the UHE neutrino flux due to neutrino spin precession. *Phys. Lett.* **B718**, 26–29 (2012). doi:10.1016/j.physletb.2012.10.024. arXiv:1205.4285.

153. Voloshin, M. B. & Vysotsky, M. I. Neutrino Magnetic Moment and Time Variation of Solar Neutrino Flux. *Sov. J. Nucl. Phys.* **44**, 544 (1986). [Yad. Fiz.44,845(1986)].

154. Okun, L. B., Voloshin, M. B. & Vysotsky, M. I. Neutrino Electrodynamics and Possible Effects for Solar Neutrinos. *Sov. Phys. JETP* **64**, 446–452 (1986). [Zh. Eksp. Teor. Fiz.91,754(1986)].

155. Barbieri, R. & Fiorentini, G. The Solar Neutrino Puzzle and the Neutrino (L) $\rightarrow$ Neutrino (R) Conversion Hypothesis. *Nucl. Phys.* **B304**, 909–920 (1988). doi:10.1016/0550-3213(88)90661-X.

156. Schechter, J. & Valle, J. W. F. Majorana Neutrinos and Magnetic Fields. *Phys. Rev.* **D24**, 1883–1889 (1981). doi:10.1103/PhysRevD.25.283.

157. Lim, C.-S. & Marciano, W. J. Resonant Spin - Flavor Precession of Solar and Supernova Neutrinos. *Phys. Rev.* **D37**, 1368–1373 (1988). doi:10.1103/PhysRevD.37.1368.

158. Akhmedov, E. K. Resonant Amplification of Neutrino Spin Rotation in Matter and the Solar Neutrino Problem. *Phys. Lett.* **B213**, 64–68 (1988). doi:10.1016/0370-2693(88)91048-9.

159. Pulido, J. Resonant and nonresonant spin-flip flavor precession of soalr neutrinos. *Phys. Rev.* **D41**, 2956 (1990). doi:10.1103/PhysRevD.41.2956.

160. Balantekin, A. B., Hatchell, P. J. & Loreti, F. Matter Enhanced Spin Flavor Precession of Solar Neutrinos With Transition Magnetic Moments. *Phys. Rev.* **D41**, 3583 (1990). doi:10.1103/PhysRevD.41.3583.

161. Akhmedov, E. K. & Pulido, J. Solar neutrino oscillations and bounds on neutrino magnetic moment and solar magnetic field. *Phys. Lett.* **B553**, 7–17 (2003). doi:10.1016/S0370-2693(02)03182-9. arXiv:hep-ph/0209192.

162. Chauhan, B. C., Pulido, J. & Torrente-Lujan, E. KamLAND, solar anti-neutrinos and the solar magnetic field. *Phys. Rev.* **D68**, 033015 (2003). doi:10.1103/PhysRevD.68.033015. arXiv:hep-ph/0304297.

163. Balantekin, A. B. & Volpe, C. Does the neutrino magnetic moment have an impact on solar physics? *Phys. Rev.* **D72**, 033008 (2005). doi:10.1103/PhysRevD.72.033008. arXiv:hep-ph/0411148.

164. Torrente-Lujan, E. KamLAND bounds on solar anti-neutrinos and neutrino transition magnetic moments. *JHEP* **04**, 054 (2003). doi:10.1088/1126-6708/2003/04/054. arXiv:hep-ph/0302082.

165. Miranda, O. G., Rashba, T. I., Rez, A. I. & Valle, J. W. F. Constraining the neutrino magnetic moment with anti-neutrinos from the sun. *Phys. Rev. Lett.* **93**, 051304 (2004). doi:10.1103/PhysRevLett.93.051304. arXiv:hep-ph/0311014.

166. Miranda, O. G., Rashba, T. I., Rez, A. I. & Valle, J. W. F. Enhanced solar anti-neutrino flux in random magnetic fields. *Phys. Rev.* **D70**, 113002 (2004). doi:10.1103/PhysRevD.70.113002. arXiv:hep-ph/0406066.

167. Dicke, R. H. A Magnetic Core in the Sun - the Solar Rotator. *Solar Physics* **78**, 3–16 (1982). doi:10.1007/BF00151138.

168. Semikoz, V. & Torrente-Lujan, E. Neutrino conversions in solar random magnetic fields. *Nucl. Phys.* **B556**, 353–372 (1999). doi:10.1016/S0550-3213(99)00352-1. arXiv:hep-ph/9809376.

169. Friedland, A. Do solar neutrinos probe neutrino electromagnetic properties? (2005). arXiv:hep-ph/0505165.

170. Fan, Y. Magnetic fields in the solar convection zone. *Living Reviews in Solar Physics* **1**, 1 (2004). doi:10.12942/lrsp-2004-1.

171. Brun, A. S., Miesch, M. S. & Toomre, J. Global-Scale Turbulent Convection and Magnetic Dynamo Action in the Solar Envelope. *Astrophys. J.* **614**, 1073 (2004). doi:10.1086/423835. arXiv:astro-ph/0610073.

172. Zwicky, F. Die Rotverschiebung von extragalaktischen Nebeln. *Helv. Phys. Acta* **6**, 110–127 (1933). [Gen. Rel. Grav.41,207(2009)]. doi:10.1007/s10714-008-0707-4.

173. Rubin, V. C. & Ford, W. K., Jr. Rotation of the Andromeda Nebula from a Spectroscopic Survey of Emission Regions. *Astrophys. J.* **159**, 379–403 (1970). doi:10.1086/150317.

174. Rubin, V. C., Thonnard, N. & Ford, W. K., Jr. Rotational properties of 21 SC galaxies with a large range of luminosities and radii, from NGC 4605 /R = 4kpc/ to UGC 2885 /R = 122 kpc/. *Astrophys. J.* **238**, 471 (1980). doi:10.1086/158003.

175. Refregier, A. Weak gravitational lensing by large scale structure. *Ann. Rev. Astron. Astrophys.* **41**, 645–668 (2003). doi:10.1146/annurev.astro.41.111302.102207. arXiv:astro-ph/0307212.

176. Clowe, D. *et al.* A direct empirical proof of the existence of dark matter. *Astrophys. J.* **648**, L109–L113 (2006). doi:10.1086/508162. arXiv:astro-ph/0608407.

177. Asztalos, S. J., Rosenberg, L. J., van Bibber, K., Sikivie, P. & Zioutas, K. Searches for astrophysical and cosmological axions. *Ann. Rev. Nucl. Part. Sci.* **56**, 293–326 (2006). doi:10.1146/annurev.nucl.56.080805.140513.

178. Dodelson, S. & Widrow, L. M. Sterile-neutrinos as dark matter. *Phys. Rev. Lett.* **72**, 17–20 (1994). doi:10.1103/PhysRevLett.72.17. arXiv:hep-ph/9303287.

179. Feng, J. L. Dark Matter Candidates from Particle Physics and Methods of Detection. *Ann. Rev. Astron. Astrophys.* **48**, 495–545 (2010). doi:10.1146/annurev-astro-082708-101659. arXiv:1003.0904.

180. Jungman, G., Kamionkowski, M. & Griest, K. Supersymmetric dark matter. *Phys. Rept.* **267**, 195–373 (1996). doi:10.1016/0370-1573(95)00058-5. arXiv:hep-ph/9506380.

181. Gildener, E. Gauge Symmetry Hierarchies. *Phys. Rev.* **D14**, 1667 (1976). doi:10.1103/PhysRevD.14.1667.

182. Weinberg, S. Gauge Hierarchies. *Phys. Lett.* **82B**, 387–391 (1979). doi:10.1016/0370-2693(79)90248-X.

183. Goodman, J. *et al.* Constraints on Dark Matter from Colliders. *Phys. Rev.* **D82**, 116010 (2010). doi:10.1103/PhysRevD.82.116010. arXiv:1008.1783.

184. Akerib, D. S. *et al.* First results from the cryogenic dark matter search in the Soudan Underground Lab. *Phys. Rev. Lett.* **93**, 211301 (2004). doi:10.1103/PhysRevLett.93.211301. arXiv:astro-ph/0405033.

185. Ahmed, Z. *et al.* Search for Weakly Interacting Massive Particles with the First Five-Tower Data from the Cryogenic Dark Matter Search at the Soudan Underground Laboratory. *Phys. Rev. Lett.* **102**, 011301 (2009). doi:10.1103/PhysRevLett.102.011301. arXiv:0802.3530.

186. Ahmed, Z. *et al.* Dark Matter Search Results from the CDMS II Experiment. *Science* **327**, 1619–1621 (2010). doi:10.1126/science.1186112. arXiv:0912.3592.

187. Agnese, R. *et al.* Search for Low-Mass Weakly Interacting Massive Particles with SuperCDMS. *Phys. Rev. Lett.* **112**, 241302 (2014). doi:10.1103/PhysRevLett.112.241302. arXiv:1402.7137.

188. Angle, J. *et al.* First Results from the XENON10 Dark Matter Experiment at the Gran Sasso National Laboratory. *Phys. Rev. Lett.* **100**, 021303 (2008). doi:10.1103/PhysRevLett.100.021303. arXiv:0706.0039.

189. Aprile, E. *et al.* The XENON100 Dark Matter Experiment. *Astropart. Phys.* **35**, 573–590 (2012). doi:10.1016/j.astropartphys.2012.01.003. arXiv:1107.2155.

190. Aprile, E. *et al.* XENON100 Dark Matter Results from a Combination of 477 Live Days. *Phys. Rev.* **D94**, 122001 (2016). doi:10.1103/PhysRevD.94.122001. arXiv:1609.06154.

191. Aprile, E. The XENON1T Dark Matter Search Experiment. *Springer Proc. Phys.* **148**, 93–96 (2013). doi:10.1007/978-94-007-7241-0_14. arXiv:1206.6288.

192. Aprile, E. *et al.* First Dark Matter Search Results from the XENON1T Experiment. *Phys. Rev. Lett.* **119**, 181301 (2017). doi:10.1103/PhysRevLett.119.181301. arXiv:1705.06655.

193. Hooper, D. Particle Dark Matter. In *Proceedings of Theoretical Advanced Study Institute in Elementary Particle Physics on The dawn of the LHC era (TASI 2008): Boulder, USA, June 2-27, 2008*, 709–764 (2010). arXiv:0901.4090.

194. Gaisser, T. K. *Cosmic rays and particle physics* (Cambridge University Press, 1991).

195. Malkov, M. & Drury, L. O. Nonlinear theory of diffusive acceleration of particles by shock waves. *Rept. Prog. Phys.* **64**, 429–481 (2001). doi:10.1088/0034-4885/64/4/201.

196. Strong, A. W., Moskalenko, I. V. & Ptuskin, V. S. Cosmic-ray propagation and interactions in the Galaxy. *Ann. Rev. Nucl. Part. Sci.* **57**, 285–327 (2007). doi:10.1146/annurev.nucl.57.090506.123011. arXiv:astro-ph/0701517.

197. Potgieter, M. Solar Modulation of Cosmic Rays. *Living Rev. Solar Phys.* **10**, 3 (2013). doi:10.12942/lrsp-2013-3. arXiv:1306.4421.

198. Adriani, O. *et al.* PAMELA Measurements of Cosmic-ray Proton and Helium Spectra. *Science* **332**, 69–72 (2011). doi:10.1126/science.1199172. arXiv:1103.4055.

199. Yoon, Y. S. *et al.* Proton and Helium Spectra from the CREAM-III Flight. *Astrophys. J.* **839**, 5 (2017). doi:10.3847/1538-4357/aa68e4. arXiv:1704.02512.

200. Antoni, T. *et al.* KASCADE measurements of energy spectra for elemental groups of cosmic rays: Results and open problems. *Astropart. Phys.* **24**, 1–25 (2005). doi:10.1016/j.astropartphys.2005.04.001. arXiv:astro-ph/0505413.

201. Aab, A. *et al.* The Pierre Auger Cosmic Ray Observatory. *Nucl. Instrum. Meth.* **A798**, 172–213 (2015). doi:10.1016/j.nima.2015.06.058. arXiv:1502.01323.

202. Moskalenko, I. V., Karakula, S. & Tkaczyk, W. The Sun as the source of VHE neutrinos. *Astron. Astrophys.* **248**, L5–L6 (1991).

203. Seckel, D., Stanev, T. & Gaisser, T. K. Signatures of cosmic-ray interactions on the solar surface. *Astrophys. J.* **382**, 652–666 (1991). doi:10.1086/170753.

204. Moskalenko, I. V. & Karakula, S. Very high-energy neutrinos from the sun. *J. Phys.* **G19**, 1399–1406 (1993). doi:10.1088/0954-3899/19/9/019.

205. Ingelman, G. & Thunman, M. High-energy neutrino production by cosmic ray interactions in the sun. *Phys. Rev.* **D54**, 4385–4392 (1996). doi:10.1103/PhysRevD.54.4385. arXiv:hep-ph/9604288.

206. Hettlage, C., Mannheim, K. & Learned, J. G. The Sun as a high-energy neutrino source. *Astropart. Phys.* **13**, 45–50 (2000). doi:10.1016/S0927-6505(99)00120-6. arXiv:astro-ph/9910208.

207. Fogli, G. L., Lisi, E., Mirizzi, A., Montanino, D. & Serpico, P. D. Oscillations of solar atmosphere neutrinos. *Phys. Rev.* **D74**, 093004 (2006). doi:10.1103/PhysRevD.74.093004. arXiv:hep-ph/0608321.

208. Argüelles, C. A., de Wasseige, G., Fedynitch, A. & Jones, B. J. P. Solar Atmospheric Neutrinos and the Sensitivity Floor for Solar Dark Matter Annihilation Searches. *JCAP* **1707**, 024 (2017). doi:10.1088/1475-7516/2017/07/024. arXiv:1703.07798.

209. Ng, K. C. Y., Beacom, J. F., Peter, A. H. G. & Rott, C. Solar Atmospheric Neutrinos: A New Neutrino Floor for Dark Matter Searches. *Phys. Rev.* **D96**, 103006 (2017). doi:10.1103/PhysRevD.96.103006. arXiv:1703.10280.

210. Edsjo, J., Elevant, J., Enberg, R. & Niblaeus, C. Neutrinos from cosmic ray interactions in the Sun. *JCAP* **1706**, 033 (2017). doi:10.1088/1475-7516/2017/06/033. arXiv:1704.02892.

211. Masip, M. High energy neutrinos from the Sun. *Astropart. Phys.* **97**, 63–68 (2018). doi:10.1016/j.astropartphys.2017.11.003. arXiv:1706.01290.

212. Lipari, P. Lepton spectra in the earth's atmosphere. *Astropart. Phys.* **1**, 195–227 (1993). doi:10.1016/0927-6505(93)90022-6.

Appendix A

Unfinished Work

Besides solar neutrino decay, three other phenomena were studied: i) the interaction of neutrinos with solar magnetic fields through a hypothetical non-zero transition magnetic moment as a secondary effect on solar neutrino propagation; ii) the production of neutrinos from the annihilation of dark matter inside the Sun and their oscillation into a sterile flavor; and iii) neutrino production by cosmic rays interacting in the solar matter as background for detecting neutrinos from dark matter annihilations.

A.1 Solar Neutrino Spin-Flavor Precession

The massive nature of neutrinos also opens a door for these particles to have non-zero electric and/or magnetic moments. The consequences of a hypothetical neutrino magnetic moment have been investigated for a variety of astrophysical phenomena: in the formation of stars in globular clusters [146], in dense astrophysical environments [147] such as type-II supernovae [148, 149], in the luminosity and pulsation of white dwarf stars [150, 151], and even in ultra-high energy neutrino source such as gamma-ray bursts (GRB) and active galactic nuclei (AGN) [152].

In fact, shortly after the publication of the first Homestake results [12], one of the first models proposed to explain the SNP relied on the coupling of the neutrino magnetic moment to solar magnetic fields [70]. In this model, the interaction with the magnetic fields would lead to the spin-precession of left-handed neutrinos into right-handed neutrinos. Right-handed neutrinos do not participate in weak interactions and hence would not be detected if neutrinos were Dirac particles [153–155]. On the other hand [156], if neutrinos were Majorana particles, transition between neutrinos of a given family into antineutrinos of the other families — e.g., $\nu_e \to \bar{\nu}_\mu/\bar{\nu}_\tau$ — would also be possible. Soon it would be noted [157–160] that the combined effect of interactions with matter and magnetic fields would give rise to resonant transitions, similarly to the MSW effect, later called the Resonant Spin-Flavor Precession.

The interaction of neutrinos with the solar magnetic field can, in principle, happen both in the radiative zone [161–163] and in the convective zone [164–166]. The radiative zone lacks internal motions that would give rise to large scale magnetic fields, which, if present, are supposed to be smooth and frozen into the stationary plasma [167]. In the convective zone, on the other hand, the convective movement of the solar plasma give rise to turbulent magnetic fields, which, in turn, cause the plethora of phenomena in the surface of the Sun, such as sunspots. While the mean magnetic field over the solar disc is of the order of 1G, it can be three orders of magnitude higher in the sunspots. Magnetohydrodynamics models explains these magnetic fields as being produced by a dynamo mechanism at the bottom of the convective zone. [168–171].

Even though this phenomenon is currently ruled-out as a primary effect, the spin-flavor precession can still be investigated as a non-leading effect on the propagation of solar neutrinos. Since this phenomenon would lead to the production of antineutrinos, its possible to set upper limits to the neutrino magnetic moment by comparing the expected fluxes to solar electron antineutrino flux limits.

A.2 Neutrinos from Dark Matter Annihilation

Dark matter, a cold non-barionic kind of matter, is an essential ingredient in the current cosmological standard model. The existence of this exotic kind of matter was first evidenced at the measurement of the anomalous rotation curves of galaxies [172–174]. As new phenomena, such as gravitational lensing [175, 176] and others were discovered, the gravitational and cosmological data in favour dark matter became overwhelming. However, such data do not provide information on the nature and properties of the particles that constitute dark matter. Over the years, several models have been proposed as candidates for dark matter, such as weakly interacting massive particles (WIMPs), axions [177] and sterile neutrinos [178], among others [179].

WIMPs are supposed to have masses along the GeV to TeV range and tree-level interactions with $W^{\pm}$ and Z_0 bosons and are found in a variety of particle physics models, such as Supersymmetry [180]. WIMPs are one of the most studied candidates for a Dark Matter particles because of the so-called “WIMP Miracle": during the evolution of the early Universe, stable WIMPS are naturally produced with the appropriate relic density to account for the gravitational effect of dark matter, while also providing a solution to the Gauge Hierarchy Problem, the discrepancy between the Higgs boson mass and the Planck mass scale [181, 182].

WIMPS, for their weakly interacting nature, provide several opportunities for their detection. Besides the production expected in particle colliders [183], there are two other possible methods for their detection in astrophysical environments. While orbiting around the Milky Way, Sun and Earth are constantly moving through the galactic dark matter halo. Dark matter particles have a small probability of weakly interacting with ordinary matter. Hence, the elastic scattering of nuclei by dark matter particles can be used as a probe and constrain their properties such as their mass and interaction cross-sections. This is called a direct detection and several experiments have been design for this purpose such as CDMS [184–187], XENON [188–192] and others.

On the other hand, the indirect detection of dark matter particles relies on the detection of ordinary matter produced by the annihilation of dark matter particles, including photons, neutrinos, and charged particles. For the annihilation to occur, it is necessary that the DM particles accumulate in high density regions. For example, dark matter particles traversing the Sun will eventually interact with ordinary matter, losing enough energy to be gravitationally trapped. As the dark matter density rises in the core, annihilation rate also rises. Annihilation products are mostly all absorbed except for neutrinos that can propagate outwards and be detected on Earth. As such, neutrinos are a particularly interesting probe for the indirect detection of dark matter.

Neutrinos can be generated in a variety of DM annihilation channels depending on the WIMP model. Heavy quarks, tau leptons, gauge bosons, Higgs bosons generate neutrinos in a continuous spectrum upon decay, whereas direct DM annihilation into neutrinos is also possible and generate monochromatic spectra [193]. Once they are produced in the annihilation of DM particles, they propagate outwards through the solar matter and interplanetary space before arriving on Earth, where they could be detected.

As such, the detection of such neutrinos could provide information on the specifics of the DM model, e.g., the particle's mass or their annihilation cross-section, or their non-detection could be a problem for WIMP models. However, these DM neutrinos could also, in principle, not be detected because they oscillate into sterile species.

Preliminary results from this work were presented at the 33$^{\text{rd}}$ Brazilian National Meeting on Particles and Fields (XXXIII Encontro Nacional de Física de Partículas e Campos), August 27$^{\text{th}}$–31$^{\text{st}}$, 2012.

A.3 Solar Atmosphere Neutrinos

Cosmic Rays (CR) are charged particles — mainly protons — produced and accelerated in astrophysical phenomena [194]. Most of these particles have their origin in the Milky Way and are accelerated by shock waves produced by the expansion of supernova remnants [195], propagating during millions of years in the interstellar medium under influence of the galactic magnetic fields [196] before escaping the Galaxy. The incidence of this particles in the solar system is approximately isotropic and, at low energies, are modulated by the solar activity [197] due to their interaction with the solar winds and magnetic fields.

The measurement of the spectrum of cosmic rays incident upon Earth's upper atmosphere is possible by direct methods up energies of the order of TeV [198, 199]. At higher energies, the lower CR flux requires the spectrum to be inferred by the measurement of the so-called air-showers — cascades of particles produced in the CR interaction with the atoms in the atmosphere — by ground experiments [200, 201]. Atmospheric neutrinos [] are produced in these cosmic ray interactions from weakly decaying mesons.

Similarly, the incidence of cosmic rays in the Sun and their interaction with the solar matter will also produce neutrinos [202–207], often called Solar Atmosphere Neutrinos (SAν). These high energy neutrinos are considered to be a fixed background for the indirect detection of dark matter, setting a "Sensitivity Floor" [208–211] for neutrino telescopes.

We aimed at finding an semi-analytical approximation for the transport of CR particles in the solar matter analogous to the typical analytical approximation describing the CR transport on Earth's atmosphere and the production of atmospheric neutrinos [194, 212].

Preliminary results from this work were presented at the 35$^{\text{th}}$ Brazilian National Meeting on Particles and Fields (XXXV Encontro Nacional de Física de Partículas e Campos), August 15$^{\text{th}}$–19$^{\text{th}}$, 2014. This work was idealized and partially performed under supervision of Dr. Julia Tjus during the sandwich PhD period at Ruhr-Universität Bochum, Germany.

Appendix B

Published Work

The results presented in Chapter 4 were published [122] and included in the following pages.

R. Picoreti, M. M. Guzzo, P. C. de Holanda, O. L. G. Peres
Neutrino decay and solar neutrino seasonal effect
Phys. Lett. B761, 70–73 (2016)
doi:10.1016/j.physletb.2016.08.007
arXiv:1506.08158

Abstract
We consider the possibility of solar neutrino decay as a sub-leading effect on their propagation between production and detection. Using current oscillation data, we set a new lower bound to the ν_2 neutrino lifetime at $\tau_2/m_2 \geq 7.2 \times 10^{-4}\,\mathrm{s}\cdot\mathrm{eV}^{-1}$, at 99% C.L.. Also, we show how seasonal variations in the solar neutrino data can give interesting additional information about neutrino lifetime.

Physics Letters B 761 (2016) 70–73

Contents lists available at ScienceDirect

Physics Letters B

www.elsevier.com/locate/physletb

Neutrino decay and solar neutrino seasonal effect

R. Picoreti [a,*], M.M. Guzzo [a], P.C. de Holanda [a], O.L.G. Peres [a,b]

[a] Instituto de Física Gleb Wataghin – UNICAMP, 13083-859, Campinas SP, Brazil
[b] The Abdus Salam International Centre for Theoretical Physics, Strada Costiera 11, 34014 Trieste, Italy

ARTICLE INFO

Article history:
Received 13 November 2015
Received in revised form 12 June 2016
Accepted 5 August 2016
Available online 9 August 2016
Editor: S. Dodelson

ABSTRACT

We consider the possibility of solar neutrino decay as a sub-leading effect on their propagation between production and detection. Using current oscillation data, we set a new lower bound to the ν_2 neutrino lifetime at $\tau_2/m_2 \geq 7.2 \times 10^{-4}$ s.eV^{-1} at 99% C.L. Also, we show how seasonal variations in the solar neutrino data can give interesting additional information about neutrino lifetime.

1. Introduction

Beyond any reasonable doubt, it is now established that neutrinos have non-zero, non-degenerate masses. Thus, it would be possible — if not mandatory — for them to decay into other particles.

Although neutrino decay is now ruled out as a leading process [1] in the so-called Solar Neutrino Problem (SNP) — the difference between the expected solar neutrino flux produced in nuclear fusion processes in the Sun and the detected flux on Earth — one can investigate this phenomenon as a sub-leading effect in the propagation of solar neutrinos and set limits to their lifetime using the most recent experimental data.

Solar neutrinos are produced in the nuclear fusion processes that power the Sun. In such processes, Hydrogen nuclei are converted into Helium through several intermediate reactions, some of which produce neutrinos in very particular spectra — both continuous and monochromatic.

Over the years, several experiments were developed for the detection of solar neutrinos at different energy ranges. From the pioneer Homestake [2] chlorine experiment — which first hinted at the SNP — through the gallium experiments GALLEX [3], SAGE [4] and GNO [5] to the water Cherenkov detectors Kamiokande, SuperKamiokande [6] and SNO [7]. Most recently, the Borexino [8] experiment measured the so called ^{7}Be neutrino line.

The LMA-MSW solution — Large Mixing Angle flavor oscillation with Mikheyev–Smirnov–Wolfenstein (MSW) resonant flavor conversion — established the scenario of three massive light neutrinos that mix [9] in combination with the measurement of the other oscillation parameters by experiments designed for atmospheric, reactor and long-baseline neutrinos. With such precise measurements of the standard oscillation parameters, it is possible to investigate new phenomena such as the neutrino decay scenario: $\nu' \to \nu + X$.

For solar neutrinos, the decay of the mass-eigenstate ν_2 into the lighter state ν_1 is disfavored by the data and the current bound to ν_2 lifetime for invisible non-radiative decays [1] is $\tau_2/m_2 \geq 8.7 \times 10^{-5}$ s.eV^{-1} at 99% C.L. Most recently, Ref. [10] argues for $\tau_2/m_2 \geq 7.1 \times 10^{-4}$ s.eV^{-1} at 2σ.

Similarly, from the combined accelerator and atmospheric neutrino data the lifetime of the ν_3 eigenstate is $\tau_3/m_3 \geq 2.9 \times 10^{-10}$ s.eV^{-1} at 90% C.L. [11] and an analysis of the long-baseline experiments MINOS and T2K gives a combined limit of $\tau_3/m_3 \geq 2.8 \times 10^{-12}$ s.eV^{-1} at 90% C.L. [12].

In this work, we consider the decay scenario in which all the final products are invisible. We combine the available solar neutrino data with KamLAND [13] and Daya Bay [14] data. For both experiments the effect of neutrino decay is minimum, allowing us to constrain the standard neutrino mixing parameters independently of the decay parameter τ_2/m_2 and leading us to obtain a robust bound on ν_2 lifetime. Additionally, we show how seasonal variations in the solar neutrino data, which are enhanced by neutrino decay, can give some interesting information about neutrino lifetime.

2. Formalism

After production in the solar core, neutrinos propagate outwards undergoing flavor oscillation and resonant flavor transition due to the solar matter potential. After emerging from the Sun, they travel across the interplanetary medium until they reach the

* Corresponding author.
E-mail address: picoreti@ifi.unicamp.br (R. Picoreti).

http://dx.doi.org/10.1016/j.physletb.2016.08.007

Earth's surface where they can be detected either promptly or after traversing Earth's matter — on which they may also be subject to matter effects.

The transition amplitude for an electron neutrino produced in the Sun to be detected on Earth as a neutrino of flavor α, $\nu_e \to \nu_\alpha$, for the standard case of neutrino oscillations with MSW effect, can be written as [15]

$$A_{e\alpha} = \sum A^{\odot}_{ei} A^{\rm vac}_{ii} A^{\oplus}_{i\alpha}\,, \tag{1}$$

where $A^{\odot}_{ei}$ is the transition amplitude of an electron neutrino produced in the solar core to be in a ν_i mass-eigenstate in the solar surface, $A^{\rm vac}_{ii}$ is the transition amplitude for the propagation between Sun and Earth surfaces, and $A^{\oplus}_{i\alpha}$ is the transition amplitude of a ν_i to be in a ν_α state upon detection on Earth.

The transition probability is given as $P(\nu_e \to \nu_\alpha) = |A_{e\alpha}|^2$. In the LMA parameter region one can neglect coherence effects [16] and simply write the incoherent sum of probabilities:

$$P(\nu_e \to \nu_\alpha) = \sum_i P^{\odot}_{ei} P^{\oplus}_{i\alpha}\,, \tag{2}$$

where $P^{\odot}_{ei} = |A^{\odot}_{ei}|^2$ is the probability of the produced ν_e to be found as a ν_i at the surface of the Sun, and $P^{\oplus}_{i\alpha} = |A^{\oplus}_{i\alpha}|^2$ is the probability of a ν_i to be detected as a ν_α on Earth.

Considering the current limits to their lifetime, neutrinos do not decay inside the Sun and it is sufficient to consider their decay on their way to Earth. The survival probability for the invisible decay of a neutrino mass-eigenstate i, with energy E_ν, after propagating a distance L, is

$$P^{\rm surv}_{\rm i} = \exp\left[-\left(\frac{\alpha_i}{E_\nu}\right) L\right]\,, \text{ with } \alpha_i = \frac{m_i}{\tau_i}\,, \tag{3}$$

where m_i is the eigenstate mass, τ_i is the eigenstate lifetime and L is the Sun–Earth distance.

For the assumption that only the ν_2 mass-eigenstate is unstable, the electron neutrino survival probability including decay and oscillation for three neutrino families is

$$P(\nu_e \to \nu_e) = c^4_{13}\left[P^{\odot}_{e1} P^{\oplus}_{1e} + P^{\odot}_{e2}\left(P^{\rm surv}_2\right) P^{\oplus}_{2e}\right] + s^4_{13}\,, \tag{4}$$

where $s_{ij} = \sin\theta_{ij}$ and $c_{ij} = \cos\theta_{ij}$ and $P^{\rm surv}_{\rm i}$ is given in Eq. (3) and $P^{\odot}_{ei}$ and $P^{\oplus}_{ie}$ are the probabilities in Eq. (2). One interesting consequence of this scenario is that the sum over all probabilities is not equal to 1, as explicitly we have

$$\sum_{\alpha=e,\mu,\tau} P(\nu_e \to \nu_\alpha) = 1 - c^2_{13} P^{\odot}_{e2}\left(1 - P^{\rm surv}_2\right)\,. \tag{5}$$

This non-unitary evolution was discussed in Ref. [17].

Another important consequence is that, for appreciable values of τ_2/m_2, the solar neutrino data can be explained by a combination of standard three neutrino MSW oscillation and decay, which leads to a degenerescence between neutrino parameters, specially Δm^2_{21} and τ_2/m_2 [1].

3. Analysis and results

For the analysis of ν_2 decay over the Earth–Sun distance and how it affects the expected rate for each solar neutrino experiment, we calculate the neutrino survival probabilities as shown in Eq. (4) and Eq. (5), numerically, under the assumption of adiabatic evolution inside the Sun [18]. Then, we compute the expected event rate for each relevant experiment and compare it to their data.

We include Homestake total rate [2], GALLEX and GNO combined total rate [19], SAGE total rate [4], SuperKamiokande I full energy and zenith spectrum [20], SNO combined analysis [7] and Borexino 192-day low-energy data [21]. Then, we build a χ^2 function as a function of the relevant parameters $\chi^2_{\odot} = \chi^2_{\odot}(\tan^2\theta_{12}, \Delta m^2_{21}, \sin^2\theta_{13}, \tau_2/m_2)$.

We can add complementary information from the reactor experiments KamLAND [13] and Daya Bay [14] and their detection of $\bar{\nu}_e$ oscillations. One important point that led us toward this analysis is the fact that these experiments give precise constraints on Δm^2_{21} and $\sin^2\theta_{13}$. KamLAND and Daya Bay have typical baselines of $L/E_\nu \sim 10^{-10}$ s.eV^{-1} and $\sim 10^{-12}$ s.eV^{-1} respectively. For the currently allowed values of τ_2/m_2, one has that $P^{\rm surv}_i \sim 1$, which implies that, in the context of these experiments, decay can be neglected and the relevant neutrino probability is the standard three neutrino expression

$$P(\bar{\nu}_e \to \bar{\nu}_e) = 1 - c^4_{13} S^2_{12} \sin^2\Delta_{21} - S^2_{13}\sin^2\Delta m^2_{ee}\,, \tag{6}$$

where $S_{ij} = \sin 2\theta_{ij}$, $\Delta_{ij} = \Delta m^2_{ij}/4E_\nu$ and $\Delta m^2_{ij} \equiv m^2_i - m^2_j$, and we define an effective mass square difference $\sin^2\Delta m^2_{ee} \equiv c^2_{12}\sin^2\Delta_{31} + s^2_{12}\sin^2\Delta_{32}$.

This implies that the standard neutrino analysis for three neutrinos of KamLAND and Daya Bay experiments can also be used for decay scenario. In other words, we can identify $\chi^2_{\rm decay} = \chi^2_{\rm no\ decay}$ in our analysis for both experiments.

For the KamLAND experiment, a $\chi^2_{\rm KL}$ function for the standard three neutrino scenario used in Ref. [13] is available in table format as a function of $\tan^2\theta_{12}$, Δm^2_{21} and $\sin^2\theta_{13}$. For the Daya Bay experiment, the $\chi^2_{\rm DB}$ function is available in table format provided in the supplementary material from Ref. [14] as a function of Δm^2_{ee} and $\sin^2\theta_{13}$.

Then, we write the combined χ^2 function for solar, KamLAND and Daya Bay data as

$$\begin{aligned}\chi^2 = {} & \chi^2_{\odot}(\tan^2\theta_{12}, \Delta m^2_{21}, \sin^2\theta_{13}, \tau_2/m_2) + \\ & + \chi^2_{\rm KL}(\tan^2\theta_{12}, \Delta m^2_{21}, \sin^2\theta_{13}) + \\ & + \chi^2_{\rm DB}(\Delta m^2_{ee}, \sin^2\theta_{13})\,,\end{aligned} \tag{7}$$

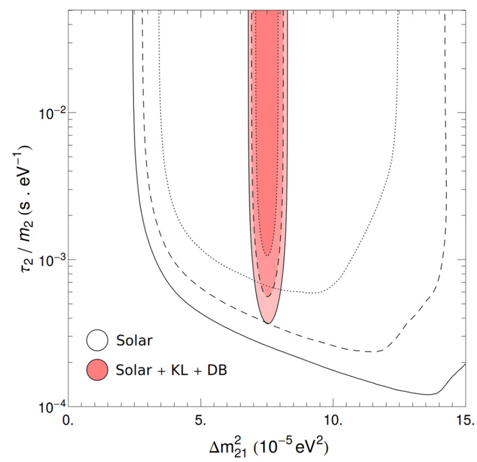

Fig. 1. Allowed regions for the decay parameter τ_2/m_2 and the mass squared difference Δm^2_{21}. The hollow curves represent the analysis with only solar neutrino data and the filled curves represent the combined analysis of solar, KamLAND and Daya Bay data. The dotted, dashed and continuous lines represent respectively 90% C.L., 99% C.L. and 99.9% C.L.

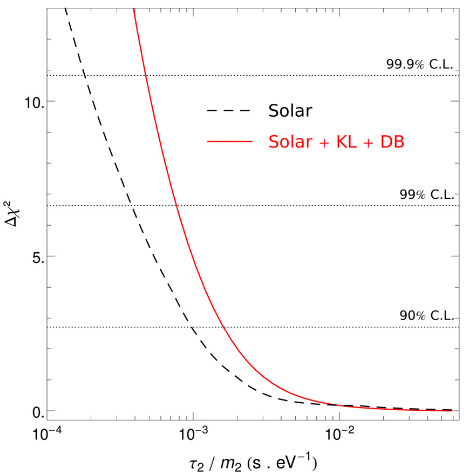

Fig. 2. $\Delta\chi^2$ for ν_2 lifetime τ_2/m_2. The dashed (continuous) curve shows the solar (combined) neutrino data analysis.

where Δm^2_{ee} was defined before and over which we can promptly marginalize the χ^2. From Eq. (7), we find the allowed regions for independent parameters $\tan^2\theta_{12}$, $\sin^2\theta_{13}$, Δm^2_{21}, and τ_2/m_2. By marginalizing over the first two, we obtain the allowed region for the mass squared difference Δm^2_{21} and the decay parameter τ_2/m_2 as shown in Fig. 1, where the hollow (filled) regions show the results for the solar neutrino (combined) analysis.

The degenerescence between Δm^2_{21} and τ_2/m_2 is evident in the hollow regions of Fig. 1, where higher values for Δm^2_{21} are allowed alongside lower values for τ_2/m_2 and lower values for Δm^2_{21} are allowed alongside higher values for τ_2/m_2.

High values of Δm^2_{21} are ruled out in the standard neutrino scenario because it leads to spectral distortions that are disfavored by the solar neutrino data. On the other hand, high values of Δm^2_{21} could become a viable solution at the cost of having lower values of τ_2/m_2. The inclusion of KamLAND and Daya Bay data breaks this degenerescence due to their precise independent measurement of Δm^2_{21} and $\sin^2\theta_{13}$ respectively.

We can now precisely isolate the contribution of the decay parameter τ_2/m_2. The complete marginalization over the standard parameters results in the curve shown in Fig. 2 of $\Delta\chi^2$ as a function of τ_2/m_2. From it, we can extract a lower limit to the ν_2 eigenstate lifetime

$$\tau_2\,/\,m_2 \geq 7.7\times 10^{-4}\ \mathrm{s\,.\,eV^{-1}},\ \text{at 99\% C.L.}, \tag{8}$$

which corresponds to an upper bound to the decay parameter $\alpha_2 \leq 8.5\times 10^{-13}$ eV^2.

4. Seasonal effect

One interesting consequence of the decay scenario that has not been discussed recently is its effect in the seasonal variation of solar neutrino flux. In the absence of decay, the neutrino flux arriving on Earth is given by $\phi^{\oplus}_{\nu} = \phi^{\odot}_{\nu}/(4\pi r^2)$, where $r = r(t)$ is the time-dependent Earth–Sun distance. The ratio between maximum (at perihelion) and minimum (at aphelion) fluxes is $R_0 = (1+\epsilon_0)^2/(1-\epsilon_0)^2$, where $\epsilon_0 = 0.0167$ is the eccentricity of Earth's orbit.

The inclusion of decay modifies the ratio between maximum and minimum neutrino fluxes and hence also the measured eccentricity ϵ as given by

Table 1
Experimental best-fit values and errors for Earth's orbital eccentricity ϵ for different solar neutrino experiments. We also show the ratio between the fitted values and Earth's eccentricity ϵ_0.

Experiment	$\epsilon_{exp} \pm \sigma_{exp}$	$(\epsilon_{exp} \pm \sigma_{exp})\,/\epsilon_0$
Borexino [8]	0.0398 ± 0.0102	2.38 ± 0.61
SK-I [22]	0.0252 ± 0.0072	1.51 ± 0.43
SNO Phase I [23]	0.0143 ± 0.0086	0.86 ± 0.51

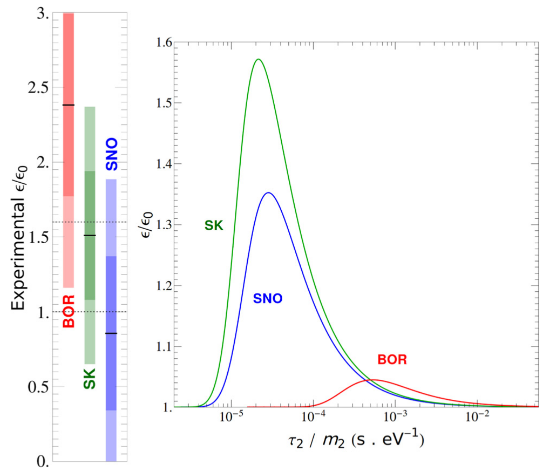

Fig. 3. Left: Experimental values for ϵ/ϵ_0. Black lines are the best-fit values and darker (lighter) shades are the 1σ (2σ) ranges as shown in Table 1. Right: Dependence of the orbital eccentricity ϵ with the neutrino lifetime τ_2/m_2 as it would be measured by different experiments — the ^{7}Be line in Borexino (BOR), and the ^{8}B spectrum in Super-Kamiokande (SK) and SNO.

$$R = R_0\,\frac{N(r_{\mathrm{per}})}{N(r_{\mathrm{aph}})} = \frac{(1+\epsilon)^2}{(1-\epsilon)^2}\,, \tag{9}$$

where r_{aph} (r_{per}) is the aphelion (perihelion) distance and N is the number of events calculated from the convolution of the adequate probabilities and cross sections for each experiment.

From Eq. (4) and Eq. (5), we know that $N(r_{\mathrm{per}}) > N(r_{\mathrm{aph}})$ holds also for the decay scenario due to P_2^{surv} dependence on the orbital distance. This implies that $R > R_0$ for all energies and thus, for any neutrino decay scenario, an enhancement in the seasonal variation of the solar neutrino flux would be expected.

Thus, the measurement of an eccentricity $\epsilon > \epsilon_0$ is a hint in the direction of the neutrino decay scenario. In fact, some experiments have measured Earth's orbital eccentricity to be different than the standard value albeit still compatible with ϵ_0 as shown in Table 1.

Fig. 3 shows the dependence of the neutrino eccentricity ϵ with the neutrino lifetime τ_2/m_2 as it would be measured by SuperKamiokande (SK), SNO and Borexino (BOR) experiments. As it can be seen, the higher energy ^{8}B solar neutrinos (measured by SK and SNO) would have a greater seasonal variation due to decay than the lower energy ^{7}Be solar neutrinos (measured by Borexino).

Due to the MSW effect, the ν_2 content in the neutrino flux leaving the Sun is energy dependent. At higher energies, there are more ν_2 neutrinos available for decay during the propagation to Earth. On the other hand, for lower energy neutrinos, there are fewer ν_2 leaving the sun and thus fewer ν_2 available for decay. For this reason, the seasonal variation for higher energy neutrinos would be bigger than for lower energy neutrinos and, consequently, also the measured eccentricity. Also from Fig. 3, it can be seen that due to the decay survival probability in Eq. (3), the lower (higher) the energy of the neutrinos, the bigger (smaller) is the lifetime for which the enhancement in the eccentricity is maximum.

We can now include the eccentricity data in the analysis as a penalty function added to the χ^2 for each experiment: $\chi^2_{\text{seasonal}} = (\epsilon_{\text{exp}} - \epsilon)^2/(\sigma_{\text{exp}})^2$. The marginalization of the combined $\Delta\chi^2$ results in a slightly lower value

$$\tau_2 / m_2 \geq 7.2 \times 10^{-4}\ \text{s}\,.\,\text{eV}^{-1}, \text{ at } 99\% \text{ C.L.} \tag{10}$$

for the decay parameter. This is due to the fact that the seasonal variation data favor non-zero values for the lifetime while the solar data analysis favors a no-decay scenario. The combination of both samples results in the lower value for the neutrino lifetime.

5. Conclusion

We know that neutrinos oscillate with non-zero mass differences and mixing angles. *Can neutrinos decay?* The answer is negative from the combined analysis of data of solar neutrino experiments and KamLAND and Daya Bay data. From our analysis, we have obtained a new upper bound to the ν_2 eigenstate lifetime $\tau_2 / m_2 \geq 7.2 \times 10^{-4}$ s . eV^{-1} at 99% C.L. which is almost one order higher than the previous established bound [1] at $\tau_2/m_2 \geq 8.7 \times 10^{-5}$ s . eV^{-1} at 99% C.L. Also, for comparison with Ref. [10], our result at 2σ is $\tau_2 / m_2 \geq 1.1 \times 10^{-3}$ s . eV^{-1} which is a similar but more constrained result.

Also, we have shown how decay can enhance the seasonal variation of solar neutrino fluxes and how it affects the measurement of Earth's orbital eccentricity. Current data is not good enough to improve the constraints to neutrino lifetime. Although future experiments could certainly improve on the measurement of solar neutrino fluxes and thus better constrain neutrino lifetime, the analysis of existing data from later phases of, e.g., Super-Kamiokande and SNO for its seasonal variation could, in principle, already improve such constraints. We urge those experimental collaborations [22,23] to redo their analysis with more of the available data.

Acknowledgements

The authors would like to thank FAPESP, CNPq and CAPES for several financial supports. O.L.G.P. thanks the support of FAPESP funding grant 2012/16389-1.

References

[1] A. Bandyopadhyay, S. Choubey, S. Goswami, Neutrino decay confronts the SNO data, Phys. Lett. B 555 (2003) 33–42, http://dx.doi.org/10.1016/S0370-2693(03)00044-3.
[2] B.T. Cleveland, et al., Measurement of the solar electron neutrino flux with the Homestake chlorine detector, Astrophys. J. 496 (1998) 505–526, http://dx.doi.org/10.1086/305343.
[3] W. Hampel, et al., GALLEX solar neutrino observations: results for GALLEX IV, Phys. Lett. B 447 (1999) 127–133, http://dx.doi.org/10.1016/S0370-2693(98)01579-2.
[4] J.N. Abdurashitov, et al., Measurement of the solar neutrino capture rate with gallium metal. III: results for the 2002–2007 data-taking period, Phys. Rev. C 80 (2009) 015807, http://dx.doi.org/10.1103/PhysRevC.80.015807.
[5] M. Altmann, et al., Complete results for five years of GNO solar neutrino observations, Phys. Lett. B 616 (2005) 174–190, http://dx.doi.org/10.1016/j.physletb.2005.04.068.
[6] K. Abe, et al., Solar neutrino results in Super-Kamiokande-III, Phys. Rev. D 83 (2011) 052010, http://dx.doi.org/10.1103/PhysRevD.83.052010.
[7] B. Aharmim, et al., Combined analysis of all three phases of solar neutrino data from the Sudbury Neutrino Observatory, Phys. Rev. C 88 (2013) 025501, http://dx.doi.org/10.1103/PhysRevC.88.025501.
[8] G. Bellini, et al., Final results of Borexino phase-i on low-energy solar neutrino spectroscopy, Phys. Rev. D 89 (2014) 112007, http://dx.doi.org/10.1103/PhysRevD.89.112007.
[9] M.C. Gonzalez-Garcia, Y. Nir, Neutrino masses and mixing: evidence and implications, Rev. Mod. Phys. 75 (2003) 345–402, http://dx.doi.org/10.1103/RevModPhys.75.345.
[10] J.M. Berryman, A. de Gouvea, D. Hernandez, Solar neutrinos and the decaying neutrino hypothesis, arXiv:1411.0308.
[11] M.C. Gonzalez-Garcia, M. Maltoni, Status of oscillation plus decay of atmospheric and long-baseline neutrinos, Phys. Lett. B 663 (2008) 405–409, http://dx.doi.org/10.1016/j.physletb.2008.04.041.
[12] R.A. Gomes, A.L.G. Gomes, O.L.G. Peres, Constraints on neutrino decay lifetime using long-baseline charged and neutral current data, Phys. Lett. B 740 (2015) 345–352, http://dx.doi.org/10.1016/j.physletb.2014.12.014.
[13] A. Gando, et al., Constraints on θ_{13} from a three-flavor oscillation analysis of reactor antineutrinos at KamLAND, Phys. Rev. D 83 (2011) 052002, http://dx.doi.org/10.1103/PhysRevD.83.052002.
[14] F.P. An, et al., Spectral measurement of electron antineutrino oscillation amplitude and frequency at Daya Bay, Phys. Rev. Lett. 112 (2014) 061801, http://dx.doi.org/10.1103/PhysRevLett.112.061801.
[15] A.S. Joshipura, E. Masso, S. Mohanty, Constraints on decay plus oscillation solutions of the solar neutrino problem, Phys. Rev. D 66 (2002) 113008, http://dx.doi.org/10.1103/PhysRevD.66.113008.
[16] A.S. Dighe, Q.Y. Liu, A.Yu. Smirnov, Coherence and the day–night asymmetry in the solar neutrino flux, arXiv:hep-ph/9903329.
[17] J.M. Berryman, A. de Gouva, D. Hernı́ndez, R.L.N. Oliviera, Non-unitary neutrino propagation from neutrino decay, Phys. Lett. B 742 (2015) 74–79, http://dx.doi.org/10.1016/j.physletb.2015.01.002.
[18] P.C. de Holanda, A.Y. Smirnov, Solar neutrino spectrum, sterile neutrinos and additional radiation in the Universe, Phys. Rev. D 83 (2011) 113011, http://dx.doi.org/10.1103/PhysRevD.83.113011.
[19] F. Kaether, W. Hampel, G. Heusser, J. Kiko, T. Kirsten, Reanalysis of the GALLEX solar neutrino flux and source experiments, Phys. Lett. B 685 (2010) 47–54, http://dx.doi.org/10.1016/j.physletb.2010.01.030.
[20] J. Hosaka, et al., Solar neutrino measurements in super-Kamiokande-I, Phys. Rev. D 73 (2006) 112001, http://dx.doi.org/10.1103/PhysRevD.73.112001.
[21] C. Arpesella, et al., Direct measurement of the Be-7 solar neutrino flux with 192 days of Borexino data, Phys. Rev. Lett. 101 (2008) 091302, http://dx.doi.org/10.1103/PhysRevLett.101.091302.
[22] M.B. Smy, et al., Precise measurement of the solar neutrino day/night and seasonal variation in Super-Kamiokande-I, Phys. Rev. D 69 (2004) 011104, http://dx.doi.org/10.1103/PhysRevD.69.011104.
[23] B. Aharmim, et al., A search for periodicities in the B-8 solar neutrino flux measured by the Sudbury Neutrino Observatory, Phys. Rev. D 72 (2005) 052010, http://dx.doi.org/10.1103/PhysRevD.72.052010.